The Dissertation Committee for Vassili Demergis
certifies that this is the approved version of the following dissertation:

Ultra-Precise Manipulation and Assembly of Nanoparticles Using Three Fundamental Optical Forces

Committee:

Ernst-Ludwig Florin, Supervisor

George T. Shubeita

Manfred Fink

Dmitrii E. Makarov

Brian A. Korgel

Ultra-Precise Manipulation and Assembly of Nanoparticles Using Three Fundamental Optical Forces

by

Vassili Demergis, B.S.

DISSERTATION

Presented to the Faculty of the Graduate School of

The University of Texas at Austin

in Partial Fulfillment

of the Requirements

for the Degree of

DOCTOR OF PHILOSOPHY

THE UNIVERSITY OF TEXAS AT AUSTIN

December 2012

Dedicated to my family.

Acknowledgments

I thank my graduate research advisor, Prof. Ernst-Ludwig Florin, for providing the meticulous yet undefined research environment which allowed my work to develop along a creative and satisfying path. I also thank Prof. Manfred Fink and Prof. George Shubeita for their continuous support of my work, progress, and time spent here.

Thanks to all the members of the Florin Lab I've worked with, especially Katie Hinko, Andrea Keidel, Tobias Bartsch, Katja Taute, Martin Kochanczyk, Pinyu Thrasher, Frank Schwemmer, Chieze Ibeneche, and Avraham (Memi) Beer. Thanks to everyone in the biophysics group and the Center for Nonlinear Dynamics for their support and for providing an exceptional work environment.

Thanks to all the staff in the physics machine shop for teaching me to fabricate the necessary parts for development of my experimental instruments.

I thank my undergraduate research advisor, Prof. Steven M. Anlage of the University of Maryland at College Park, for providing me an excellent opportunity to work for several years on significant research problems as an undergraduate student. It was only through this experience in which I discovered I had a true talent and love for experimental and computational research. This experience was an invaluable part of my success as a graduate student

and for successes to come.

Likewise, I thank Prof. Dennis Drew, also of the University of Maryland, for allowing me to work in his optics lab for one summer as an undergraduate. Dr. Drew allowed me to explore any area of optics which I was interested, even if not related to his own work. He allowed me full use of any free equipment he possessed, and even purchased additional items for my random explorations from his own grant money. This was exceptionally kind, and this experience significantly increased my love of physics.

I sincerely thank Mr. Sean Chappe, my high school physics teacher at Hunterdon Central Regional High School in New Jersey. I took every physics course he offered over 3 years, and he cared enough to recognize my talent from the first day. He would assign the classes additional projects solely for my own educational benefit. He continues to be a good mentor and friend.

Most importantly I thank my family, especially my mom, dad, and brother, for always believing in me and supporting me.

Ultra-Precise Manipulation and Assembly of Nanoparticles Using Three Fundamental Optical Forces

Publication No. _____

Vassili Demergis, Ph.D.
The University of Texas at Austin, 2012

Supervisor: Ernst-Ludwig Florin

The invention of the laser in 1960 opened the door for a myriad of studies on the interactions between light and matter. Eventually it was shown that highly focused laser beams could be used to confine and manipulate matter in a controlled way, and these instruments were known as *optical traps*. However, challenges remain as there is a delicate balance between object size, precision of control, laser power, and temperature that must be satisfied.

In Part I of this dissertation, I describe the development of two optical trapping instruments which substantially extend the allowed parameter ranges. Both instruments utilize a standing wave optical field to generate strong optical gradient forces while minimizing the optical scattering forces, thus dramatically improving trapping efficiency. One instrument uses a cylinder lens to extend the trapping region into a line focus, rather than a point focus, thereby confining objects to 1D motion. By translation of the cylinder

lens, lateral scattering forces can be generated to transport objects along the 1D trapping volume, and these scattering forces can be controlled independently of the optical gradient forces. The second instrument uses a collimated beam to generate wide, planar trapping regions which can confine nanoparticles to 2D motion.

In Part II, I use these instruments to provide the first quantitative measurements of the *optical binding* interaction between nanoparticles. I show that the optical binding force can be over 20 times stronger than the optical gradient force generated in typical optical traps, and I map out the 2D optical binding energy landscape between a pair of gold nanoparticles. I show how this ultra-strong optical binding leads to the self-assembly of multiple nanoparticles into larger contactless clusters of well defined geometry. I finally show that these clusters have a geometry dependent coupling to the external optical field.

Table of Contents

List of Tables

List of Figures

Part I

Nanoparticle Manipulation Using the Optical Scattering and Gradient Forces

Chapter 1

Introduction to Optical Forces

Since the first experimental demonstration of the laser in 1960 [1], studies involving the interactions between light and matter have rapidly become more accessible. This has led to a rapid increase in technological advancements utilizing optical properties. Everything from the more commonplace such as fiber-optic telecommunications, finger-print scanners and laser-based surgery, to technologies still in development such as photonic circuitry [2–4], holographic data storage [5, 6], and quantum computing [7–12]. Nanoscale optical systems are especially intriguing. At that scale, objects typically have a mass small enough such that photons scattered by the object impart a significant amount of momentum and cause the object to move. This most basic light-matter interaction is commonly known as *radiation pressure*, and more technically known as the *scattering force*.

1.1 First Observations of Radiation Pressure

Generally, the forces applied to objects due to light scattering cannot be observed with the naked eye. Objects encountered in everyday life are typically far too massive, and the photon momentum is far too small to cause

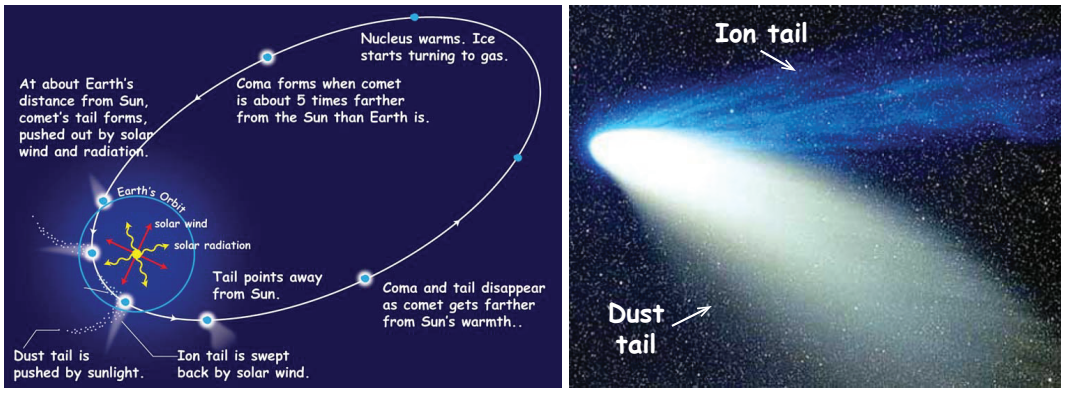

Figure 1.1: Comet tail formation near the sun. As the comet nears the sun, gas and dust particles are pushed away due to solar radiation pressure. Ions experience a stronger force component from solar wind than neutral particles, and the ions tend to follow magnetic field lines. Right panel: The comet *Hale-Bopp* photographed at its perihelion in April of 1997. Images from http://spaceplace.NASA.gov.

any significant motion of those objects. However, there are several instances in which the circumstances are just right for radiation pressure to be readily observed. In fact, radiation pressure was documented as early as 1610 in a letter from Johannes Kepler to Galileo Galilei in which he described how comet tails always point away from the sun [13, 14]. He suggested that the sun itself may cause this effect, and as it turned out he was correct. Small dust particles and gases surrounding the comet are pushed away from the sun by the photons which impact and scatter off [15, 16].

In the vacuum of space there is little to dampen the acceleration of the small dust particles, and so the effect of this radiation pressure on comet tails is very pronounced. However, in vacuum even massive objects can be significantly accelerated. The solar radiation pressure (SRP) can be expressed

for a perfectly absorbing object as in reference [17]:

$$p_{SR} = \frac{L_{sun}}{4\pi r^2 c} \tag{1.1}$$

where $L_{sun} = 3.85 \times 10^{26}\, W$ is the luminosity of the sun, r is the distance of the object from the sun, and c is the speed of light in vacuum. Thus, the SRP on an object near the Earth ($r = 1 A.U. = 1.5 \times 10^{11} m$) is roughly $4.5 \times 10^{-6} \frac{N}{m^2}$. This is in fact a significant pressure for objects which remain in space for long periods of time. For example, GPS satellites must have their trajectories corrected for solar radiation pressure effects, and fluctuation of the solar irradiance is the dominant source of error in computing these trajectories [18, 19]. Massive objects are also affected, such as the command/service module (CSM) of the Apollo 11 mission. We can actually estimate the effect of solar radiation pressure on the moon mission by considering the displacement of the CSM over its 3 day trip from the Earth to the moon as:

$$\Delta x \approx \frac{1}{2} a t^2 \tag{1.2}$$

$$\approx \frac{p_{SR}\, A\, t^2}{2m} \tag{1.3}$$

where a is the acceleration of the object, t is the time the pressure is applied to the object, m is the mass of the object, and A is the cross-sectional area of the object. For the approximate weight and dimensions of the CSM ($A \approx 40 m^2$, $m = 3 \times 10^4 kg$), we can estimate that by the time the CSM reached the moon, it would have been displaced by about $200m$ due solely to the solar radiation pressure. When we consider a trip from Earth to Mars (about 9

months travel time) for a similar spacecraft, we can estimate the displacement to be over $1000km$. In fact, these displacements are precisely calculated and taken into account by NASA scientists to guarantee successful missions and can even be used to aid in spacecraft maneuvering [20–26]. This acceleration of large objects through light scattering is an intriguing concept and may eventually lead to spacecraft powered by "solar sails" [17, 27–29], however the fundamental processes in which light applies forces on objects are more easily studied in the lab on the single particle level.

1.2 The Scattering Force for Manipulating Microscopic Particles

The first calculations describing radiation pressure on nanoparticles were described by James Clerk Maxwell in 1871 using his theories on electromagnetism [30], and in 1901 Peter Lebedew reported the first experimental demonstration [31]. However it wasn't until the introduction of the laser in 1960 that this *scattering force* was considered as a viable tool for precise manipulation of microscopic objects. The first demonstration using lasers as the basis for manipulating objects using scattering forces was performed in 1969 by Arthur Ashkin [32, 33], a scientist at Bell Telephone Laboratories in New Jersey. He showed that not only were micron-scale particles easily manipulated by laser light, but that due to the strong dependence of the magnitude of the scattering force on the size of the particle (see also equation (1.5)), particles of different sizes could effectively be sorted. In his demonstration,

larger $2.68\mu m$ diameter particles would be transported along the direction of light propagation while smaller $0.59\mu m$ diameter particles would be left behind [32]. Additional calculations and experiments dealing with the optical scattering force soon followed [34–43], and the scattering force can succinctly be written as in references [39, 41, 44]:

$$F_{scat}(\vec{x}) = \frac{8\pi^3\alpha^2}{3cn_m^3\epsilon_0^2\lambda^4} I(\vec{x}) \tag{1.4}$$

$$= \frac{128\pi^5 a^6 n_m}{3c\lambda^4} \left[\frac{(n_p/n_m)^2 - 1}{(n_p/n_m)^2 + 2}\right]^2 I(\vec{x}) \tag{1.5}$$

where a is the radius of the particle, n_p and n_m are the refractive indexes of the particle and the surrounding medium respectively, λ is the wavelength of the excitation light, α is the polarizability of the particle, and $I(\vec{x})$ is the intensity of the light at the position of the particle ($\vec{x}$). While the scattering force is very efficient in transporting particles, stable confinement of particles typically cannot be achieved by a single beam using only the scattering forces.

To achieve "optical trapping" of his micro-spheres (optical levitation free from direct surface contact), Ashkin used two counter-propagating laser beams such that the net scattering force on the particle was zero (see figure 1.2). While this generated stable trapping along the axis of light propagation, the particles could still experience confinement perpendicular to this axis, albeit relatively weakly. Ashkin attributed these radially confining optical forces to the momentum transferred into the particle during refraction of the photons as they entered and exited the curved surfaces of the sphere. Figure 1.2c shows that for an incident beam of non-uniform intensity, such as a Gaussian beam,

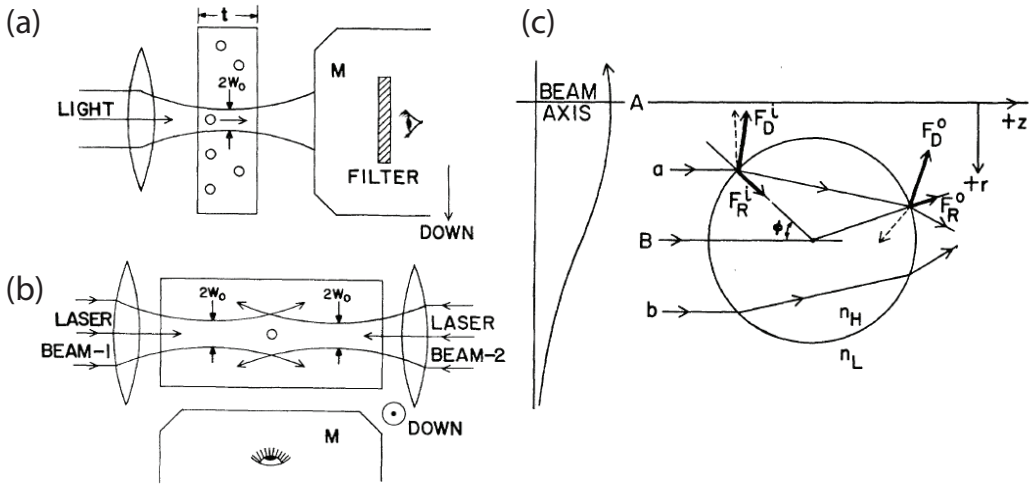

Figure 1.2: Original figures from Ashkin's first paper on optical trapping by radiation pressure [32]. a) Particles are accelerated towards a glass surface by the scattering force. b) Stable suspension of particles using two counter-propagating laser beams. The net scattering force here is nearly zero. c) Description of forces applied to the particle due to refraction of the light rays. The particle is pulled toward the highest intensity light rays.

the net force on the particle due to refraction of the photons pulls the particle toward the highest intensity light rays and is dependent on the spatial variation (gradient) of the light intensity. This kind of force is therefore known as the *gradient force*. On this size scale, when the particle radius is much larger than the wavelength of the excitation light, this ray optics description is valid and is conceptually very similar to the description of the scattering force (i.e. momentum is transfered from the photon to the object). However, for much smaller particles whose radius is much smaller than the wavelength of the excitation light (Rayleigh particles) this description becomes invalid as the light rays cannot be considered to refract at precise locations on the particle surface.

A different conceptual model must be used to describe the gradient force for Rayleigh particles.

1.3 The Gradient Force & Optical Tweezers

After his demonstrations of particle manipulation using the scattering force [32, 33], Ashkin quickly realized that the gradient force (which he called the *dipole force* in early publications) could be used as a powerful tool for optical confinement of microscopic particles. In 1980 he published calculations predicting that stable trapping of single atoms should even be possible provided a reasonable method to slow down the thermal motion of the atoms was possible [35]. Soon after, from in 1984 to 1986, he worked with Steven Chu to provide the first experimental observation of optically trapped atoms, made possible by new laser based cooling techniques and magneto-optical trapping [38]. Chu's work on cooling and trapping single atoms earned him the 1997 Nobel prize in physics [45]. Chu left Bell Labs shortly after trapping atoms while Ashkin remained and continued to work on optical gradient force trapping, this time with a focus on trapping biological material. The first experimental demonstrations of optical gradient force trapping using a single laser beam came in 1986 [44], and trapping of biological material by the same method was described in 1987 [46, 47]. The technique of optical trapping by a single, highly focused laser beam was termed "optical tweezers," and also often called a "single beam trap" [48–61].

Ashkin used optical tweezers to trap not only micron-sized dielectric

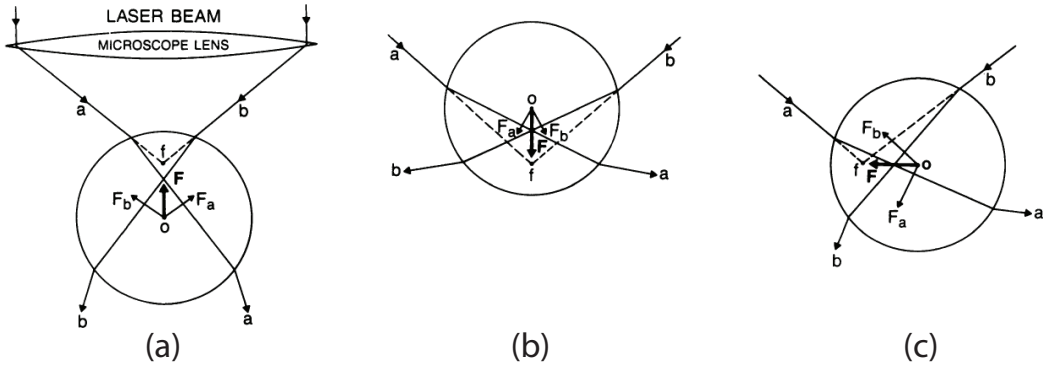

Figure 1.3: Diagram illustrating gradient force trapping by a single focused laser beam in the ray optics regime. Light rays are refracted as they enter and exit through the particle surfaces, thereby transferring momentum from the photon to the particle. The net force generated (F) is always toward the focal point (f) from the particle center (O). The object is displaced a) below the focus, b) above the focus, and c) laterally from the focus. Figure adapted from reference [61].

objects such as glass spheres and bacteria, but also the tobacco mosaic virus which has a size much closer to the Rayleigh regime ($length \approx 320nm$, $diam \approx 20nm$) [44, 62]. However, while trapping of objects whose size is larger than the wavelength of incident light can be described by ray optics (see figure 1.3), a different model is needed to describe Rayleigh particles. For Rayleigh objects, it is not possible to describe the refraction of light rays at precise locations on the particle surface since the wavelength of the light is much larger than the particle radius. The gradient forces generated on Rayleigh objects can be described by considering the polarizability of the particle. An object in an electric field becomes polarized with a dipole moment ($\vec{p}$) of:

$$\vec{p} = \alpha \vec{E} = q\vec{d} \tag{1.6}$$

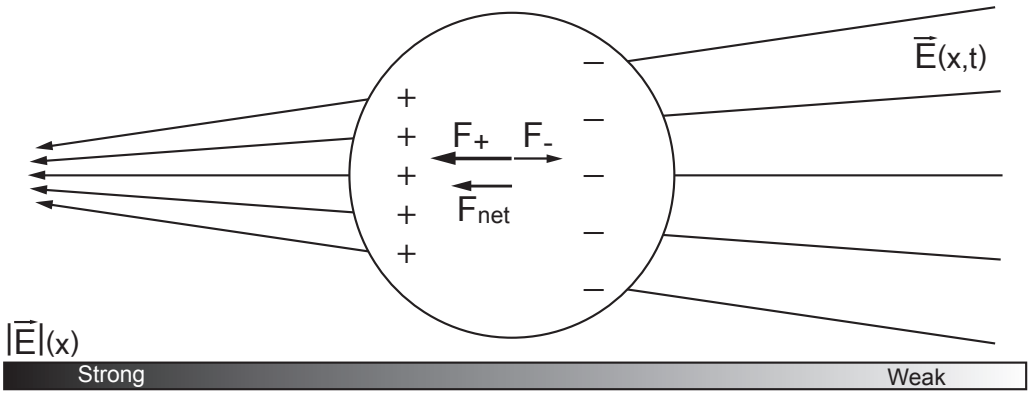

Figure 1.4: Diagram illustrating how gradient forces are generated on a Rayleigh particle. In the presence of an electric field, the particle can become polarized. If the field is non-uniform (stronger on one side of the particle than the other), the polarized particle experiences a stronger force toward the direction of increasing intensity (for polarizability $\alpha > 0$).

where α is the polarizability of the particle and $\vec{E}$ is the electric field at the location of the particle. The dipole moment of the particle defined here is also equivalent to the dipole moment of two charges ($\pm q$) separated by a displacement $\vec{d}$. Figure 1.4 illustrates this concept. We also know the force acting on a charge is described by the Lorentz relation:

$$\vec{F_q} = q\vec{E} \tag{1.7}$$

In the case where the polarized particle is in a non-uniform field, you can consider that the magnitude of the electric field on one side of the particle is larger than on the other side, thereby generating a larger force on the side of larger electric field (see figure 1.4). If the polarizability of the particle is positive ($\alpha > 0$), the force is directed toward the direction of the stronger field. In the case of optical tweezers, this would be toward the focal point of

the laser. The gradient force on a Rayleigh particle can then be written as derived in reference [41]:

$$\vec{F}_{grad}(\vec{x}) = \frac{1}{4}\alpha\nabla|E(\vec{x})|^2 \tag{1.8}$$

$$= \frac{2\pi n_m a^3}{c}\left[\frac{(n_p/n_m)^2 - 1}{(n_p/n_m)^2 + 2}\right]\nabla I(\vec{x}) \tag{1.9}$$

where we have utilized the relationship between the intensity of light and the electric field amplitude as:

$$I(\vec{x}) = \frac{cn_m\epsilon_0}{2}|E(\vec{x})|^2 \tag{1.10}$$

We can compare the gradient and scattering forces applied to a particle in an optical tweezer to determine the criteria for stable optical trapping. Since the scattering force acts to push the particle in the direction of light propagation, the peak gradient force along the optical axis which pulls the particle toward the focal spot must be stronger than the scattering force at that location. This is a particular weakness in the trapping mechanism as the intensity gradients along the optical axis are much weaker than perpendicular to it. As shown in references [41, 44], we can then use equations (1.5) and (1.9) along with the axial position where the peak intensity gradient is located to define a condition for stable trapping. The intensity distribution of a Gaussian focal spot can be written as in reference [41]:

$$I(x, y, z) = \frac{2P}{\pi}\left[\frac{1}{\omega_0^2 + 4z^2}\right] e^{-\frac{2(x^2+y^2)}{\omega_0^2+4z^2}} \tag{1.11}$$

where P is the total laser power in the beam related to the peak electric field amplitude by $P = \frac{1}{4}\pi\omega_0^2 n_m\epsilon_0 cE_0^2$, and ω_0 is the radius of the beam waist and is

related to the numerical aperture (NA) of the trapping lens by $\omega_0 \approx \frac{\lambda}{2NA}$. The location of the strongest gradient force along the optical axis of a Gaussian point focused beam is then given by $(x, y, z) = (0, 0, \frac{\pi\omega_0^2}{\sqrt{3}\lambda}) = (0, 0, \frac{\pi\lambda}{4\sqrt{3}NA^2})$. Therefore, the trapping condition for Rayleigh particles can be written as in reference [41]:

$$\frac{F_{grad}}{F_{scat}} = \frac{3\sqrt{3}\lambda^3 NA^2}{32\pi^5 a^3}\left[\frac{(n_p/n_m)^2+2}{(n_p/n_m)^2-1}\right] \geq 1 \tag{1.12}$$

We can see here a strong dependence on the numerical aperture of the focusing lens, and in fact typically very high numerical aperture lenses ($NA \approx 1.3$) are used in order to generate stable trapping of small particles.

From just equation (1.12) we would expect that smaller particles are easier to trap since the scattering force drops off more quickly than the gradient force with size, but this is not the case. The above condition does not consider thermal forces, which greatly affect the ability to stably confine the particles. This thermal stability condition is mainly dependent on the strength of the gradient force. Since the depth of the potential energy well (U_0) for the trapped particle is proportional to $\int F_{grad}\,\mathrm{d}\vec{s}$ (where s is the escape path), then from equation (1.9) we also know $U_0 \propto a^3$. So for smaller and smaller particles, the depth of the trapping potential rapidly decreases while the thermal energy of the particle remains constant (at $k_B T$). This is the main reason why trapping very small particles is much more difficult than large particles. Indeed, only when advanced cooling techniques were developed which minimized the thermal energy of the particle could single atoms be trapped [38]. However, it is not always possible to cool the object. For example, biological applications

[63–87] are required to be kept at or near room temperature if they are to remain functional. Since the thermal motion of objects cannot be reduced in these cases, techniques improving stability though reducing the strength of the scattering force and increasing strength of the gradient force began to be developed. The primary example of this is the standing wave optical trap.

1.4 The Standing Wave Optical Trap

In 1998, Pavel Zemánek and his colleagues at the Academy of Sciences of the Czech Republic proposed a method of optical trapping utilizing a standing wave optical field [88–95]. By focusing the laser onto a reflective surface, a standing wave is generated along the optical axis due to the interference of the incident and reflected beams (see figure 1.5). This simple geometry had two significant advantages. First, if the reflectivity of the surface is approximately 100%, then the scattering force on the particle due to the incident beam is completely compensated by the scattering force generated by the reflected beam. Therefore, the condition for stable trapping which requires the scattering force to be weaker than the peak axial gradient force is always satisfied (equation (1.12)). This would imply not only higher stability trapping, but certain conditions no longer need to be met. For example, the numerical aperture of the trapping lens no longer needs to be large, and this was demonstrated in reference [95]. In fact, the beam needs not be focused at all since a completely collimated beam would still generate an axial gradient force due only to the standing wave. I will actually demonstrate and utilize this effect

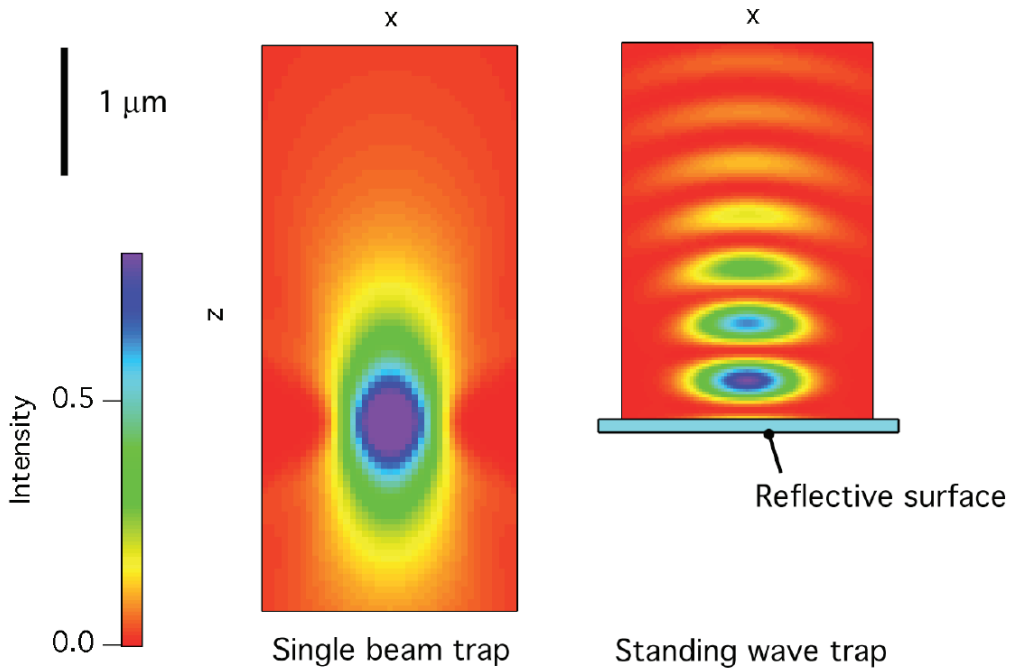

Figure 1.5: Calculations of the traditional optical tweezer intensity profile compared to that of the standing wave optical trap. For the same peak intensity, the gradient forces in the standing wave trap are much greater due to the shortened distances between peak and minimum intensity. The greatest improvement is along the optical axis (z-axis), which is the weakest axis in the standard single beam trap. The wavelength of incident light is $\lambda = 800nm$. Figure from reference [95].

to great advantage in chapters 2 and 6.

The second advantage is in terms of the gradient forces generated. We can see in figure 1.5 that in a traditional single beam trap the focal spot intensity distribution is greatly elongated along the optical axis (z-axis) compared to the radial dimension. This typically would allow a trapped particle to be significantly pushed along the optical axis by scattering forces to a position

where the confinement by the gradient forces would then be weaker. Thus the particle would be more likely to escape and usually does so along the optical axis due to the lower restoring gradient force in that direction. In contrast, when a standing wave is generated the axial intensity gradients become much stronger than in the case of the single beam trap, and become even stronger than the radial gradient forces. This is due mainly to the much shorted distance between intensity maximum to minimum, which is now about $\lambda/4$ axially compared to the single beam trap which is on the order of 2λ axially. In fact, the peak axial gradient force is calculated to be over 15 times stronger in the standing wave trap compared to the single beam trap for the same laser power [95].

We see that the standing wave optical trap eliminates (in a perfect system) the destabilizing scattering force while amplifying the gradient forces, especially along the optical axis which was previously the weakness of the single beam trap. With these improvements, it became possible to stably trap much smaller dielectric nanoparticles, down to $40nm$ in diameter, at reasonable laser powers and at room temperature [89, 95]. This is 3 times smaller in volume compared to the tobacco mosaic virus trapped by Ashkin in 1986 [44]. Since the standing wave geometry shows such significant improvement in trapping of nano-scale objects, I will use this as the basis on which my optical trapping instruments are developed.

1.5 Other Optical Manipulation Methods

The standing wave optical trap is not the only advancement in optical trapping since Ashkin's work. There are many variations on optical tweezer design, all with their own advantages and disadvantages. However, there are two primary goals for basing my new optical instruments on the standing wave geometry rather than any other. First, I intend to trap the smallest particles possible using the least laser power. This is to ensure measurements of optical effects within the Rayleigh regime while also avoiding significant heating of the objects. Second, the objects must be trapped far from physical surfaces in order to ensure the particles are free to move and are not experiencing surface friction or drag effects. The standing wave geometry satisfied both of these conditions. I will now briefly describe the other major classes of optical trapping and manipulation techniques which have been developed since Ashkin's original work and discuss them in reference to the two above conditions.

1.5.1 Evanescent Field Traps

One method to generate strong intensity gradients is by utilizing evanescent waves. When an incident beam strikes an interface between two media of different refractive indexes, part of the beam is reflected and part of the beam is transmitted. However, if the beam propagates from a high index material into a low index material and strikes the interface at an angle greater than the critical angle, resulting in total internal reflection of the beam, an evanescent field is generated within the low index medium. Figure 1.6 illustrates this

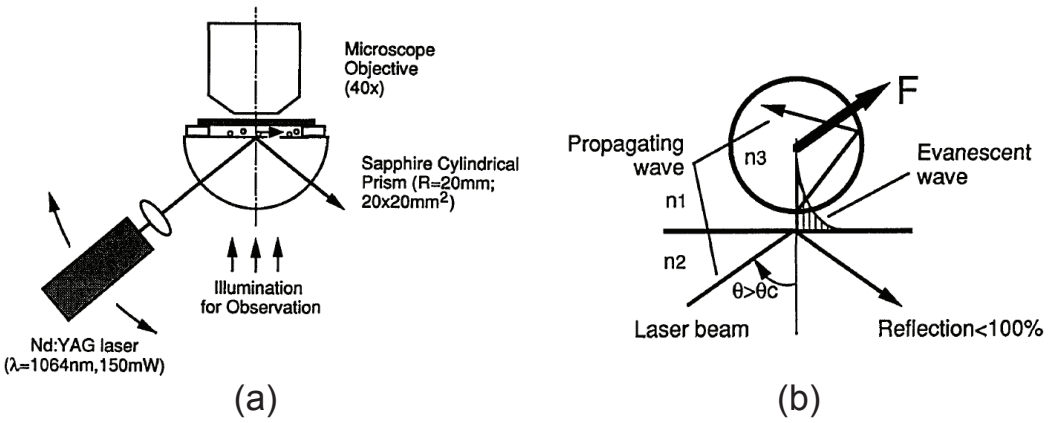

Figure 1.6: Diagram of optical trapping by evanescent waves adapted from reference [96]. a) An incident laser beam is focused on the interface between two media of different refractive indexes. b) When the angle of the incident beam is greater than the critical angle, total internal reflection occurs and an evanescent field is generated within the second medium which decays exponentially with distance from the interface. This steep intensity gradient pull particles toward the surface. In addition, a scattering force is generated in the direction of light propagation.

concept. The evanescent field intensity decays exponentially with distance from the interface, thus creating steep intensity gradients. Particles in this evanescent field experience a strong gradient force, pulling them toward and into contact with the surface [96–102].

In addition, a scattering force is generated on the particles as indicated in figure 1.6b. This scattering force is similar to the scattering force described in chapter 1.2 in that momentum from the incident photons is transferred to the particle. Interestingly though, an evanescent field is not a propagating wave and therefore carries no momentum. The scattering force here is therefore attributed to conversion of the evanescent field back into a propagating field

inside the particle, or equivalently the tunneling of photons through the gap between the particle and surface [96]. Through this process, momentum of the incident beam can be transferred to the particle, and particles can then also be driven across the surface in addition to being pulled towards it by the gradient force [96, 99, 101, 102].

While this method generates very strong gradient forces, the primary concern when using this technique is the contact the particles make with the surface. Bounded by a hard surface, particles are not free to move in all directions. Additionally, friction and drag forces due to contact with the surface prevent free motion of the particles, which can be otherwise used as a reporter for the optical forces the particles experience. As I will show in Part II, this is important for revealing and measuring unexpected optical interactions.

1.5.2 Scanning Single Beam Traps

It is also possible to modify traditional single beam optical tweezers in order to generate intensity fields of nearly arbitrary three-dimensional geometries. One such method is the use of motorized mirrors or acousto-optical modulators to rapidly scan the focus of the laser within the sample. This essentially distributes the laser intensity over the desired path, typically defined through a computer program, and the time the beam has spent at each position in that path determines the trapping strength at that position [103–114]. Using this method, it is possible to generate arrays of discrete trapping regions (known as "time shared" trapping), or extended traps, such as lines, loops or

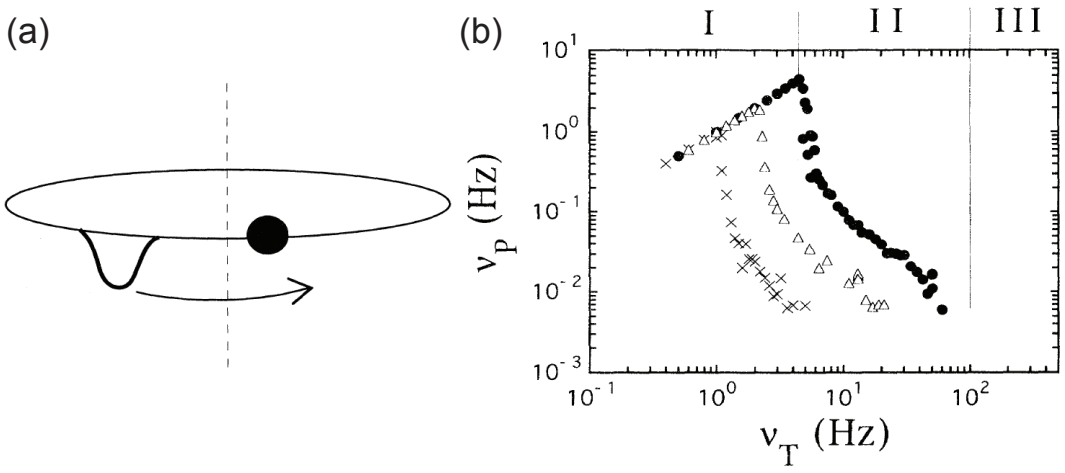

Figure 1.7: Particle transport in scanning optical tweezers. a) A single beam optical trap is rapidly scanned in a circle roughly $16\mu m$ in diameter thereby confining a particle along the same path. The location of the trapping potential during the scan is indicated by the inverted Gaussian curve. b) Dependence of the velocity of the particle (v_p) with respect to the velocity of the scanned trap (v_T) and laser power. $700mW$ (circles), $300mW$ (triangles), $150mW$ (crosses). Figure adapted from reference [105].

other shapes.

Figure 1.7 shows an example of a scanning optical trap which traces out a circular path $16\mu m$ in diameter. The particle is then confined to the path traced out by the trap, but is pulled by the optical trap along the path every time the trap passes by. Figure 1.7b shows the velocity of the particle as a function of the velocity of the scanning trap and the laser power. As expected, for low scan velocities, the trap pulls the particle along with it and the particle velocity is identical to the trap velocity. However, at a critical speed determined by the drag forces and laser power, the particle can no longer be pulled effectively by the trap and gets left behind. Therefore we see

the particle velocity decrease rapidly until it is relatively unaffected by the motion of the trap.

The relative intensities of different positions in the scan can also be varied. More time spent at a location by the laser means a higher time averaged intensity field, and thus stronger gradient forces. By precise control over the position of the trap and the dwell time at each location, intensity fields can be generated which can perform interesting functions, such as for guiding and sorting of particles. Figure 1.8 shows an example in which a carefully sculpted intensity field can sort different sized particles from a fluid flow. The optical field is shaped to have regions of varying intensity. Since the gradient force is proportional to a^3 (where a is the particle radius) while the Stokes drag on the particles is proportional to a, the smaller particles cannot be contained by the weaker intensity fields while the larger particles can. In this fashion, the smaller particles exit the intensity field at a different location than the larger particles, and the particles are therefore effectively sorted [112, 113].

While scanning optical tweezers can have a wide variety of uses, it cannot provide trapping strength or precision greater than the traditional optical tweezers on which it is based. It actually requires more total laser power to generate forces of similar strength as the power is widely distributed over a larger area. In addition, the relative phase of the light at different positions in the intensity field cannot be controlled. For experiments requiring that the phase of light at each position in the intensity field is equal, the scanning method cannot be used. I will perform such experiments which are sensitive

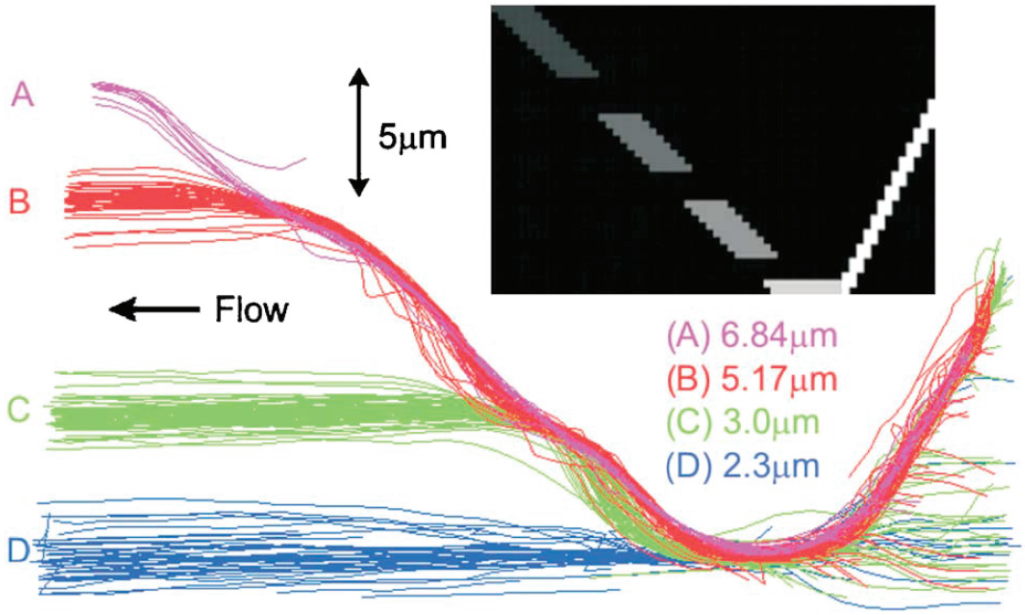

Figure 1.8: Sculpted intensity field by scanning optical tweezers for particle sorting. A flow of four different diameter particles is directed by the shaped intensity field which is indicated by the gray-scale inset. White indicates high intensity and black zero intensity. The smaller particles are not affected by the lower intensity regions while the large particles are, allowing for efficient sorting of particles by size. Figure adapted from reference [112].

to the phase of incident light at all positions in the optical field in Part II of this dissertation.

1.5.3 Extended Traps

Rather than scanning a point focused single beam trap in order to generate a custom intensity field, it is also possible to use additional optical elements to shape the wavefront of the incident beam. The simplest example of this is to use an additional lens, for example a cylinder lens, to stretch

the point focus of the optical tweezers into a line focus or other shape [115–129]. The main advantage of this technique is the simplicity of implementation since they generally only require insertion of an additional lens, rather than a series of computer controlled scanning mirrors or acousto-optical modulators. Another advantage is preservation of the relative phase of light at all positions in the stretched light field, whereas in the scanning tweezers the relative spatial phase coherence is destroyed. However, the drawback to this technique is the lack of a point focused beam. For example, in the case of using a cylinder lens to generate a line focus, the beam is only tightly focused in one dimension. We know that the stability of the trap in terms of the ratio of the gradient force to the destabilizing scattering force is strongly dependent on how tightly focused the laser beam is (see equation (1.12)). By focusing in only one dimension, the scattering force quickly begins to dominate over the gradient force and thus the trapped particles are very unstable. When this method is used, either the particles must be pressed against the surface [115, 116, 121], the particles must be very large ($> 1\mu m$) [117, 123], or sub-micron particles can only be trapped for very short timescales [118]. These drawback prevent me from using this technique as it stands, however the advantage of the uniformity in the phase of light is of critical importance to my measurements. I will propose a modification to this technique by combining it with the standing wave geometry in order to dramatically increase stability and precision.

Another way to generate extended optical fields is to use a reverse imaging technique. Rather than use a laser beam which is focused by the

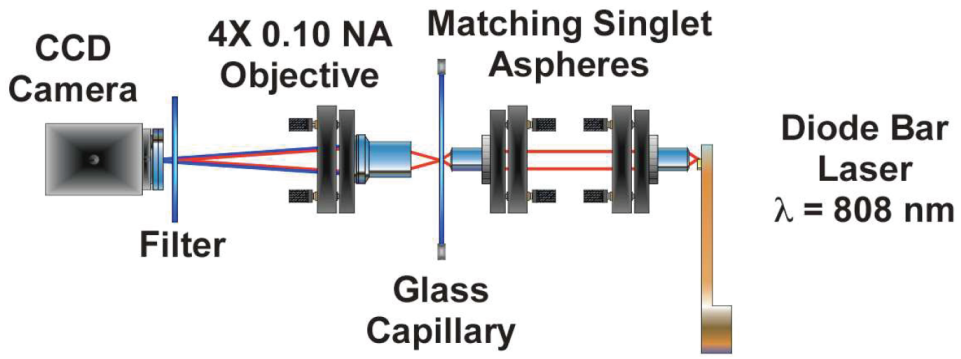

Figure 1.9: Technique for generating optical trapping regions of various geometries by reverse imaging. An emitting object (a diode laser bar) is imaged onto the sample plane thereby generating an intensity field of the same geometry. Particles can then be trapped and aligned in the shape of the emitter. Figure from reference [131].

objective lens to generate a trapping region, we begin with an already sculpted external light field which is then imaged onto the sample plane. Figure 1.9 shows how a diode bar laser is used as the emitter and is imaged onto the sample thereby generating an intensity field of the same geometry (a long line in this case) [130–132]. Particles can then be trapped and aligned in the high intensity region. I suspect one could even use an array of many emitting diodes, or emitters of varying geometry or wavelength thereby projecting the emitted geometry onto the sample plane. However, I have search and not found a report of this particular evolution of the method. In addition, it should be possible to dramatically "shrink" the scale of the original external light pattern as it gets imaged into the sample, but I have not seen this reported in the literature either. In any case, it is not possible for this technique to beat the diffraction limit of a traditional point focused laser beam and suffers from

similar drawbacks to the line focused traps discussed above.

1.5.4 Holographic Optical Traps

It is also possible to shape of the intensity pattern using holographic methods [77, 114, 133–154]. Holography is especially useful because it allows for nearly complete control over the phase and direction of the laser wavefronts. Figure 1.10 shows a schematic of a typical holographic optical trap design. The incident laser is first reflected off of a spatial light modulator (SLM). The SLM is an array of pixels, similar to an led display, which can be controlled by a computer program. Each pixel is able to retard the phase of light by a specific amount through electronically controlled variation of the refractive index [155]. Thus when the beam is reflected off the SLM, the wavefront is no longer uniform but rather propagates as a custom diffraction pattern. For example, the incident laser beam can be reshaped to propagate as though it were an array of many incident parallel beams which can then all be focused into the sample chamber. Thus, an array of particles can be trapped within the sample chamber as shown in figure 1.10. The wavefront can further be modified such that some beams are either diverging or converging before entering the focusing objective lens thereby generating optical traps in a plane other than the focal plane. This is the basic principle for using holographic optical traps for manipulating multiple particles in all three dimensions, but nearly any geometry of the intensity patter can be constructed (for example: interlocking rings [153]), and the wavefronts can even be designed to apply torques to

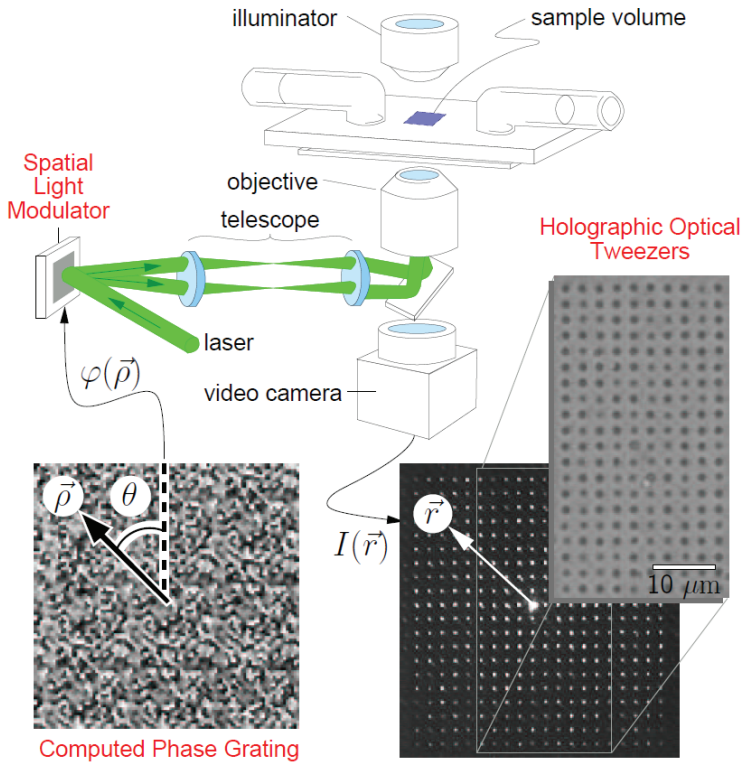

Figure 1.10: Schematic of a holographic optical trap. The incident laser beam is first diffracted off a computer controlled spatial light modulator. The holographic image is formed within the sample chamber allowing for 3D control of multiple particles. Figure from reference [134].

objects [138, 154, 156].

In addition to trapping of objects, holographic tweezers can be used to guide and sort objects within a fluid flow. Such techniques are known as optical fractionation. Figure 1.8 is an example of optical fractionation, although it was not based on holographic tweezers but rather rapidly scanned tweezers. However, holographic optical tweezers have received the most attention for this technique as they can potentially be more easily implemented for industrial

applications [135, 137, 148, 157].

While holographic optical tweezers have many uses, there are also drawbacks. Mainly, the wavefronts generated by the SLMs are not very precise. As I've described, the SLMs are composed of many pixels, and these pixels have finite size on the order of $40\mu m$ in both length and width [155]. This size is much larger than the wavelength of the incident light, and so it is not possible to generate a diffraction wavefront with perfect precision. This leads to focusing of the beams within the sample chamber to form focal spots that typically are distorted and are larger than the diffraction limit. Thus, only large particles ($> 1\mu m$) can typically be trapped and high precision positioning of the particle is lost. In the future, higher resolution SLMs may make holographic tweezers a more viable option for high precision and nanoscale applications.

1.5.5 Optical Conveyor Belts

While holographic optical traps utilize diffraction patterns to generate multiple trapping volumes in the sample plane, there are also methods which utilize the interference of multiple beams. In particular, optical conveyor belts demonstrate precise control of the phase of the interfering beams in order to generate transport of objects over long distances and can be used in either a standing wave trap geometry [150, 158–168] or an evanescent field trap geometry [165, 169–173]. Figure 1.11 shows images of particles being transported by a typical optical conveyor belt using a standing wave generated by two counter-propagating Bessel beams. By precise variation of the phase of one of

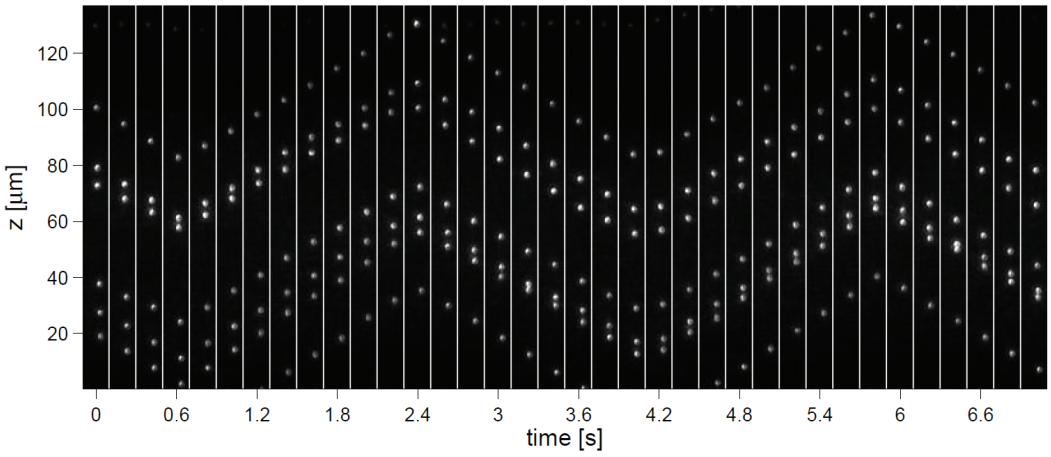

Figure 1.11: Images of particle transport in a typical optical conveyor belt. Particles are trapped in the standing wave of two counter-propagating Bessel beams. By manipulating the phase of one of the beams, the standing wave is moved thereby also transporting the particles. The particles are $410nm$ diameter polystyrene. Figure from reference [161].

the beams, the standing wave pattern can be translated thereby transporting the particles which are confined in the antinodes.

The main advantage of this technique, aside from the ability to transport particles, is the strength of the confinement which can be achieved using the standing wave geometry. As I discussed in chapter 1.4, generation of a standing wave pattern both increases the gradient force and at the same time eliminates the destabilizing scattering force. Thus, trapping and transport of particles as small as $200nm$ in diameter has been achieved. When used in combination with advanced cooling techniques, even single atoms can be transported by this method [158, 162].

However, this method has its flaws as well. Bessel beams have a self

reconstructing, or "self healing," wavefront which allows them to propagate long distances with little diffraction. This is used to generate long standing waves deep within the sample chamber. Yet, the axicon lenses (cone-shaped lenses) used to generate these Bessel beams are known to generate flaws in the beam wavefront due to the axicon tips which are not perfectly sharp but are rounded and thereby reduce trapping stability. Furthermore, the technique utilizing Bessel beams appears to require immense laser power of over $1W$ in order to trap such small particles, and significant heating of the water within the sample chamber in this case has been documented [161]. If water, which has a nearly minimum absorbance at the wavelength used ($\lambda = 532nm$), is susceptible to heating, then this kind of laser power and heating would likely damage biological material or hinder measurements dependent on the thermal fluctuation of the trapped particles. Metal particles, which are an object of interest for my work (see Part II), are particularly susceptible to heating.

In the case of the evanescent field variation of the optical conveyor belt, Bessel beams are not needed, and the laser intensity may be distributed over a large area. However, the problem here is that the particles are pulled into contact with the surface, as discussed with general evanescent wave trapping in chapter 1.5.1. Therefore, while the optical conveyor belt has many advantages, its significant disadvantages prohibit me from using this method as it currently stands. Yet is is clear that utilizing standing waves can provide the most stable method of trapping nanoparticles free in solution.

1.6 Outline of Research Objectives

Although there are many different methods of optical manipulation available, none are able to meet all the requirements for stable trapping of nanoscale particles free in solution, and in a geometry which allows for free movement of particles within a static optical field. For example, the extended trapping or scanning techniques generate confinement along paths of many different geometries, however they have not been shown to effectively trap sub-micron particles. Conversely, the standing wave optical trap has proven its ability to trap nano-objects, but its point focused beam does not allow particles to freely move over long range.

In the next chapters, I will discuss the development of two new instruments which combine the standing wave optical trap geometry with extended trapping techniques. I will show that these new instruments are capable of achieving trapping of nanoparticles in extended optical fields using minimally focused or completely collimated beams. One such geometry is a one-dimensional tube-like confinement which I call the standing wave optical line trap (SWOLT) and is described in chapter 2. The other geometry is a two-dimensional planar confinement which I call the pancake trap (PT) and is described in chapter 6.

In chapters 3, 4 and 5 I describe a method for generating and using additional scattering force components in these traps to push particles to new positions in the optical field without altering the intensity field itself. Thus, the trapping by the gradient forces remains unaffected. This transport can be

generated by either varying the angle of the incident beam thereby pushing particles in one direction, or by focusing and de-focusing the beam which pushes particles toward or away from the optical axis.

After fully developing the instruments and characterizing their function, I will use these instruments to study fundamental optical interactions between nanoparticles. Aside from the optical scattering and gradient forces which are forces applied to objects directly by the incident beam of light, there is also a force known as the optical *binding* force which is an interaction between two or more particles in an optical field. While this optical binding force has been observed and studied for over 20 years, direct quantitative measurements of this force between Rayleigh particles have so far been out of reach. I describe the current state of measurements on the optical binding force in chapter 8. By monitoring the movement of nanoparticles in the SWOLT and pancake trap for long timescales, I can gather orders of magnitude more statistics of the optical binding interaction and accurately quantify the forces and interaction energy landscape. Chapter 9 describes the measurements of binding force in 1D using the SWOLT, and chapter 10 describes the measurement of the 2D energy landscape using the pancake trap.

Finally, I will use the wide optical field of the pancake trap to observe the self-assembly of "optical matter," formations of multiple nanoparticles bound together only through optical binding forces. These cluster formations have been previously predicted through numerical simulation, but have never been observed experimentally. I can then monitor the bulk motion of the

clusters in the trap to determine if the coupling to the external optical field may be dependent on the specific geometry of the clusters. These measurements are also described in chapter 10.

Chapter 2

The Standing Wave Optical Line Trap

2.1 Introduction

With the introduction of the optical tweezers by Ashkin in 1986 [44, 46, 47], fields such as biophysics, colloidal physics and nanotechnology have widely adopted it as a tool for manipulating and applying external forces on micro-scale objects [67, 75, 100, 138, 165]. While standard optical tweezers are commonly used to manipulate single objects, the development of new methods for multi-particle manipulation has recently become of great interest. For example, optical methods for sorting and mixing of particles as part of lab-on-chip devices have been the focus of many studies, also known as optical fractionation [135–137, 139, 144, 148, 157]. There has also been much effort in optical methods for continuous transport and delivery of many particles along defined pathways using extended optical traps or optical conveyor belts (see chapter 1.5). However, these techniques have only been shown to be effective for manipulating individual particles larger than about $1\mu m$ in diameter, require immense laser power or pull the objects into contact with a hard surface.

Our goal is to develop a technique that can manipulate nanoparticles free in solution using low laser power and allows for continuous optical trans-

port. Such a technique would be highly beneficial for sorting, mixing and assembly of not only synthetic particles such as individual carbon nanotubes, but also for biological particles such as small vesicles. With this goal in mind, we base our technique on the standing wave optical trap (SWOT), which has been shown to produce stronger intensity gradients and deeper potential wells compared to a single beam trap (SBT) of the same power and is able to trap nanoparticles free in solution [88–94]. In a SBT, a laser beam is typically focused by a high numerical aperture lens in order for the axial gradient force to overcome the axial scattering force. This requirement is eliminated in a SWOT due to the compensation of the axial scattering force by the reflected beam [88–94, 146, 147, 149] and because the axial gradient force is still generated by the standing wave pattern even if collimated beams are used. This advantage allows us to generate a highly stable standing wave optical line trap (SWOLT), even though we have only focused the trapping beam in one dimension. I use the SWOLT to confine nanoparticles to a precise pathway where the transverse thermal position fluctuations of the particles are still smaller than their diameter. This is important, for example, for the precise ordering and assembly of nano-objects.

While the precise confinement of nano-particles is a necessary step in an assembly process, it would be desirable if the particles could be manipulated independent of this confinement. Here I show that the SWOLT can generate a *lateral* component of the scattering force which can be used for unidirectional or bidirectional continuous transport out of the trap or for forcing the

aggregation of particles. This lateral component of the scattering force can be controlled *independently* of the confining gradient force through the lateral and axial translation of the cylinder lens that is used to generate the SWOLT. The elegant design of the SWOLT allows me to derive a simple ray optics model (and consequently a simple mathematical expression) which describes the forces generated on particles in the SWOLT trapping volume.

2.2 Instrument Design

The design of the SWOLT is similar to that of standard single beam traps but with a few additions. Figure 2.1 shows a schematic diagram of the SWOLT. The system is designed around an inverted microscope (Axiovert 100, Carl Zeiss, Germany). Objects are imaged using the microscope's built-in differential interference contrast (DIC) components which include the condenser lens, Wollaston prisms, polarizer, analyzer and a halogen lamp as the light source. A CCD camera (Rolera-XR Fast Cooled, Q-Imaging, Surrey, BC, Canada) is used to capture real time videos of the particles. A 1064nm wavelength single longitudinal mode laser (CL1064-1W0-S, CrystaLaser, Reno, NV, USA) is coupled into a single mode polarization preserving fiber optic cable (PMC-980/1064-6 4-NA012-3-APC-500-P, Schäfter and Kirchoff GmbH, Germany). The coupling optics of the fiber expand the beam to about 5mm in diameter in order to overfill the back aperture of the objective lens. The objective lens (Plan-Neofluar 100x/1.3 Oil Pol, Carl Zeiss, Germany) is used both for imaging and for focusing the laser onto the surface of a dichroic coverslip

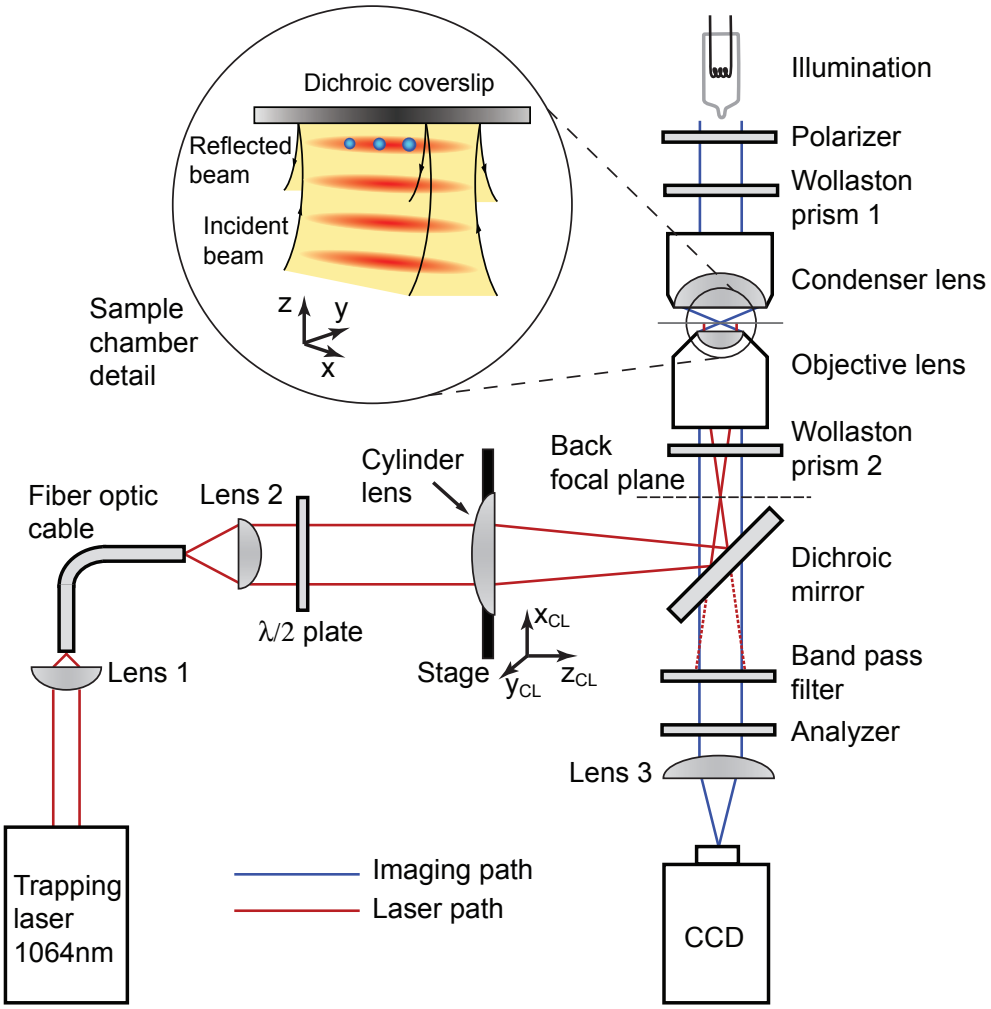

Figure 2.1: Schematic of a standing wave optical line trap. The design is based on a standard single beam trap design [75, 174], but with two additions. A dichroic coverslip is used as part of the sample chamber to generate a standing wave optical trap. The cylinder lens is used to stretch the trapping volume into a line, and translation of the cylinder lens generates lateral components of scattering force which drive transport along the line. Many imaging techniques can be used with the SWOLT, such as dark field microscopy. Figure 6.1 shows a similar setup using dark field. See also figure 9.1 for a 3D illustration of the trapping volume. Figure from my publication [175].

(1064nm reflectivity $> 99\%$, Institute of Scientific Instruments of the ASCR, Czech Republic). The incident and reflected laser beams interfere and generate a standing wave trap within the sample chamber (see figure 2.1 inset). The sample chamber volume is typically filled with deionized water along with the sample to be studied. A $\lambda/2$ plate is used to change the polarization angle of the incident laser beam such that it is not split in two by the Wollaston prism. Finally, a cylinder lens (LJ1653RM-C, $f = 200mm$, Thorlabs, Newton, NJ) is inserted in the beam path in order to transform the SWOT into a SWOLT. This is done by focusing the laser beam onto a line localized on the back focal plane of the objective and centered on the optical axis. We will call this the "default" alignment. The first trapping volume near the dichroic coverslip is nearly diffraction limited transverse to the long axis (y-axis) of the line trap. The width of the elongated Gaussian intensity profile along the line trap (x-axis) is determined by the diameter of the incident laser beam, the focal length of the cylinder lens, and the back focal length of the objective lens. The focusing axis of the cylinder lens (x_{CL}-axis) corresponds to the elongated axis of the trapping beam (x-axis), thus the SWOLT can also be rotated through rotation of the cylinder lens. We will show that particles can be manipulated by translating the cylinder lens laterally or axially from the default position. Thus, the cylinder lens is mounted on an XY stage for precise translation perpendicular to the beam path, and the XY stage is attached to a rail system that permits long-range translation of the cylinder lens along the optical axis. This allows the cylinder lens focal line to be positioned relative to

the back focal plane of the objective lens in order to generate either collimated, converging, or diverging trapping beams within the sample.

A simple check to see that the system is correctly producing a line focus is to directly image the focal spot (actually a focal line). Since the same objective is used for imaging objects in the sample as well as for focusing the laser, the imaging plane is equivalent to the focal plane. To see an image of the focal spot (which is the object of imaging), we need to use the dichroic coverslip to reflect the rays back to the objective lens. Thus we really create a virtual object of the focal spot which is in a plane behind the dichroic surface. Therefore the only instance in which this virtual focal spot and the imaging plane can be coplanar is to focus the objective lens directly onto the surface of the dichroic coverslip. Any translation of the objective lens along the optical axis away from this position will cause the image to be out of focus and we will see the point spread function of the focal spots. Figure 2.2 shows example images of a point focused spot and a line focused spot. The intensity distribution can be easily rotated by rotating the cylinder lens accordingly but otherwise does not change significantly. In addition, the axis of rotation is at the same location where the point focused trap is located in figure 2.2a which indicates good alignment of the optical system.

2.3 Trapping and Alignment of Nanoparticles

The ability of the SWOLT to stably trap and align nanoparticles over a long length-scale is demonstrated in figure 2.3. Particles can be seen to be

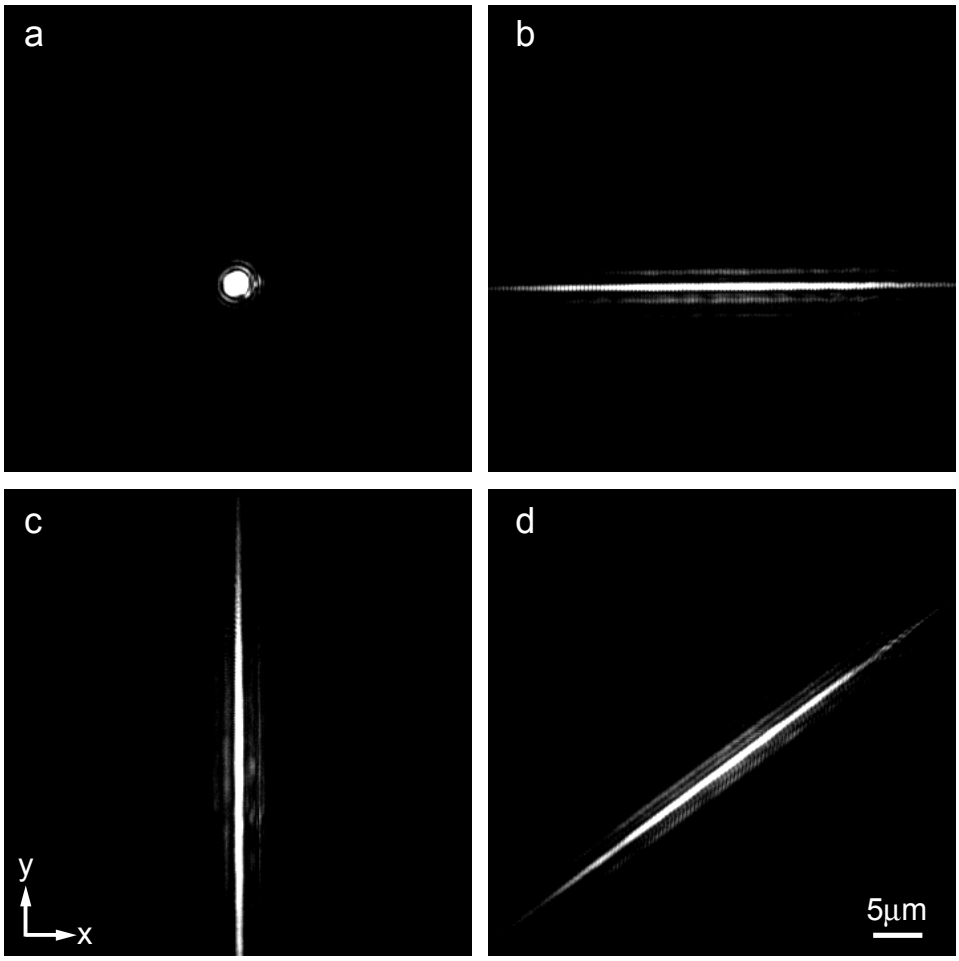

Figure 2.2: Images of the standing wave optical line trap intensity distribution in the xy-plane. Images were recorded by removing the band pass filter from the experimental setup (see figure 2.1) thereby allowing some laser light to reach the camera. Since I focus the the laser onto the surface of the reflecting coverslip with the objective lens, the imaging and focal planes are coplanar and the image of the focal spot/line are projected onto the CCD camera. a) Image of a point focused laser (cylinder lens removed). b), c), & d) When the cylinder lens is inserted, the point focus is stretched into a line focus. By rotation of the cylinder lens, the orientation of the focal line is correspondingly rotated. This allows for precise alignment and orientation of elongated trapped objects, or for changing the path of transported objects.

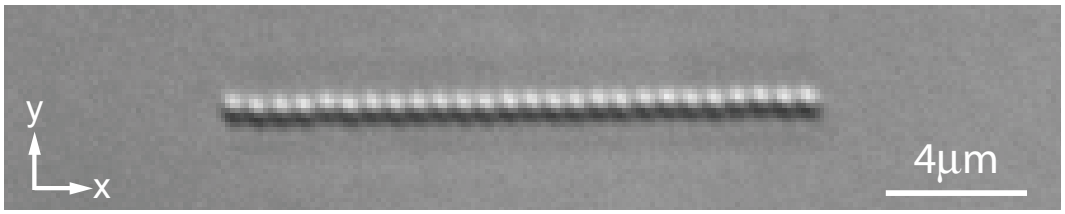

Figure 2.3: Trapping and alignment of $500nm$ diameter polystyrene particles in the SWOLT. Stable trapping and alignment of 26 polystyrene nanoparticles is demonstrated using $70mW$ of laser power in the focal plane. The aligned particles maintain a precise ordering (they can not pass each other) demonstrating the precision of the alignment even over the long SWOLT length. Particles are imaged using DIC microscopy.

well aligned along the SWOLT length, and the alignment axis can be rotated easily by rotating the cylinder lens as shown in figure 2.2. The confinement along the y- and z- axes is strong enough to reduce thermal fluctuations of the particles along those axes to significantly less than the particle diameters (see also chapter 2.4). Therefore the trapped particles cannot "pass" each other along this chain, but rather they maintain their precise ordering along the length of the SWOLT. This is the equivalent of confinement to one dimension, as in a channel or tube. This trapping geometry generated by the SWOLT can be used for many studies requiring confinement to 1D, but would otherwise suffer from proximity to surfaces such as attempts to experimentally quantify single file diffusion [176–185]. Single file diffusion plays a major role in many biological functions, such as the transport of molecules through ion channels [186–191], and therefore development of an experimental model system would prove useful in further research studies.

The ability of the SWOLT to stably trap and align even smaller nanopar-

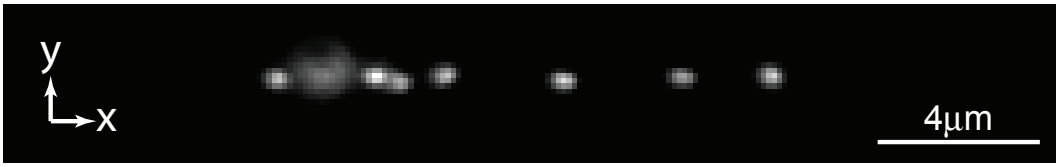

Figure 2.4: Trapping and alignment of nanoparticles in the SWOLT. Gold particles $100nm$ in diameter were stably trapped and aligned in the SWOLT with $70mW$ of laser power in the focal plane. Particles are imaged using dark-field microscopy. The particle second from the left is trapped in the second antinode of the standing wave and thus is out of focus. Figure from my publication [175].

ticles at low laser power is demonstrated in figure 2.4. The compensation of the scattering force increases the stability of the SWOLT when compared to a single beam trap (SBT). Particularly for metallic particles in a SBT, the strong scattering forces push them along the optical axis to positions away from intensity maximum where they become less stable. Thus higher laser powers are generally required for stable trapping compared to a SWOT. For example, $97nm$ diameter gold particles were trapped with $30mW$ of laser power in an optimized SBT [192, 193]. Here we use $70mW$, but when comparing the theoretical power density of the diffraction limited Gaussian focal spot of the SBT ($\sigma_x = \sigma_y \approx 0.5\mu m$) with the extended SWOLT ($\sigma_x \approx 15\mu m$, measured from direct images of the SWOLT intensity profile, and $\sigma_y \approx 0.5\mu m$), and even accounting for a factor of 4 increase in power density due to the standing wave, the required power density of the SWOLT is still at least 3 times lower at the intensity maximum. Particles were also stably trapped far away from the intensity maximum of the SWOLT (along the x-direction) where the power density can be nearly an order of magnitude lower compared to the center of a SBT.

Despite the low power density, the gold nanoparticles are well aligned within the SWOLT. Using video analysis to track the particle positions, the measured standard deviation of the transverse (y-axis) thermal fluctuations along the length of the trap explored by the particles is only $36 \pm 4nm$ (determined by a Gaussian fit to the position data) which is smaller than their radius. Thus the probability that they reorder themselves along the SWOLT is very low which is desirable for the assembly of nanoparticles in a precise order.

2.4 Measurement of the SWOLT Trapping Stiffness

While it is possible to trap, align, and manipulate such small particles in the SWOLT, their diameter is below the diffraction limit. This makes the quantification of the trap properties difficult. Although we can distinguish individual 100nm gold particles from aggregates based on the scattering intensity (for example doublets appear roughly twice as bright as an individual), the center of an individual particle cannot be tracked if particles aggregate. Therefore, we use $500nm$ diameter polystyrene particles, easily resolved in conventional DIC microscopy, for many of the following experiments which will characterize the SWOLT.

To determine the trap stability we observed a 500nm diameter polystyrene particle diffusing in the SWOLT for 2 hours (see figure 2.5a) and calculated the position histogram. The longitudinal (x-axis) as well as the transverse (y-axis) probability distributions follow a Gaussian profile that corresponds

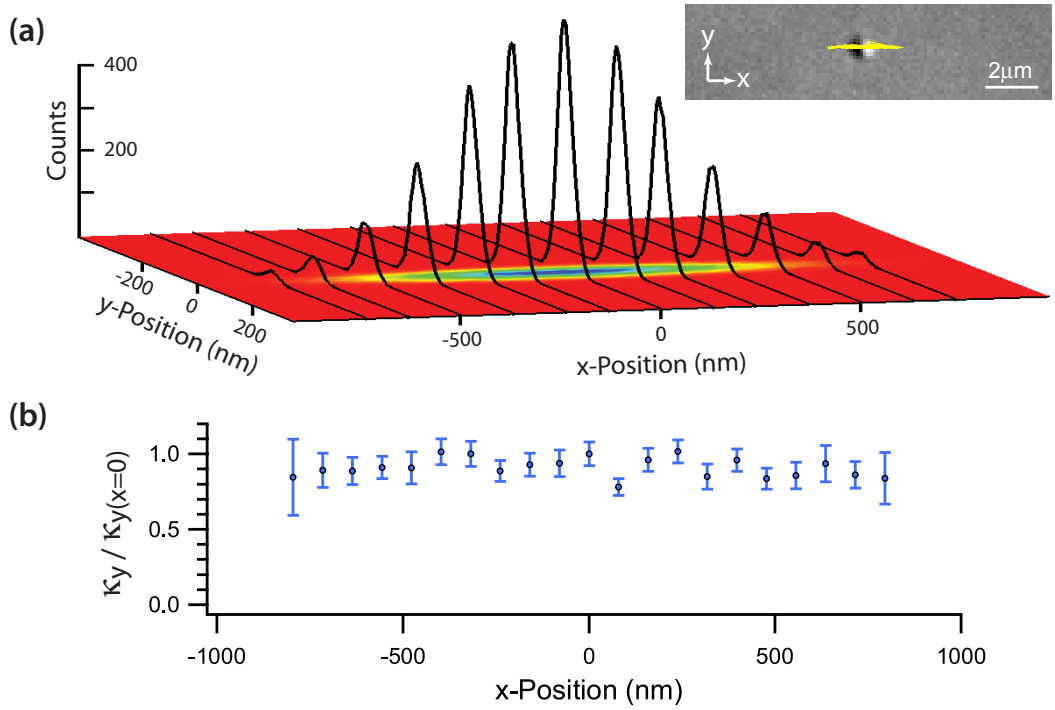

Figure 2.5: Characterization of the SWOLT's trapping potential. a) Position histogram of a $500nm$ diameter polystyrene bead diffusing in the SWOLT for 117 minutes (1.4×10^5 data points). The base image shows the full 2D histogram data. The black curves are individual line profiles of histogram data for a given x-position averaged over $\pm 65nm$. The inset shows a sample DIC image used to track the bead. The yellow line indicates the path of the center of the particle over 30sec. b) The transverse spring constant κ_y of the trap at different positions along the trap length. Values are normalized to the value at $x = 0$, $\kappa_y(0) = 2.6 \pm 0.2 pN/\mu m$. The trapping power in the focal plane was about $70mW$. Figure from my publication [175].

to a harmonic potential. The width of the probability distribution along the x-axis (at $y = 0$) is $385 \pm 4nm$ and along the y-axis (at $x = 0$) is $36.9 \pm 0.4nm$. The corresponding spring constants are $\kappa_x = 0.025 \pm 0.002 pN/\mu m$ and $\kappa_y = 2.6 \pm 0.2 pN/\mu m$. The errors in these values are determined from least-squares

fitting of the data. The small fluctuations along the y-axis underline the strong transverse confinement of the particle by SWOLT while the confinement along the trap is weak, allowing the particle to explore more than two micrometers by thermal excitation. The aspect ratios are approximately 10:1 for the position fluctuations and 1:100 for the force constants. As expected, the transverse force constant κ_y is nearly invariant over the explored length of the trap (see figure 2.5(b)) which indicates a tube-like confinement of the particle. The uniform transverse confinement also suggests that the SWOLT extends much further out, but these parts of the SWOLT are not accessible by thermal fluctuations under the given experimental conditions. To also explore these parts of the SWOLT, we use two additional methods: change of the average particle position by the lateral component of the scattering force and the measurement of the flow velocity of the particle after it is captured by the SWOLT. These methods are described in Chapters 3 and 4.

2.5 Trapping and Guiding Live Swimming Bacteria

The ability of the standing wave optical line trap to stably confine objects to a one-dimensional channel, even at low laser power, opens the door for interesting new experiments. For example, biological experiments in which cells need to be ordered and observed for long timescales can be performed. Figure 2.6 shows several bacterium (Bacillus subtilis) aligned in the SWOLT. The strong confinement of the bacteria to 1D effectively maintains their ordering, even as they undergo cell division.

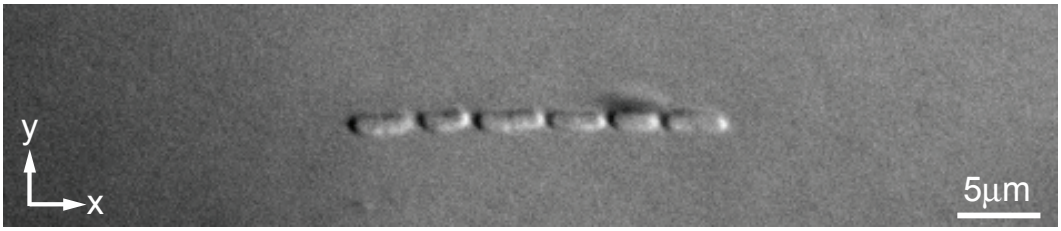

Figure 2.6: Bacteria (Bacillus subtilis) trapped and aligned in the SWOLT. Images using DIC microscopy. The bacteria shown here were not able to swim, and so were easily trapped (see figure 2.7 for swimming bacteria). Cell division was observed for a few of the bacteria in the SWOLT, however the medium was likely deprived of nutrients and so prevented normal division. The SWOLT provides the possibility for alignment and observation of biological objects using low laser power and free from surface contact.

In the case of swimming bacteria, the SWOLT can be used to guide their motion without imposing solid walls. Figure 2.7 shows an example of a swimming bacterium being guided by the SWOLT. In the future, experiments may be done which study the 1D motion of swimming bacteria without the presence of a hard surface which is known to significantly affect the swimming behavior. On the other hand, the SWOLT can also be used to probe the surface effects even further, in a controlled fashion. With proper positioning of the SWOLT, bacteria can be guided to swim parallel to a hard surface. The distance from the surface the bacteria swim can then easily be varied by repositioning the SWOLT, and the swimming behavior as a function of distance from the hard surface can be studied in detail. This is just one example of potentially many biological experiments that can be done with the SWOLT. However I will focus on the purely optical phenomena, which is surprisingly rich, for much of this dissertation.

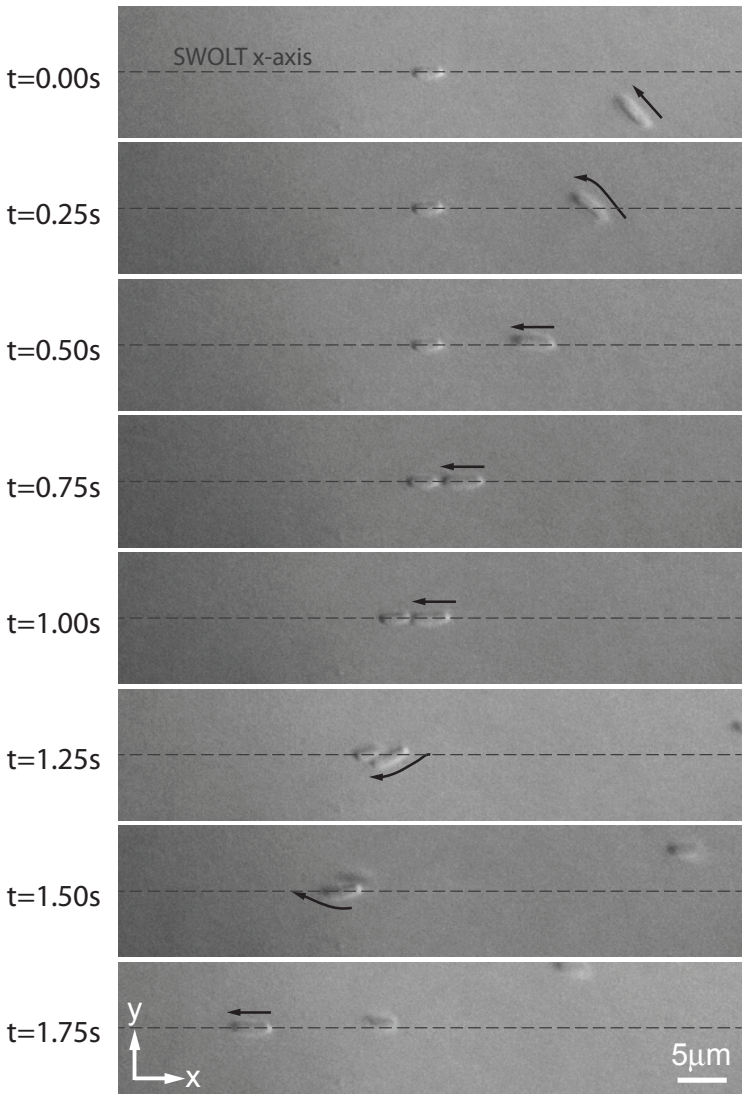

Figure 2.7: Excepts from video of bacteria (Bacillus subtilis) swimming through the SWOLT. At this laser power ($P \approx 70mW$), the bacteria swim too strongly to stay in the SWOLT. One bacterium is likely dead (not from the trap) and thus rests at the center of the SWOLT. A passing bacterium swims by but is guided by the SWOLT to change directions and swim along the SWOLT axis, pushing into the dead bacterium and swimming around it for a moment. Images taken using DIC microscopy.

2.6 Summary

Two new optical trapping instruments were described and tested. In chapter 2, the details of the standing wave optical line trap (SWOLT) design were presented, and the instrument was shown to achieve the intended functionality. Primarily, the SWOLT was shown to effectively confine nanoparticles to a one-dimensional tube-like channel free in solution. Transverse particle fluctuations in the SWOLT were measured to be smaller then their diameter which is sufficient to maintain the order of the particles along the channel. Twenty-six $500nm$ polystyrene particles were simultaneously trapped in the SWOLT indicating the long length scale (tens of μm) with which particles can be precisely aligned. Several $100nm$ diameter gold particles were also stably trapped using 3 times less laser intensity than previously reported. This indicates the efficiency of the SWOLT for trapping nanoparticles with low laser power. Finally, live bacteria were trapped and aligned in the SWOLT, again showing that living biological objects can be trapped with little photodamage.

Chapter 3

Uni-Directional Manipulation in the SWOLT

3.1 Generating Lateral Scattering Force Components

In the experiments described in Chapter 2, the SWOLT was aligned so that the scattering force from the incoming and reflected beam compensated each other completely, i.e. when the trapping beam along the x-direction is normal to the dichroic coverslip. However, the situation where the scattering force is completely compensated is only a special case of the SWOLT. The collimated beam parallel to the optical axis (z-axis) is generated in the sample chamber by focusing the trapping laser beam on the center of the back focal plane of the objective lens. By translating the cylinder lens perpendicular to the optical path, a lateral component of the scattering force ($\vec{F}^s_{net}$) will be generated (see figure 3.1).

The dashed lines show representative light rays for the case of zero net scattering force. The solid lines show the path of those rays after the cylinder lens has been shifted by δx_{CL}. The cylinder lens focal line still lies within the back focal plane of the objective lens, thus the beam still emerges as collimated, but the incident angle (θ_m) of that collimated beam changes. Since the beam no longer propagates normal to the reflective surface of the

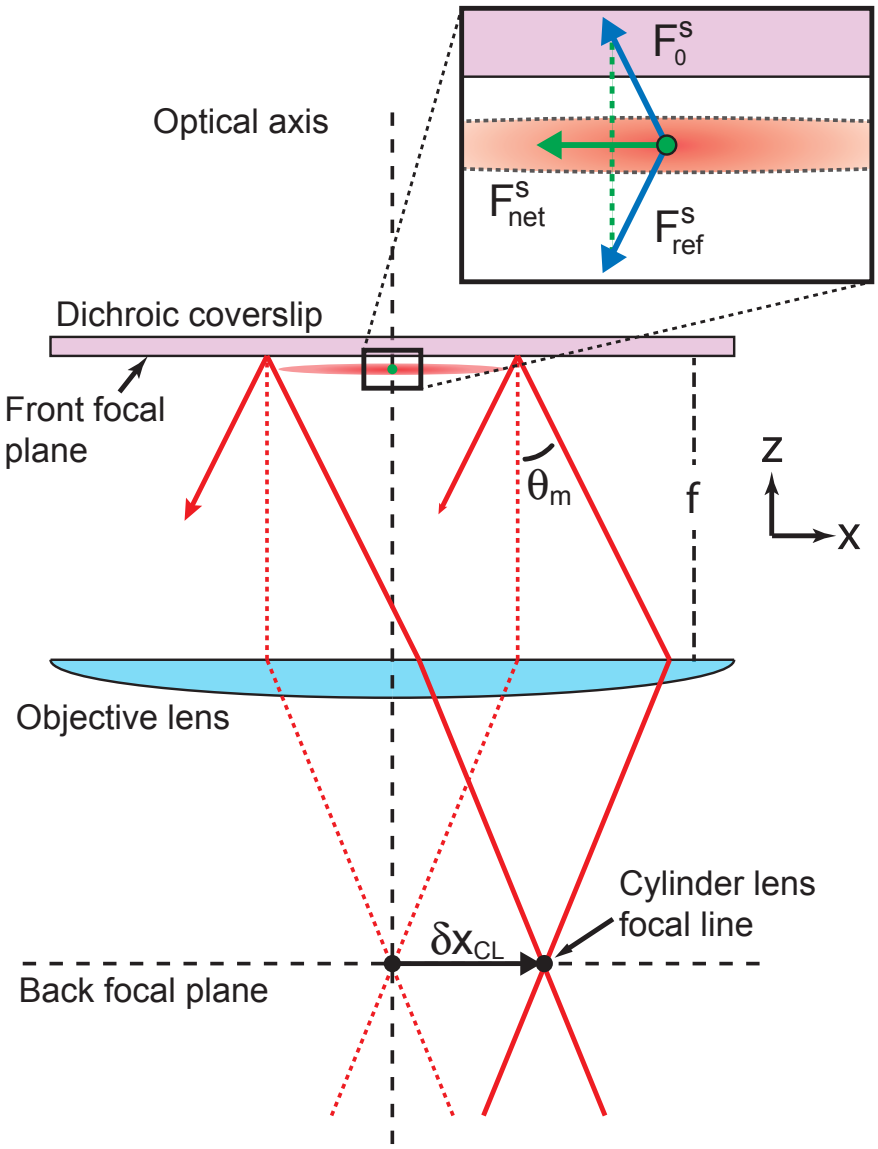

Figure 3.1: Ray optics diagram illustrating how the lateral component of the scattering force ($\vec{F}_{net}^s$) is generated by shifting the cylinder lens along the x_{CL}-direction. While the z-component of the scattering force is compensated by the reflected beam, the lateral component is amplified. This enables transport of particles along the length of the SWOLT. Figure from my publication [175].

dichroic coverslip, there is a lateral component of the scattering force ($\vec{F}^s_{net}$) while the axial components of the incoming and reflected beam still cancel each other out. The lateral components of the two beams add, amplifying its strength. The lateral scattering force can be used to push particles to different regions along the length of the SWOLT. To illustrate the action of the lateral scattering force, the cylinder lens was shifted in steps of $50\mu m$, and a 2D position histogram was obtained for each position of the diffusing particle. Figure 3.2 shows the average position of the particle for different positions of the cylinder lens. Note that the particle can be pushed over a range of $30\mu m$ to $40\mu m$ by a modest shift of the cylinder lens (range of incident angles about $\pm 13^{\circ}$) due to the strength of the lateral scattering force.

To exclude that the longitudinal shift of the particles position is caused by a longitudinal displacement of the SWOLT while changing the position of the cylinder lens, we imaged the position of the trap and analyzed its strength. Although it is expected that the shift in the average position of the trapped particle is due to the lateral scattering force, any changes in the gradient force also need to be considered since the resting position of the particle is the point where the scattering and gradient force compensate each other. By examining the ray diagram in figure 3.1 it is expected that the gradient force distribution will be unchanged as the cylinder lens is shifted. The solid light rays (representing a non-zero angle of incidence of the trapping beam on the dichroic coverslip) are parallel to the dashed light rays (representing normal incidence of the trapping beam) before entering the objective lens, so when

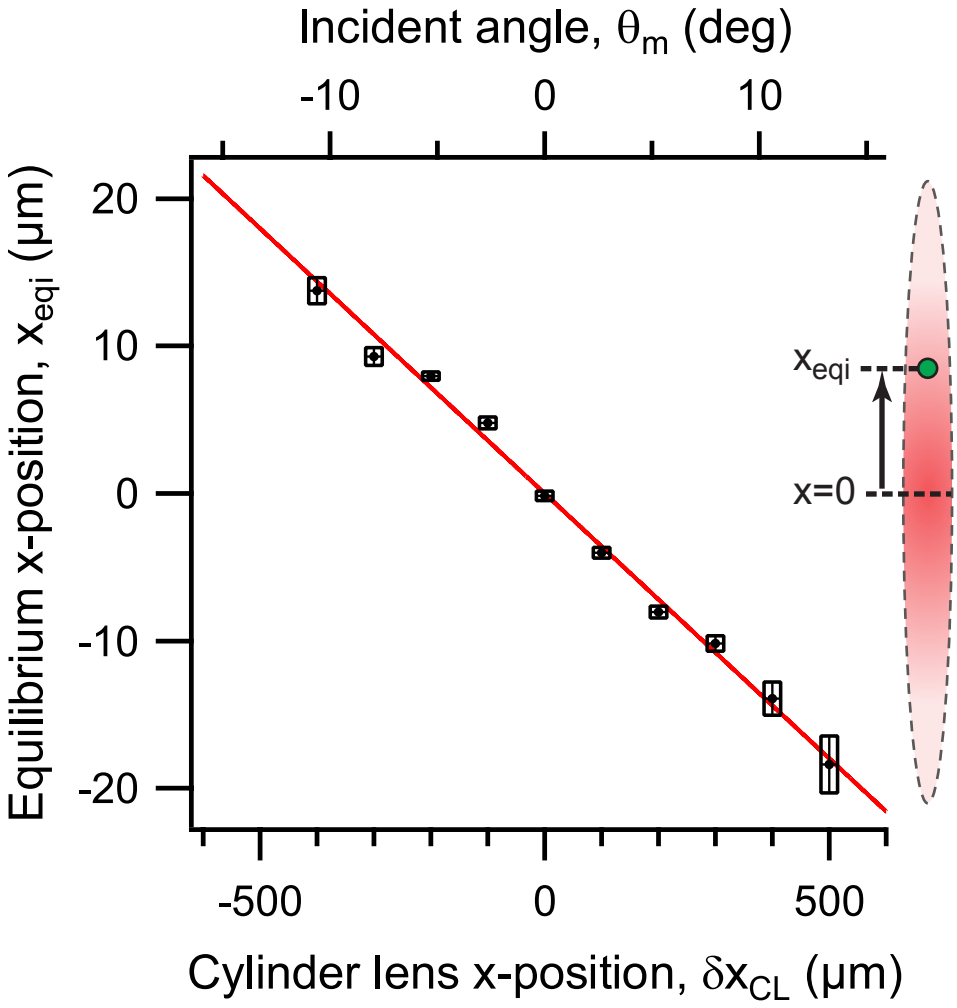

Figure 3.2: The average position of a trapped $500nm$ diameter polystyrene particle in the SWOLT is shown for different positions of the cylinder lens. The value $x_{eqi} = 0$ corresponds to a selected pixel on the CCD camera near the x-position of the intensity maximum when $\delta x_{CL} = 0$. The vertical error bars represent the standard deviation of the position. The solid red line was fit to the data using the model for the SWOLT described in the text (equation (3.9)). The parameters used for the fit are shown in table 3.1. The incident angle (θ_m) was calculated from cylinder lens position (δx_{CL}) using equation (3.6). The inset illustrates an example of the particle position within the trapping volume's intensity profile. Figure from my publication [175].

$D = 4277\mu m$	$NA = 1.3$	$\kappa_x = 25\frac{fN}{\mu m}$
$n_m = 1.33$	$n_p = 1.55$	$\lambda_0 = 1064nm$
$I_0 = 3.0\frac{mW}{\mu m^2}$	$\|\vec{F}^s_{00}\| = 0.98 \pm 0.03pN$	

Table 3.1: Parameters used for the fit to the data in figure 3.2 using equation (3.9). The diameter of the back aperture of the objective lens (D) as well as the numerical aperture (NA) were given by the manufacturer; the refractive index of the medium, water (n_m), is known; the longitudinal spring constant (κ_x) was measured as described in the text; and the magnitude of the incident scattering force at $x = 0$ ($|\vec{F}^s_{00}|$) was determined by fitting equation (3.9) to the data with all other parameter held constant. This value is in agreement with calculations of the scattering force magnitude on a Rayleigh particle using equation 1 in the work done by Ashkin et.al. [44] which yields $1.17pN$. For that calculation we assume the parameters of a $500nm$ diameter polystyrene particle with refractive index n_p trapped in water by a $1064nm$ vacuum wavelength laser. The intensity of the incident beam at $x = y = 0$, I_0, can be calculated from the total power and the x and y widths of the 2D-Gaussian beam profile by $I_0 = P/(\sigma_x\sigma_y\pi) = 70mW/(15\mu m \times 0.5\mu m \times \pi) = 3.0mW/\mu m^2$.

they emerge they must intersect in the focal plane. Thus it is expected that the intensity distribution in the trapping region near the reflective surface, which is situated near the front focal plane of the objective, must remain unchanged. Images of the intensity distribution on the surface of the dichroic coverslip were obtained by removing the band pass filter (see figure 2.1) from the observation path to allow the laser light to be imaged on the CCD chip. Figure 3.3(a) shows the intensity profiles along the x-axis as the cylinder lens is moved in steps of $50\mu m$.

A shift of $\pm 4\mu m$ in the center position of the intensity profiles can be seen as the cylinder lens is moved. This shift is a result of translating

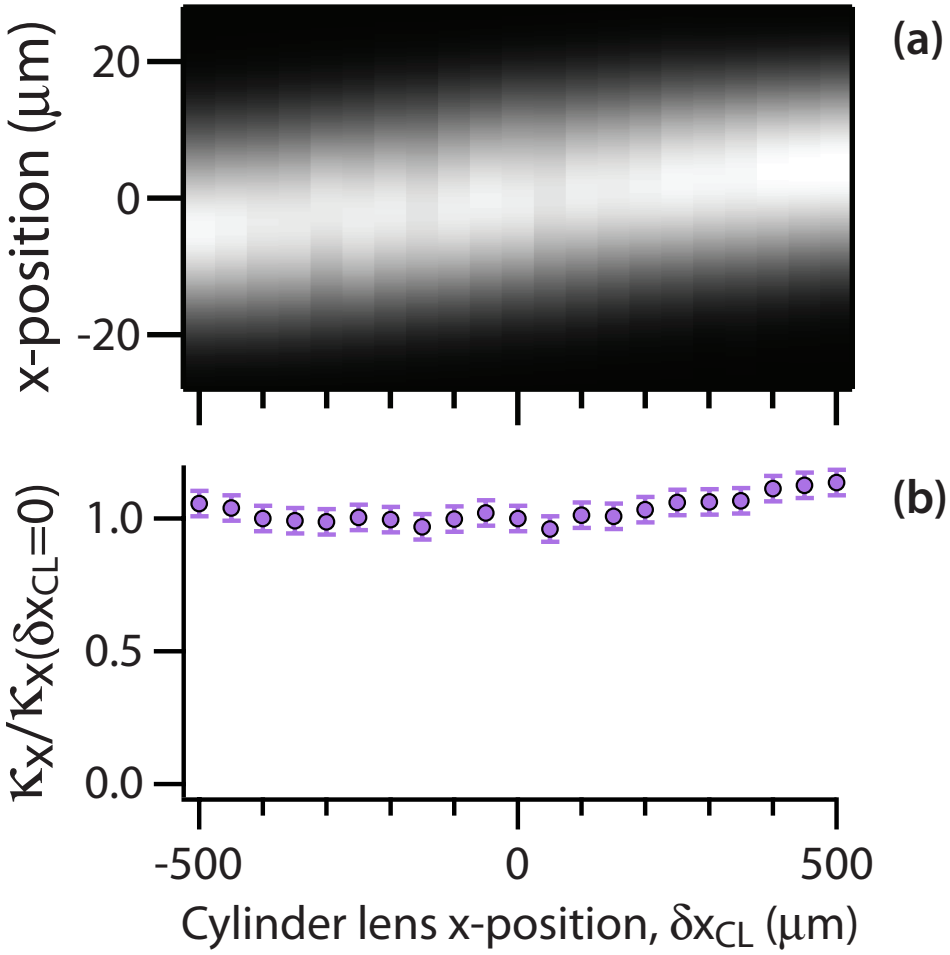

Figure 3.3: Intensity profile of the SWOLT as a function of the position of the cylinder lens. a) The intensity profile of the trap is imaged directly to provide the gradient force component of the optical forces acting on the particles. No particles are in the trap. Each column of pixels represents the intensity profile of the trap along its length averaged over $\pm 250nm$ from the longitudinal axis ($y = 0$). Profiles were measured as the cylinder lens was translated in steps of $50\mu m$. b) Normalized longitudinal stiffness ($\kappa_x/\kappa_{x(\delta x_{CL}=0)}$) of the SWOLT as function of the cylinder lens position. The stiffness was calculated from the intensity distribution (see text). Figure adapted from my publication [175].

the cylinder lens without also translating the path of the incident laser beam. However, this shift is in the opposite direction of the particle displacement and is smaller in magnitude. Therefore the scattering force is pushing the particle to different locations in the trap rather than being moved to a new intensity maximum by the gradient force.

To obtain a measure of the strength of the spring constant κ_x, we analyzed the intensity profiles. By taking the derivative of each intensity profile, which is proportional to the gradient force, a line can be fitted to the derivative near the trap's center. The slope of this line is proportional to the spring constant. Figure 3.3(b) shows that the calculated magnitude of the spring constant remains unchanged as the cylinder lens position is varied. Thus the strength of the lateral scattering and the gradient force are independent within the tested range.

3.2 Mathematical Determination of Particle Position

To describe the new equilibrium position of the trapped particle when the angle of incidence (θ_m) is not zero, we now develop a quantitative description of the lateral scattering force as a function of θ_m. The net scattering force can be described by:

$$\vec{F}^s_{net} = -2|\vec{F}^s_0| \sin(\theta_m)\hat{x} \tag{3.1}$$

where θ_m is the incident angle of the beam with respect to the normal of the reflective coverslip (see figure 2.1 and figure 3.4). $\vec{F}^s_0$ is the scattering force applied to the particle by the incident light ray. Assuming the particle

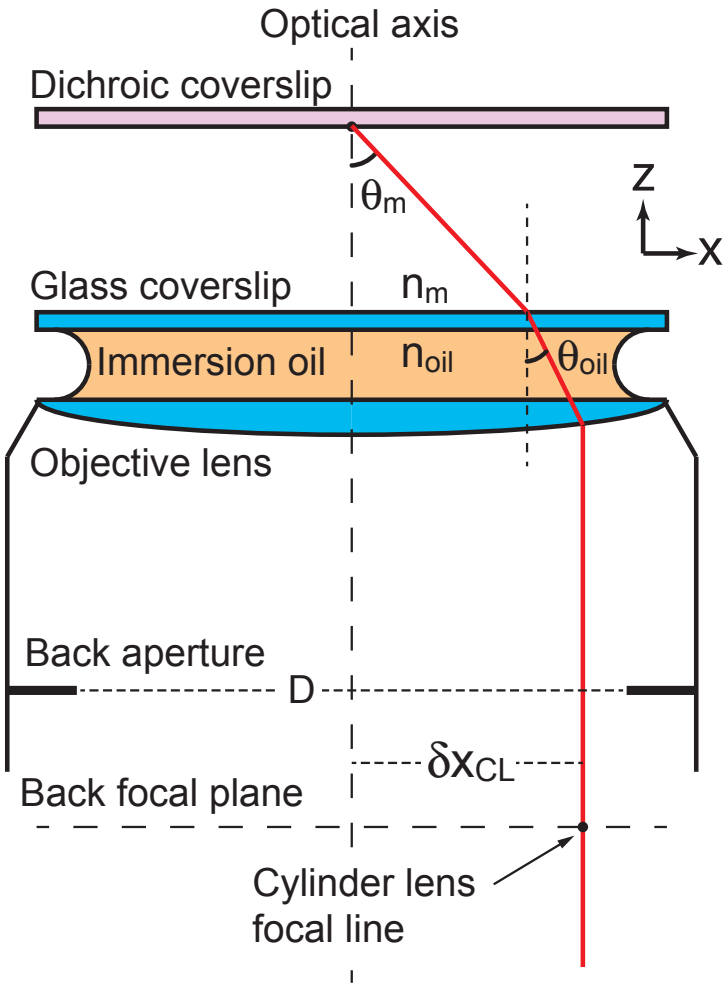

Figure 3.4: Definition of the parameters used to calculate the incident angle of the laser light θ_m as a function of cylinder lens position δx_{CL}. Figure from my publication [175].

is near the dichroic coverslip which has a reflectivity close to 100%, we can approximate the magnitude of the scattering force applied by the reflected light ray $\vec{F}^s_{ref}$ to be equal to that of the incident light ray (see figure 3.1 inset). If the particle is not trapped in the first antinode of the SWOLT (closest to the coverslip), but is trapped in an antinode further from the surface, this approximation will become less accurate for large incident angles θ_m since the incident and reflected rays striking the particles will have different intensities based on the intensity profile of the trapping beam. The magnitude of the force $\vec{F}^s_0$ is proportional to the intensity of the light ray generating that force. Since we can assume that the intensity profile of the beam is a Gaussian and the incident angle is independent of x-position in the SWOLT, we can write $\vec{F}^s_0(x) = \vec{F}^s_{00}\exp(-x^2/\sigma_x^2)$ where σ_x is the width of the Gaussian intensity profile in $\hat{x}$ and $\vec{F}^s_{00}$ is the incident scattering force at $x = 0$. Thus equation (3.1) becomes:

$$\vec{F}^s_{net} = -2|\vec{F}^s_{00}|\sin(\theta_m)e^{\frac{-x^2}{\sigma_x^2}}\hat{x} \tag{3.2}$$

To derive the relationship between the angle of incidence and the cylinder lens position, we use a simplified model of the objective lens as described by Hwang and Lee [194]. We consider a ray parallel to the optical axis whose distance from the optical axis corresponds to the center position δx_{CL} of the cylinder lens. The angle θ_{oil} can be related to the ray position δx_{CL} by:

$$n_{oil}\sin\theta_{oil} = \frac{\delta x_{CL}}{f} \tag{3.3}$$

where f is the focal length of the objective lens and n_{oil} is the refractive index of the immersion oil which is matched to that of glass. And in the limit where

$\delta x_{CL} = D/2$ the equation becomes:

$$n_{oil} \sin \theta_{oil}^{max} = \frac{D}{2f} \tag{3.4}$$

where θ_{oil}^{max} is the maximum incident angle and is related to the numerical aperture NA of the objective lens by:

$$n_{oil} \sin \theta_{oil}^{max} = NA \tag{3.5}$$

Using Snell's law, $n_m \sin \theta_m = n_{oil} \sin \theta_{oil}$, with Eqs. (3.3) , (3.4), and (3.5), we can write the incident angle θ_m as a function of the cylinder lens position δx_{CL}:

$$\sin \theta_m = \frac{2 \ NA \ \delta x_{CL}}{D \ n_m} \tag{3.6}$$

Thus the form of the scattering force and the gradient force acting on a particle along the x-axis in the SWOLT can be written as:

$$\vec{F}_{net}^{s}(x, \delta x_{CL}) = \frac{-4 \, |\vec{F}_{00}^{s}| \, NA \, \delta x_{CL}}{D \, n_m} \, e^{\frac{-x^2}{\sigma_x^2}} \, \hat{x} \tag{3.7}$$

$$\vec{F}_{x}^{g}(x) = -\kappa_x \, x \, e^{\frac{-x^2}{\sigma_x^2}} \, \hat{x} \tag{3.8}$$

where the x-component of the gradient force $\vec{F}_x^g$ is given by the gradient of a Gaussian intensity profile and is independent of cylinder lens position δx_{CL}. Using equation (3.7) and equation (3.8) it is now possible to solve for the equilibrium position of the particle, which is where $\vec{F}_{net}^{s} + \vec{F}_x^g = 0$. Solving these equations for x, the position of the particle, yields:

$$\vec{x}_{eqi}(\delta x_{CL}) = \frac{-4 \, |\vec{F}_{00}^{s}| \, NA \, \delta x_{CL}}{\kappa_x \, D \, n_m} \, \hat{x} \tag{3.9}$$

The validity of equation (3.9) can be tested by fitting this function against the experimental data (see figure 3.2) leaving the magnitude of the maximal scattering force ($|\vec{F}^s_{00}|$) as the only free parameter. The excellent agreement of data and calculation confirms that our simple model is sufficiently precise to describe the change of the scattering and gradient force as a function of the position of the cylinder lens correctly.

3.3 Measurement of Total Optical Force at All Positions

If the gradient force does not change as the angle of incidence is changed, then a probe particle can be manipulated by the scattering force alone to an arbitrary equilibrium position along the trap. This allows us to measure the transverse stiffness of the trap κ_y from the local thermal fluctuations of the particle (see figure 3.5). As expected, the transverse force constant, dominated by the gradient force, follows essentially the Gaussian intensity profile of the trap. When the particle is displaced $15\mu m$ from the center to either side, its transverse stiffness drops to just a few percent of its center value, but the trap is still strong. We like to emphasize again that the positioning of the particle was achieved by the lateral scattering force, in contrast to most other optical manipulation techniques in which the particle is transported primarily by the gradient force and thus typically comes to rest at the intensity maximum.

To quantify the lateral scattering force along the long axis of the trap, we track the probe particle as it is transported along the length of the trap to its rest position which is given by the balance of the gradient and scattering

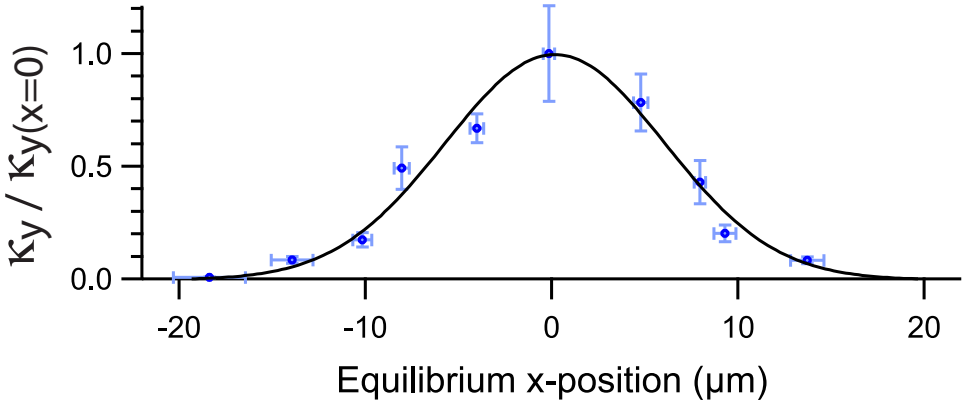

Figure 3.5: Transverse stiffness of the SWOLT measured at different equilibrium positions along the trap length. Using the lateral scattering force as shown in figure 3.1, a $500nm$ diameter polystyrene particle was pushed to positions away from the position of highest intensity. The transverse stiffness κ_y was measured concurrently with equilibrium position data shown in figure 3.2. A Gaussian profile is drawn to guide the eye. Figure from my publication [175].

force as calculated above. Since the Reynolds number of a nanoparticle in water is very small, it can be assumed that the particle/fluid system is overdamped and the particles travel at terminal velocity at any instant. In this case the drag and the optical force are always in balance, and we can determine the magnitude of the optical forces along the SWOLT from the local velocity of the particle using Stokes' law:

$$\vec{F}_x^d = 6\pi\epsilon\eta a v_x \hat{x} = \vec{F}_{net}^s + \vec{F}_x^g \tag{3.10}$$

where η is the viscosity of the fluid, ϵ is a correction factor for the viscous drag near a surface [195], a is the radius of the particle, and v_x is the x-component of the particle's velocity. Figure 3.6(b) shows the local velocities of particles and

$\lvert\vec{F}^s_{00}\rvert = 1pN$	$a = 250nm$	$\kappa_x = 25\frac{fN}{\mu m}$
$\sigma_x = 15.5\mu m$	$\eta = 1.0\frac{fNs}{\mu m^2}$	$\epsilon = 3$

Table 3.2: Parameters used to fit equation (3.11) to the velocity data shown in figure 3.6b. The value θ_m is the only free parameter used in the fit while the remaining parameters are fixed to known, measured, or estimated values. $|\vec{F}^s_{00}| = 1pN$ and $\kappa_x = 25fN/\mu m$ are set to experimentally determined values as described for figure 3.2 (see also table 3.1). The particle radius ($a = 250nm$) is given by the manufacturer; the width of the Gaussian intensity profile ($\sigma_x = 15.5\mu m$) is measured from images of the intensity profile at the coverslip surface; the viscosity of water ($\eta = 1.0fNs/\mu m^2$) is known; and the viscous drag correction factor ($\epsilon = 3$) was estimated for a particle moving near a surface [195].

the corresponding forces while they are transported form the capture position to the position of zero force. The results are an average over 16 to 18 particles for each of the three angles of incidence. Though the particles used here are large and are trapped near the surface, they do not make contact due to repulsive electrostatic forces. This occurs because both the glass surface and the carboxylated polystyrene particles naturally have a negative charge, and the Debye length in deionized water is very long compared to the glass-particle separation distance.

For the case of vertical incidence ($\theta_m \approx 0$) for which the scattering force is almost completely compensated, the force profile resembles that of the gradient of a Gaussian intensity profile as expected. When the incidence angle is not zero, a net scattering force ($\vec{F}^s_{net}$) is generated. With increasing angle of incidence, the maximum velocity of the captured particle increases, and the

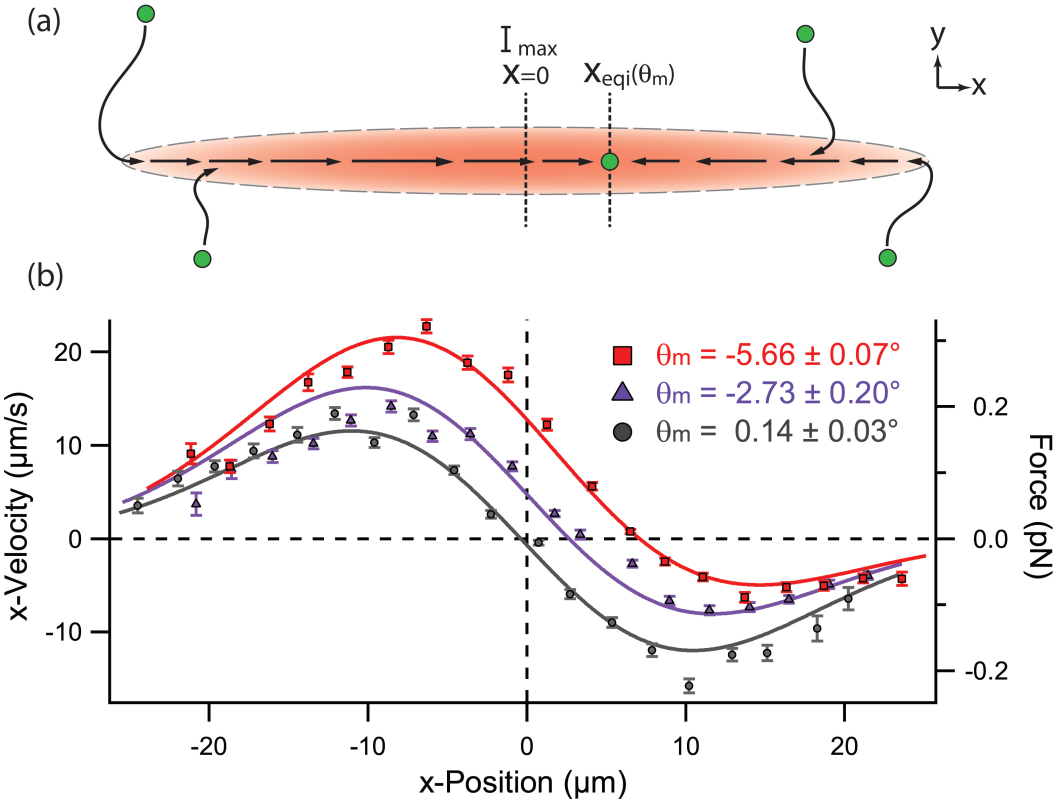

Figure 3.6: Measurement of the optical force component along the long axis of the SWOLT: $\vec{F}_x^{Total}(x) = \vec{F}_{net}^{s}(x) + \vec{F}_x^{g}(x)$. To measure the forces acting along the entire length of the trap, particle velocities were measured. a) Experimental procedure. Particles diffuse one-by-one into the trap near one of the ends. A video is recorded of the particle being transported to its rest position which depends on the incident angle of the trapping beam θ_m. The positions and velocities of the particles are determined by video particle tracking. b) The average velocity of the particle at each position in the trap is shown for different angles of incidence (θ_m). The right axis shows the corresponding optical forces. The solid curves are fits from the model (equation (3.11)) where θ_m is the only free parameter. The remaining parameters are fixed to known, measured, or estimated values and are given in table 3.2. Videos were recorded at a rate of 80 fps. The results of at least 16 particles were averaged for each measurement. The error bars represent the standard error of the mean of these measurements. All measurements were done using $70mW$ of laser power in the sample plane. Figure from my publication [175].

equilibrium position of the particle is moved further away from the center of the trap as already indicated in figure 3.2. We can calculate the local velocity of the particle as a function of the angle of incidence from equations (3.2), (3.8), and Stokes' law (3.10):

$$\vec{v}_x(x,\theta_m) = \frac{-1}{6\pi\epsilon\eta a} e^{\frac{-x^2}{\sigma_x^2}} \left[2|\vec{F}_{00}^s| \sin(\theta_m) + \kappa_x x\right]\hat{x} \tag{3.11}$$

The data sets in figure 3.6(b) were fitted with equation (3.11) where the angle of incidence was the only free parameter. The resulting angles of incidence agree well with the experimental values calculated from the cylinder lens positions $\delta x_{CL} = \{0\mu m, -100\mu m, -200\mu m\} \pm 15\mu m$ (corresponding to $\theta_m = \{0°, -2.62°, -5.24°\} \pm 0.39°$). The uncertainty in cylinder lens position arises from the mechanical accuracy and drifting of the positioning stage. The good agreement between the model and data again supports the assumption that the scattering force can be varied independently of the gradient force.

3.4 Summary

A method for generating single-direction transport of particles within the SWOLT was presented and tested. By translating the cylinder lens perpendicular to the optical axis, the incident angle of the trapping beam can be changed. This in turn generates lateral scattering force components which can push particles to new positions along the length of the SWOLT. This mechanism was described in detail, and a mathematical model based on ray optics was developed. The positioning of particles along the length of the SWOLT

was demonstrated, and the results were compared successfully with the model predictions. The transport velocities of particles in the SWOLT were measured in order to determine the total optical force as a function of position in the SWOLT. These measurements were also shown to agree with model predictions. Finally, it was shown that the scattering force which is used to transport the particles can be varied without disturbing the intensity distribution of the trapping volume, thereby maintaining a static gradient force field.

Chapter 4

Bi-Directional Manipulation in the SWOLT

4.1 Generating Axially Symmetric Scattering Force Components

So far, net scattering forces were generated by changing the angle of incidence of the collimated beam by displacing the cylinder lens perpendicular to the optical axis. However, scattering forces that lead to transport in the SWOLT can be generated in another way. Figure 4.1 illustrates how lateral scattering forces can be generated by translating the cylinder lens along the optical axis rather than perpendicular to it.

The forces now act radially inwards (converging beam) or outwards (diverging beam) from the optical axis, and the incident angle varies with the position along the long axis of the trap. For a diverging beam (figure 4.1(a)), the x-components of the scattering force counteract the gradient force and push the particles away from the center of the trap. For a converging beam (figure 4.1(b)), the net scattering force reinforces the gradient force and pushes the particles toward the center of the trap. The latter essentially leads to stronger confinement and a higher force constant of the trap. Also in this case, the intensity profile of the SWOLT near the surface of the dichroic coverslip will remain constant as the cylinder lens is translated along the optical axis (δz_{CL}).

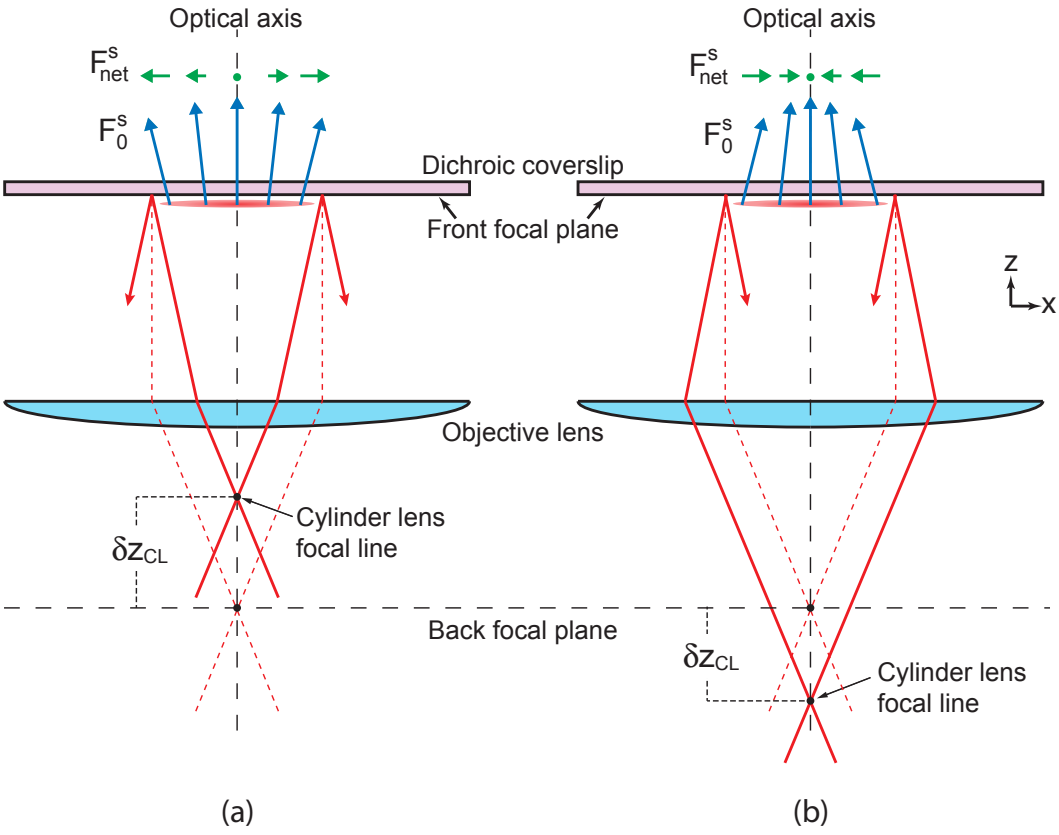

Figure 4.1: Generation of axially symmetric scattering forces by translating the cylinder lens along the optical axis. a) Generation of radially outward pointing scattering forces by a diverging beam. b) Generation of radially inward pointing scattering forces by a converging beam. The blue arrows represent the incident scattering force vector at different locations along the SWOLT. The green arrows represent the net scattering force vectors when considering the contribution of the reflection off the dichroic coverslip. The resultant net force is parallel to the plane of the coverslip since the z-components cancel. Figure from my publication [175].

Thus the gradient force again remains constant even as the scattering force is varied. Using this technique, particles can be transported radially toward or away from the center of the SWOLT, rather than unidirectionally as shown earlier. Figure 4.2 shows images of particles being positioned by translating the cylinder lens along the optical axis.

When the cylinder lens is moved towards the objective lens and a diverging beam is generated, the net scattering force acts radially outward and pushes the particles outward from the center of the trap, thus separating them as shown in figure 4.2(a). When the cylinder lens is moved away from the objective lens and a converging beam is generated, the particles are pressed together as shown in figure 4.2(c). We note that the inter-particle spacings seen in figure 4.2 are determined in part by optical binding forces [115, 116, 118, 196–198]. The SWOLT in fact provides a very efficient method for studying this "third" optical force, and the results of this study are presented in Part II of this dissertation (starting page 93).

4.2 Ray Optics Theory of Axially Symmetric Scattering Forces

Similarly to the case of the lateral transport (chapter 3), a mathematical model based on ray optics can be used to predict the magnitude of the scattering force at any location along the SWOLT length. However, this model is a bit more complex since the angle at which the rays strike the reflecting surface vary as a function of position along the SWOLT. Nevertheless, we be-

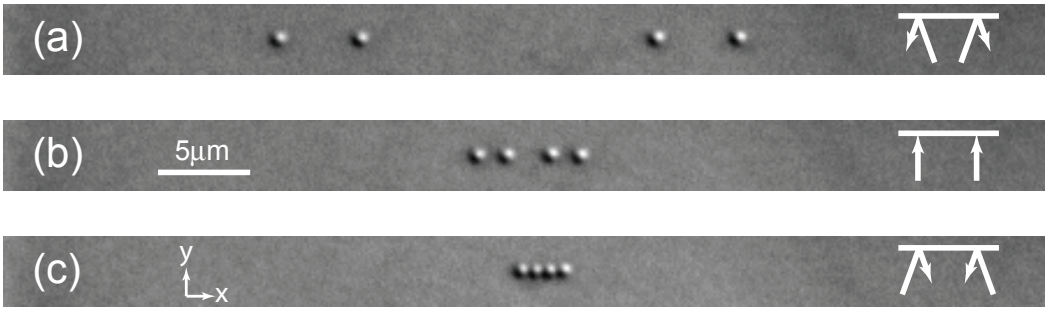

Figure 4.2: Positioning of particles with radially symmetric scattering forces. a) Particles are pushed away from the center of the trap by the lateral scattering forces generated by a diverging beam ($\delta z_{CL} = 60mm$). b) Particles move closer to the center of SWOLT when the laser light is focused on the back focal plane of the objective lens ($\delta z_{CL} = 0$) and the net scattering force is reduced to 0. c) When the cylinder lens is moved away from the objective lens ($\delta z_{CL} = -140mm$) thus generating a converging beam, the particles are pressed closer together. Inset: Propagation of the light rays at the dichroic coverslip surface. Figure from my publication [175].

gin by using the ray optics model detailed in figure 4.3. If we consider the cylinder lens focal line to be a point source, we know that the position of that point source along the optical axis (the object plane) is related to the location of the image (image plane). We can determine the location of the image plane by analyzing the geometry of figure 4.3. We use a "test" object in order to construct the geometry, as just using a point source on the optical axis is not sufficient. Since our system includes a refractive index mismatch interface between the glass and water, we need to consider both the image first generated by the lens/glass/oil system alone as well as the image generated including this interface. This is necessary for complete determination of the paths and angles of the light rays.

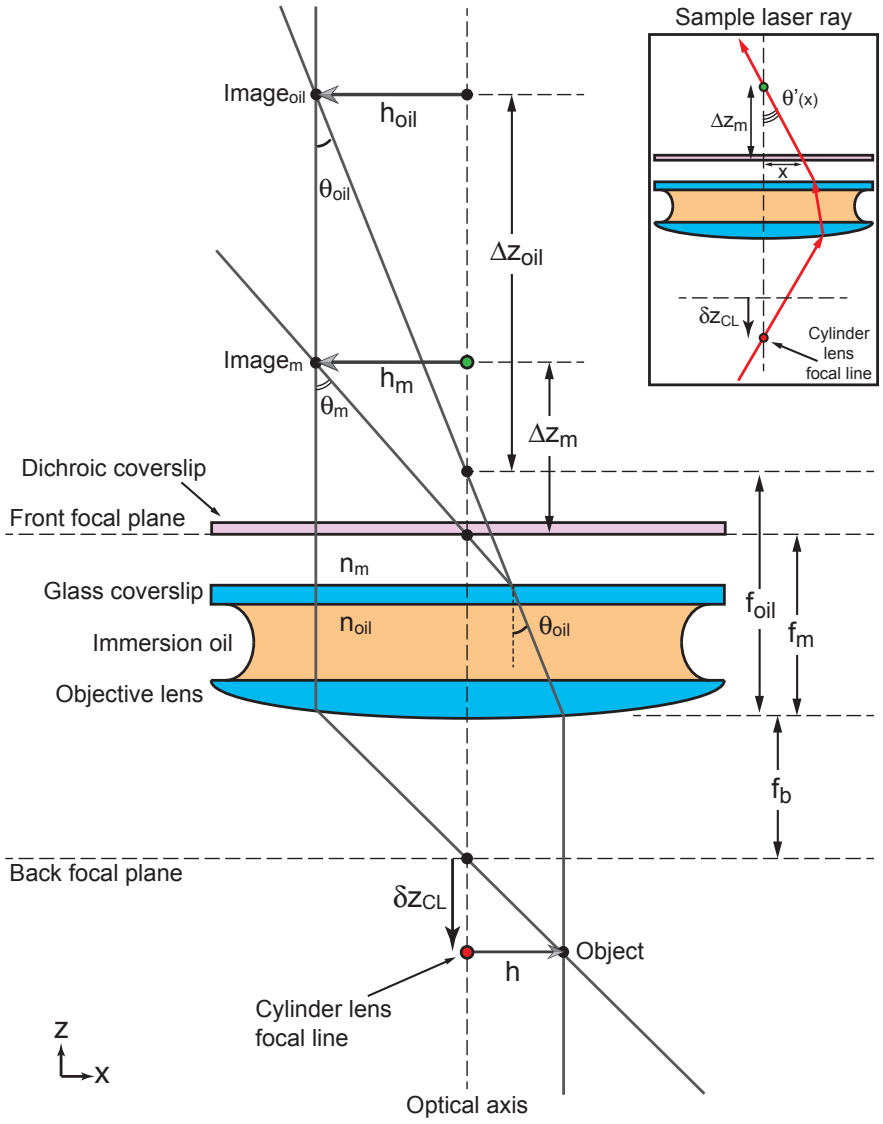

Figure 4.3: Definition of the parameters used to calculate the incident angle of the laser light as a function of cylinder lens position axial displacement δz_{CL}. I use a "test" object (with its corresponding image) to aid in construction of the ray optics geometry and determine the location of the final imaging plane (Image_m). The inset shows the path of a sample ray from the trapping laser which is focused on the optical axis but displaced a distance δz_{CL} from the back focal plane. The angle with which the ray strikes the surface $\theta'(x)$ is dependent on the distance along the surface x.

Now we can begin to relate the variables geometrically. First it is obvious that $h_{oil} = h_m$. Next, by noting the similar triangles, we can also clearly see the relations:

$$\frac{\delta z_{CL}}{h} = \frac{f_b}{h_m} \tag{4.1}$$

$$\frac{\Delta z_{oil}}{h_m} = \frac{f_{oil}}{h} \tag{4.2}$$

where δz_{CL} is the displacement of the cylinder lens focal line from the back focal plane of the objective lens along the optical axis, and f_b is the back focal length of the objective lens (the other values are constructs from the "test" geometry). Combining equations (4.1) and (4.2) we find:

$$\delta z_{CL} \Delta z_{oil} = f_b f_{oil} \tag{4.3}$$

Next, we can see a relationship between Δz_{oil} and Δz_m using the common side h_m. First we note:

$$\tan\theta_{oil} = \frac{h_m}{\Delta z_{oil}} \tag{4.4}$$

$$\tan\theta_m = \frac{h_m}{\Delta z_m} \tag{4.5}$$

The combination of equations (4.4) and (4.5) yields:

$$\Delta z_{oil} = \left[\frac{\tan\theta_m}{\tan\theta_{oil}}\right] \Delta z_m \tag{4.6}$$

The next step is to assume that the object height h is equal to half the diameter of the back aperture such that the angles θ_{oil} and θ_m take on their maximum values for light rays passing through this objective lens (see also figure 3.4).

This is a valid choice since the location of the image plane does not depend on the height of the object, and this allows us to relate the maximum angle (θ_{oil}^{max}) to the diameter of the front aperture (D_f) and the numerical aperture (NA) of the objective lens by the relation given in reference [194] (this relation was also used in chapter 3.2):

$$\sin\theta_{oil}^{max} = \frac{D_f}{2f_{oil}} \tag{4.7}$$

as well as the known definition of the numerical aperture NA:

$$NA = n_{oil}\sin\theta_{oil}^{max} \tag{4.8}$$

Therefore, when we let $h_m \to D_f/2$ such that $\theta_{oil} \to \theta_{oil}^{max}$ and $\theta_m \to \theta_m^{max}$, we can use equations (4.7) and (4.8) to rewrite equation (4.6) as:

$$\Delta z_{oil} = \left[\frac{\tan\theta_m^{max}}{\tan\theta_{oil}^{max}}\right]\Delta z_m \tag{4.9}$$

$$= \left[\frac{\tan\theta_m^{max}}{\tan(\sin^{-1}(\frac{D_f}{2f_{oil}}))}\right]\Delta z_m \tag{4.10}$$

$$= \left[\left(\frac{2f_{oil}}{D_f}\right)^2 - 1\right]^{\frac{1}{2}}\tan\theta_m^{max}\Delta z_m \tag{4.11}$$

Now we can use Snell's law to relate the incident and refracted angles at the glass/water interface ($n_{oil}\sin\theta_{oil} = n_m\sin\theta_m$). Substituting this into equation (4.11) we get:

$$\Delta z_{oil} = \left[\left(\frac{2f_{oil}}{D_f}\right)^2 - 1\right]^{\frac{1}{2}}\tan\left(\sin^{-1}\left(\frac{n_{oil}}{n_m}\sin\theta_{oil}^{max}\right)\right)\Delta z_m \tag{4.12}$$

Again, using equation (4.7) we rewrite equation (4.12):

$$\Delta z_{oil} = \left[\left(\frac{2f_{oil}}{D_f}\right)^2 - 1\right]^{\frac{1}{2}} \tan\left(\sin^{-1}\left(\frac{NA}{n_m}\right)\right) \Delta z_m \tag{4.13}$$

$$= \sqrt{\left[\left(\frac{2f_{oil}}{D_f}\right)^2 - 1\right] \Big/ \left[\left(\frac{n_m}{NA}\right)^2 - 1\right]} \Delta z_m \tag{4.14}$$

Solving equation (4.14) for the displacement of the image plane:

$$\Delta z_m = \sqrt{\left[\left(\frac{n_m}{NA}\right)^2 - 1\right] \Big/ \left[\left(\frac{2f_{oil}}{D_f}\right)^2 - 1\right]} \Delta z_{oil} \tag{4.15}$$

Now we consider the inset in figure 4.3 and relate the incident angle of the light ray (θ') to the displacement of the image plane (Δz_m) and the lateral displacement along the reflective surface (x):

$$\tan\theta' = \frac{x}{\Delta z_m} \tag{4.16}$$

Since we know that we are only interested in the x-component of the scattering force, we can make the remaining steps simpler by calculating $\sin\theta'$:

$$\sin\theta' = \sin\left(\tan^{-1}\left(\frac{x}{\Delta z_m}\right)\right) \tag{4.17}$$

$$= \left[\left(\frac{\Delta z_m}{x}\right)^2 + 1\right]^{-\frac{1}{2}} \tag{4.18}$$

$$= \left[\left(\frac{\left[\frac{n_m}{NA}\right]^2 - 1}{\left[\frac{2f_{oil}}{D_f}\right]^2 - 1}\right)\left(\frac{\Delta z_{oil}}{x}\right)^2 + 1\right]^{-\frac{1}{2}} \tag{4.19}$$

Now we substitute equation (4.3) into equation (4.19) to get:

$$\sin\theta' = \left[\left(\frac{\left[\frac{n_m}{NA}\right]^2 - 1}{\left[\frac{2f_{oil}}{D_f}\right]^2 - 1}\right)\left(\frac{f_b f_{oil}}{x\delta z_{CL}}\right)^2 + 1\right]^{-\frac{1}{2}} \tag{4.20}$$

$$= \left[\left(\frac{\left[\frac{n_m}{NA}\right]^2 - 1}{\left[\frac{2}{D_f}\right]^2 - \left[\frac{1}{f_{oil}}\right]^2}\right)\left(\frac{f_b}{x\delta z_{CL}}\right)^2 + 1\right]^{-\frac{1}{2}} \tag{4.21}$$

Finally, we use equations (4.7) and (4.8) to relate for f_{oil} to known parameters:

$$f_{oil} = \frac{D_f\, n_{oil}}{2\, NA} \tag{4.22}$$

Substituting equation (4.22) into equation (4.21) we can now solve for the angle θ' with respect to known physical parameters:

$$\sin\theta'(x) = \left[\left(\frac{\left[\frac{n_m}{NA}\right]^2 - 1}{1 - \left[\frac{NA}{n_{oil}}\right]^2}\right)\left(\frac{f_b D_f}{2\, x\, \delta z_{CL}}\right)^2 + 1\right]^{-\frac{1}{2}} \tag{4.23}$$

Now we can use equation (4.23) in conjunction with the description of the scattering force given by equation (3.1). From equation (4.23) we can clearly see that when $\delta z_{CL} \to 0$ the angle θ' is 0 (no lateral component of scattering force) at all positions x along the length of the SWOLT as we would expect. For a finite valule of δz_{CL}, we see that for $x = 0$ the angle is always $\theta' = 0$, as expected for the axially symmetric system. For lager displacements of a particle from the optical axis, x, the incident angle becomes increasingly steep. Again, this is as we expect conceptually from figure 4.1.

4.3 Summary

A method for generating bi-directional transport of particles within the SWOLT was presented and tested. Here, the cylinder lens was translated along the optical axis in order to generate a converging or diverging beam within the sample chamber thereby generating inward or outward transport of particles respectively. This mechanism was described using ray optics, and a mathematical model describing the scattering force was derived. Separation and compression of multiple particles using this mechanism was demonstrated.

Chapter 5

Continuous Transport of Particles Using the SWOLT Within a Fluid Flow

5.1 Uni- & Bi-Directional Continuous Transport

Since both the methods, single-direction transport as in figure 3.1 and radial transport as in figure 4.1, allow for varying the net scattering force independently of the gradient force, they can be used to generate continuous transport of particles. Figure 5.1(a) shows the continuous transport of particles in a single direction by increasing the angle of incidence of a collimated beam while figure 5.1(b) shows the continuous transport of particles in opposite directions by a divergent beam.

Particles $500nm$ in diameter, carried by a flow of water, are captured by the SWOLT which lies perpendicular to the fluid flow. Since the cylinder lens has been translated perpendicular to or along the optical axis, a net scattering force is generated which pushes the particles toward the end(s) of the trap. Since the transverse spring constant κ_y of the trap decreases significantly toward the ends of the trap (see figure 3.5), the drag force on the particles is sufficient to overcome the optical gradient force there and carry the particles out of the trap. Thus continuous transport is generated in the SWOLT by

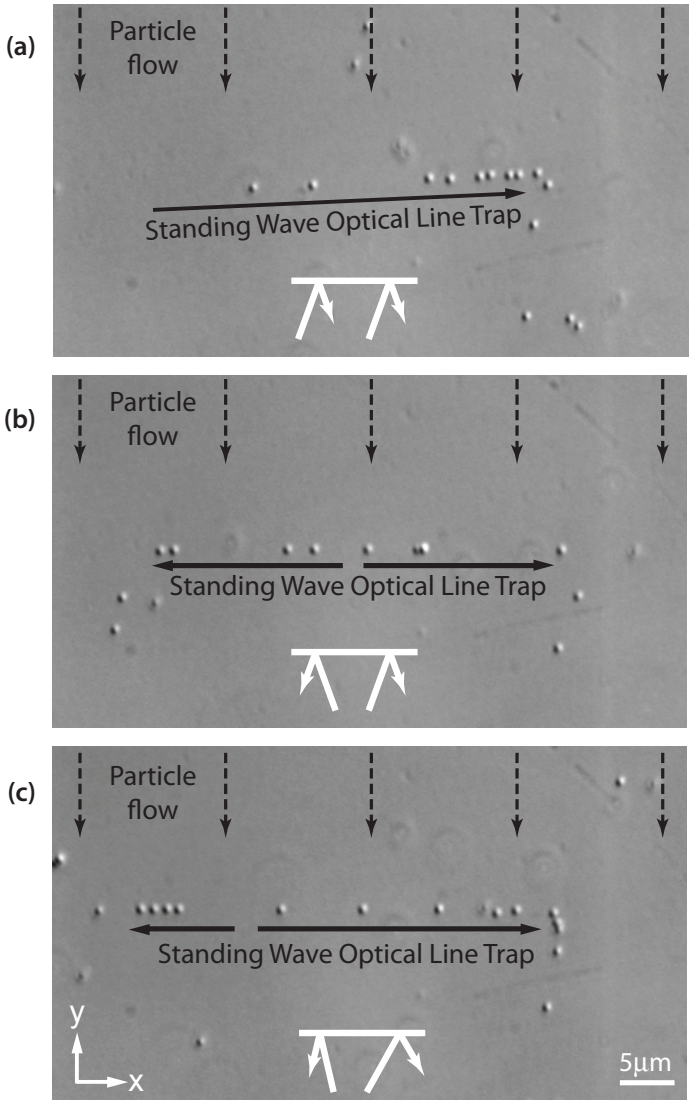

Figure 5.1: Particles are continuously transported by fluid flow into the SWOLT which lies perpendicular to the flow. The particles are then captured and transported towards the end(s) of the trap where they can then be pushed out by drag forces. a) Single direction transport as illustrated in figure 3.1 with $\delta x_{CL} = -500\mu m$. b) Bi-directional outward transport as illustrated in figure 4.1 with $\delta z_{CL} = 100mm$. c) Combination of both uni- and bi-directional transport methods with $(\delta x_{CL}, \delta z_{CL}) = (-300\mu m, 100mm)$. Inset: Propagation of the light rays at the dichroic coverslip surface. Figure adapted from my publication [175].

combination of the strong gradient force that captures the particles from the flow and the strong lateral scattering force that pushes the particles over long distance to unstable regions where they leave the SWOLT. We note that in figure 5.1a the SWOLT has been tilted slightly towards the fluid flow to show that the transport is not due to drag forces, but is in fact is an optical effect.

Figure 5.2, corresponding to figure 5.1a, shows example streamlines of particle flow into, carried by, and out of the SWOLT. By locating and tracking the positions of only the particles which are in the focal plane of any given frame, I can generate an image representing the flow pattern over the course of 250 frames of the corresponding video. Since only the particles in the focal plane are tracked, we can see not only information about their x and y positions, but also information about their z axis motion. Since the particles in the bulk fluid are free to thermally diffuse in all directions, they constantly come in and out of the focal plane. This is indicated in figure 5.2 by the many short streamlines above and below the SWOLT. When particles are captured from the fluid flow by the SWOLT, they are then confined to the 1D trapping volume which also lies in the focal plane. Therefore, along the SWOLT we see a solid streamline as the particles are transported to the right edge by the optical scattering force. When the particles near the end of the SWOLT, the are carried out by the fluid flow. Since the particles leaving the SWOLT all originate in the focal plane, the exiting streamlines are at first very dense, but become less dense as the particles diffuse again in all directions.

It is also possible to add the effects of both transport methods simulta-

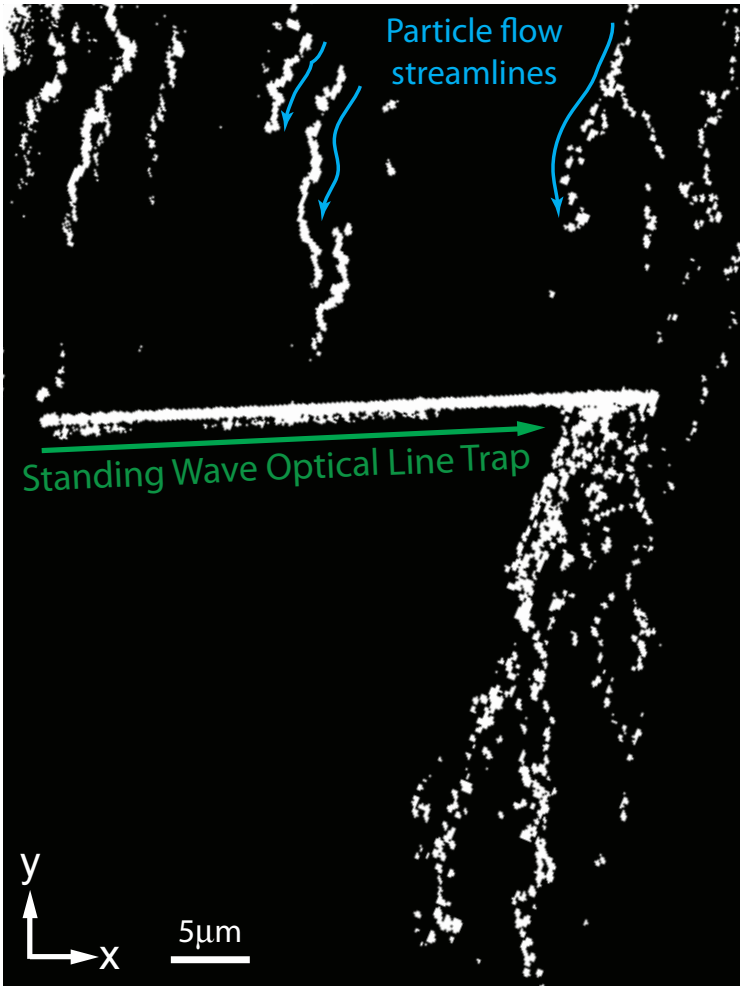

Figure 5.2: The video corresponding to figure 5.1a was analyzed to show the flow pattern (streamlines) of the 500nm diameter polystyrene particles into a SWOLT. Only particles in the focal plane were located in 250 consecutive frames of the video taken at 20fps and the set of all particle locations is plotted as white pixels. A few streamlines are highlighted by blue arrows as examples. We can see that particles diffuse easily in and out of focus while in the bulk fluid (many short streamlines), but in the SWOLT they are transported precisely in the focal plane. Particles leaving the SWOLT, carried out by the flow, begin their new journey within the focal plane and slowly diffuse again in all directions.

neously by providing both a lateral and axial translation of the cylinder lens. The result is that the particles are once again transported in opposite directions depending on their location in the trap, but the point at which the lateral scattering force changes direction is no longer in the center of the SWOLT. It is instead shifted such that the majority of the SWOLT transports particles in one direction while a smaller fraction of the SWOLT is responsible for transport in the opposite direction (see figure 5.1c). This is a simple example of how the SWOLT can be used to sort particles. Here, we can send a given fraction of the particles to one side, and the remaining fraction to the other side. In the future, more advanced sorting mechanisms can be designed which can sort based on size or refractive index of the particle (see chapter 7.1).

5.2 Summary

A method for continuous optical transport of particles using the SWOLT was presented. Particles could be captured from a fluid flow by the SWOLT then immediately transported to the ends of the SWOLT using the scattering forces. At the ends of the SWOLT, the confining gradient forces are weaker and so the particles can then be carried out of the SWOLT once they reach the ends. Continuous transport in a single direction using the method of chapter 3 and outward transport from the SWOLT center using the method of chapter 4 were demonstrated. Additionally, both methods can be combined resulting in a biased outward transport of particles such that a larger fraction of particles are transported toward one end than the other.

Chapter 6

The Pancake Trap

6.1 Introduction

While confinement of objects to one-dimension using the SWOLT is an efficient way to manipulate and study 1D systems or elongated objects, there are also many systems which are most effectively studied in two-dimensions. For example, optical fractionation techniques [135–137, 139, 144, 157] for passive sorting, mixing and analysis of particles works most efficiently when the particles can be manipulated in 2D or 3D. More recently, nanoparticles have been predicted to interact within optical fields to form clusters of well defined geometries [199], known as "optical matter." Elongated nano-objects, such as microtubules and actin filaments, may require freedom to rotate, fluctuate and arrange in 2D in order to display certain behavior, such as the formation of cytoskeletal networks. Many of these 2D systems are required to be free from surface contact in order for the nano-objects to freely diffuse and organize. However, until now a tool which can stably confine nanoparticles in a wide 2D plane away from surfaces has not been available.

Aside from pressing objects between two solid, flat surfaces, confinement in 2D is most commonly achieved through total internal reflection optical

trapping [101, 102, 200, 201] where the steep optical gradients of the evanescent field pull particles into direct contact with a single flat surface. Particle motion is greatly dampened from contact with the surface and thus particles cannot freely explore different arrangements through thermal motion. In addition, the steep incident angle of the laser beam generates a scattering force on the particles which transports them along the surface [101, 102] and eventually out of the field of view or until pressed against a barrier. Counter propagating beams can be used, but either an interference pattern is generated which puts the particles in a pre-defined configuration due to the intensity pattern, or if cross polarized beams are used, dynamics dependent on a well-defined polarization direction of the optical field can no longer be observed [201]. I solve these major problems of current 2D trapping methods through development of a new optical trapping instrument which I call the optical pancake trap (PT).

6.2 Instrument Design

The design of the pancake trap is very similar to the design of the SWOLT as described in chapter 2.2. A schematic of an optical pancake trap setup using dark field microscopy illumination is shown in figure 6.1. It is also possible to use DIC, as shown with the SWOLT setup, and that design would be much like it is shown in figure 2.1. The pancake trap, like the SWOLT, is based on a typical optical tweezer design [44, 100, 165, 174] built around a commercial microscope with two modifications. First, a plano-convex spherical lens (LA1172-C-ML, $f = 400mm$, Thor Labs, USA) is added to the optical

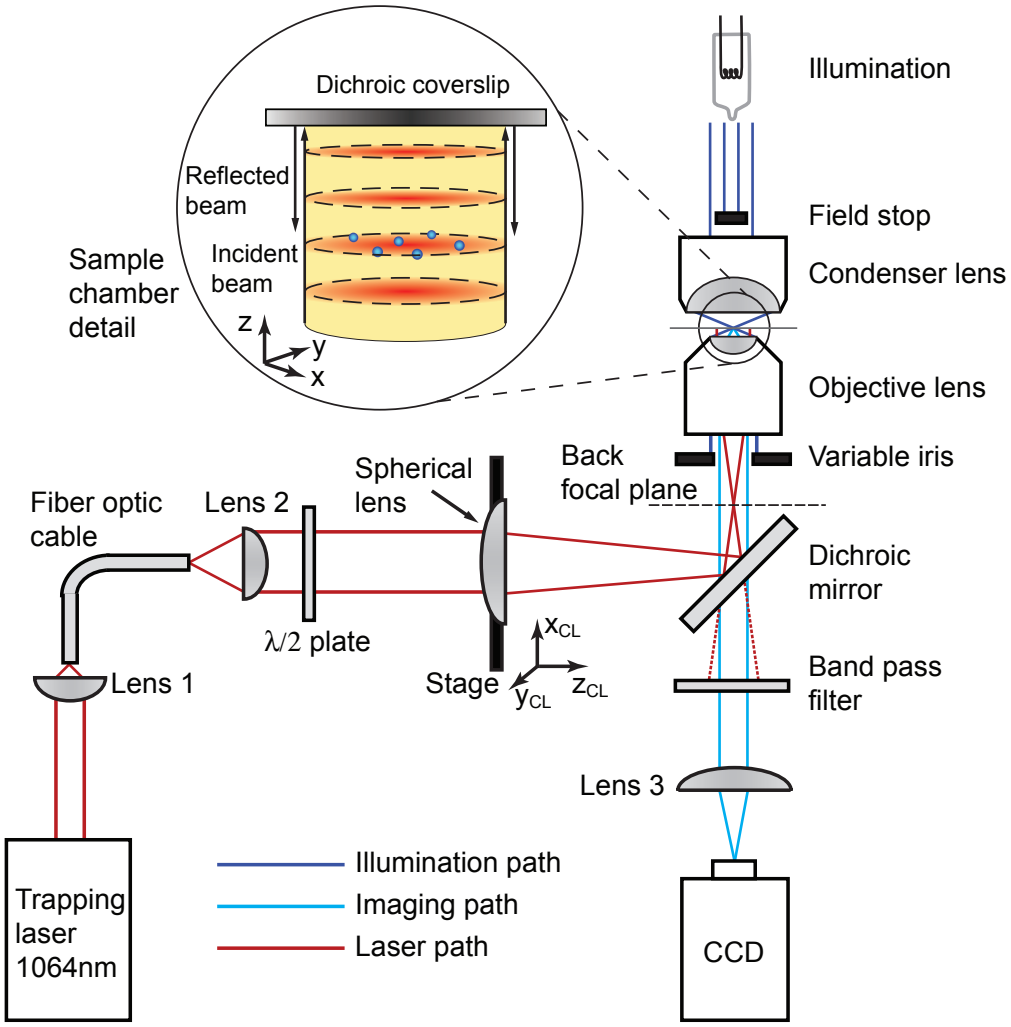

Figure 6.1: Schematic of an optical pancake trap. The design is based on a standard single beam trap design [75, 174], but with two additions. A dichroic coverslip is used as part of the sample chamber to generate a standing wave optical trap. The addition of a spherical lens in the trapping laser optical path is used to generate a collimated beam withing the sample chamber, rather than a point focused beam. Many different imagin techniques can also be used with the pancake trap, such as DIC microscopy. Figure 2.1 shows a similar setup using DIC imaging. See also figure 10.1 for a 3D illustration of the trapping volume.

path just behind the microscope objective lens (Plan-Neofluar 100x/1.3 Oil Iris, Carl Zeiss, Germany). By using this spherical lens to focus an incident laser beam (vacuum wavelength $\lambda_0 = 1064nm$) onto the back focal plane of the objective lens, a collimated beam is formed within the sample chamber. This is similar in concept to a simple beam expander design but in reverse a beam shrinker which reduces the diameter of the incident collimated laser beam by about three orders of magnitude. Within the sample chamber, the shrunk collimated beam is reflected off of a dichroic coverslip (reflectivity $> 99\%$) thereby generating a standing wave intensity distribution axially, while maintaining a wide 2D Gaussian intensity distribution radially (see figure 6.1). Thus, particles trapped by gradient forces in the high intensity regions (antinodes) experience strong axial confinement but weak radial confinement, effectively restricting motion to a wide 2D plane. These stacked, wide 2D trapping regions are nearly identical in size and strength, and therefore we observe nearly identical behavior of trapped particles in planes up to about $50\mu m$ from the reflective surface. This enables 2D trapping far from surfaces which may affect the dynamics which one intends to observe.

6.3 Single Particle Characterization of Trap Size

We can characterize the trapping potential of the pancake trap by monitoring a particle diffusing in the trap for long timescales. This is an identical technique as described in chapter 2.4. Figure 6.2 shows a position histogram of a single $200nm$ diameter gold particle trapped in the pancake trap.

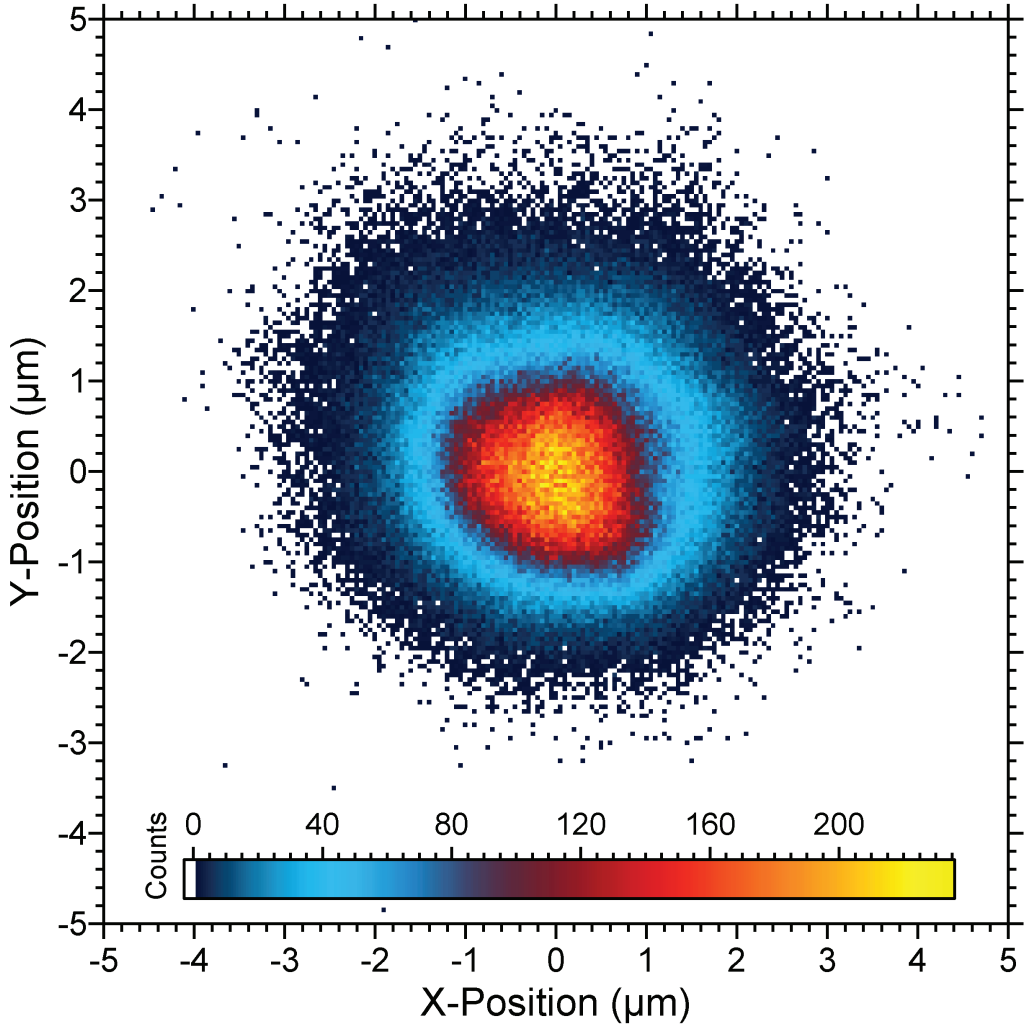

Figure 6.2: Position histogram of a single $200nm$ diameter gold particle in the pancake trap using $130mW$ of laser power measured in the sample plane. The histogram is generated from 3.7×10^5 data points (2 hours of video at $50fps$ using dark-field microscopy). The wide, Gaussian trapping area is demonstrated. While the diameter of the region explored by the particle can be seen to be relatively small ($2\sigma_p = 1.66\mu m$), this due to the strong polarizability of the gold particle. The actual diameter of the beam can be calculated from knowledge of the particle polarizability and sample temperature to be $2\sigma_I \approx 12.6\mu m$ (see chapter 6.3). Bin size= $50nm \times 50nm$.

The histogram illustrates the wide, Gaussian, axially-symmetric trapping volume of the pancake trap. The width of this Gaussian probability distribution shown is $\sigma_p = 0.83\mu m$ and this value is directly related to the Gaussian intensity profile of the beam. Since the confinement of a particle within an optical field is dependent on the intensity of the field as well as the parameters of the particle which determine its polarizability (such as its size and refractive index), the true width of the collimated beam used to generate the pancake trap may be calculated knowing these parameters.

Through Boltzmann statistics we can relate the probability of finding the particle in a given location to the potential energy of being in that location:

$$W_{x,y} = \frac{1}{Z} e^{\frac{-U_{x,y}}{k_B T}} \tag{6.1}$$

where $W_{x,y}$ is the probability of being at location (x, y) , $U_{x,y}$ is the potential energy of the particle at that location, $k_B T$ is the thermal energy of a single particle, and $Z = \int\int_{-\infty}^{\infty} e^{\frac{-U_{x,y}}{k_B T}} \mathrm{d}x\mathrm{d}y$ is a normalizing factor ensuring the total probability over all space is equal to 1. It is reasonable to approximate the measured probability distribution as a 2D Gaussian, and thus we can rewrite equation (6.1) as:

$$\frac{1}{A} e^{\frac{-\left(x^2+y^2\right)}{\sigma_p^2}} = \frac{1}{Z} e^{\frac{-U_{x,y}}{k_B T}} \tag{6.2}$$

where σ_p is the width of the 2D Gaussian probability distribution and $A = \int\int_{-\infty}^{\infty} e^{\frac{-\left(x^2+y^2\right)}{\sigma_p^2}} \mathrm{d}x\mathrm{d}y = \sigma_p^2 \pi$ is a normalizing factor ensuring the total probability over all space is again equal to 1. We also know that the only significant

potential in our system is due to the gradient force on the single particle, and this potential is given by:

$$U_{x,y}^{grad} = -\frac{\alpha}{2}E_{x,y}^2 \tag{6.3}$$

$$= -\frac{\alpha}{cn_m\epsilon_0}I_{x,y} \tag{6.4}$$

$$= -\frac{\alpha}{cn_m\epsilon_0}I_0 e^{\frac{-\left(x^2+y^2\right)}{\sigma_I^2}} \tag{6.5}$$

$$= -\frac{\alpha}{cn_m\epsilon_0}\left[\frac{4P}{\sigma_I^2\pi}\right] e^{\frac{-\left(x^2+y^2\right)}{\sigma_I^2}} \tag{6.6}$$

where $E_{x,y}$ is the amplitude of the electric field at the given location, $I_{x,y}$ is the field intensity distribution which we know to be approximately Gaussian, I_0 is the peak intensity of the 2D Gaussian intensity distribution, $P = \int\int_{-\infty}^{\infty}\frac{1}{4}I_{x,y}\mathrm{d}x\mathrm{d}y = \frac{1}{4}\pi\sigma_I^2 I_0$ is total power of the incident beam which is related to the peak intensity of the Gaussian standing wave intensity distribution, σ_I is the width of the Gaussian intensity distribution, n_m is the refractive index of the medium, c is the speed of light in vacuum, ϵ_0 is the dielectric permittivity in vacuum, and α is the complex polarizability of the particle using the Clausius-Mossotti relation (equation (6.8)) in conjunction with the radiative reaction correction (equation (6.7)) [39, 196, 202]:

$$\alpha = \frac{\alpha_0}{1 - \frac{ik^3\alpha_0}{6\pi\epsilon_0\epsilon_m}} \tag{6.7}$$

$$\alpha_0 = 4\pi\epsilon_0\epsilon_m a^3\left[\frac{\epsilon_p - \epsilon_m}{\epsilon_p + 2\epsilon_m}\right] \tag{6.8}$$

where a is the radius of the particle, ϵ_p is the dielectric constant of the particle, ϵ_m is the dielectric constant of the medium, and $k = \frac{2\pi n_m}{\lambda_0}$ is the wavenumber

$\lambda_0 = 1064nm$	$\epsilon_0 = 8.85 \times 10^{-12} \frac{s^2C^2}{m^3kg}$	$k_B = 1.38 \times 10^{-23} \frac{m^2kg}{Ks^2}$
$P = 130mW$	$\epsilon_p = -26.18 + i1.85$ [203]	$T = 295K$
$a = 100nm$	$\sqrt{\epsilon_m} = n_m = 1.33$	$c = 3 \times 10^8 \frac{m}{s}$

Table 6.1: Experimental system parameters used to calculate the width of the beam used to generate the pancake trap from the probability distribution data shown in figure 6.2.

of the excitation light in the medium. Using equation (6.6) with equation (6.2) yields:

$$\frac{1}{A} e^{\frac{-(x^2+y^2)}{\sigma_p^2}} = \frac{1}{Z} e^{\left(\frac{4\alpha P}{\sigma_I^2 \pi c n_m \epsilon_0 k_B T}\right) e^{\frac{-(x^2+y^2)}{\sigma_I^2}}} \tag{6.9}$$

$$\approx \frac{1}{Z} e^{\frac{-4\alpha P(x^2+y^2)}{\sigma_I^4 \pi c n_m \epsilon_0 k_B T}} \tag{6.10}$$

where the Gaussian function within the exponent in equation (6.9) was approximated by Taylor expansion to the first non-zero term. Therefore, in this case where the particles displacement from the center of the Gaussian intensity profile is generally much smaller than the width of that intensity profile ($x^2 + y^2 \ll \sigma_I^2$), we can approximate:

$$\sigma_I^4 \approx \frac{4\alpha P \sigma_p^2}{\pi c n_m \epsilon_0 k_B T} \tag{6.11}$$

From our measurement of the width of the probability distribution shown in figure 6.2, we find $\sigma_p \approx 0.83\mu m$. The remaining parameters are known or are measured directly (see table 6.1). Using the parameters in table 6.1 with equations (6.7), (6.8) and (6.11), we can calculate the width of the Gaussian intensity distribution as $\sigma_I \approx 6.3\mu m$.

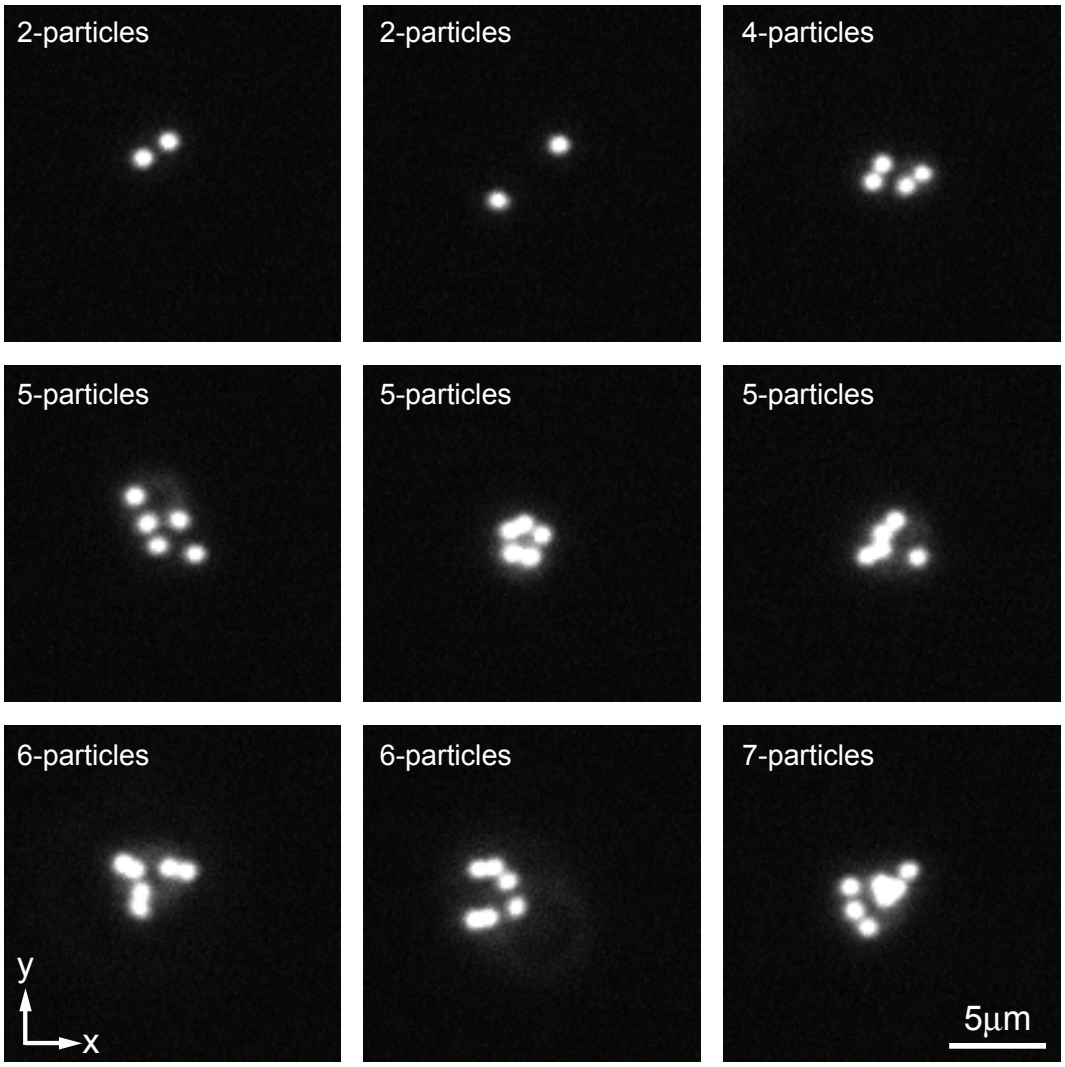

Figure 6.3: Dark-field images of $500nm$ diameter polystyrene particles confined to 2D in the pancake trap. Particles are effectively confined to a single plane (all are in focus) due to strong axial intensity gradients, but are weakly confined in the x and y directions due to the wide diameter of the collimated trapping beam. Interesting 2D behavior can be observed, such as the formation of clusters and "strings." Although, for these particles at the laser power used these formation are not stable. Much of this inter-particle interaction behavior can be attributed to optical binding forces (see chapter 10).

6.4 Single-Plane Alignment of Multiple Particles

I demonstrate the alignment of particles in a single plane using a solution of $500nm$ diameter polystyrene particles in water. Figure 6.3 shows dark field images of particles aligned in the pancake trap. While the particles are free to diffuse in the xy-plane, they are strongly confined along the z-axis. Thus the particles all remain in the focal plane over long timescales. As more particles enter the trap, it becomes clear that the particles begin to form more complex 2D arrangements and display coupled motion. Particles form clusters of various geometries including string-like or chain-like connections, however the interaction here is weak in comparison to the thermal forces which break up the formations rapidly. These intriguing interactions can be attributed to an inter-particle optical force known as the optical binding force. This optical binding interaction is studied in detail in Part II, and the potential for this force to be ultra-strong is exploited to form optical molecules. Such 2D optical molecules are described in chapter 10.

6.5 Summary

A method using a collimated beam for generating a 2D optical trap was demonstrated, and this instrument was named the pancake trap. A single trapped $200nm$ diameter gold particle was monitored over 2 hours, and the resulting position histogram demonstrated a wide, axially symmetric trapping potential. This position histogram could then be used to calculate the diameter of the collimated trapping beam, which was determined to be $12.6\mu m$.

Multiple $500nm$ diameter polystyrene particles were trapped simultaneously showing confinement of particles to a single plane. The pancake trap is the first instrument to provide stable optical trapping of nanoparticles to a wide single plane free in solution. This provides an optimal environment for observing free 2D motion of trapped objects.

Chapter 7

Outlook

7.1 Sorting, Mixing and Assembly of Nanoparticles

There are potentially many uses for the standing wave optical line trap and the pancake trap. For example all-optical sorting, mixing, and assembly of nanoparticles as part of lab-on-chip devices has been of great interest [112, 136, 137]. With the SWOLT, it is possible to stably confine and transport nanoparticles along a well defined path with well defined velocities over long distances ($> 40\mu m$), even at low laser power. In principle, the length of the SWOLT is only limited by the aperture of the front lens of the objective. In our case, this would be about $1.35mm$ (given by the manufacturer). Thus, provided there is enough laser power, transport should be possible over much longer distances than shown here. I have shown that continuous transport can be achieved by utilizing the lateral scattering force to push particles into positions of weak confinement. There, they can be more easily retrieved from the trap and collected, thus creating space for new particles to enter the trap and be transported. Since transport in the SWOLT operates based on the precise balance between the optical gradient and scattering forces, it should be possible to sort particles based on properties which scale differently with respect to these forces. For example, it should be possible to effectively sort

particles of different sizes since $F_{scat}/F_{grad} \propto a^3$. I used a fluid flow to both introduce particles into the trap and retrieve them from the end of the trap. It should also be possible to use multiple SWOLTs to hand off particles from one SWOLT to another which would allow for continuous sorting or mixing of particles. In an advanced arrangement, a three step process can be employed where nanoparticles are first sorted, then arranged, and finally brought together and assembled. The standing wave optical line trap provides the precision necessary to achieve this kind of controlled sorting and assembly of nanoparticles in solution at room temperature.

7.2 Biological Filament Mechanics and Organization

Additionally, there are many biological systems which could be studied more efficiently using the SWOLT or pancake trap. For example, one could study the mechanical properties of biological filaments such as microtubules, actin thin filaments and myosin thick filaments[70, 204–211]. Typically the fibers are fixed to a solid surface on at least one end in order to prevent the fiber from drifting out of the field of view. From this position, the filament can be bent by optical tweezers or the thermal fluctuations of the filament can be observed thereby revealing the mechanical properties of the filament [207, 212]. It would be beneficial to be able to confine single filaments free in solution for long timescales in an alignment within the focal plane. In traditional optical tweezers, the shape of the focal spot intensity distribution is elongated along the optical axis (see figure 1.5). This would cause a trapped

filament to align itself along that axis perpendicular to the focal plane [213]. Additionally, previous methods for generating elongated traps (see chapter 1.5) have demonstrated low trapping stability, especially for nano-objects. By using the SWOLT, it should be possible to stably confine these biological nano-filaments in an alignment within the focal plane using low laser power. This would allow the observation of the thermal fluctuations of the filaments free from surface contact, which could allow for insights into their mechanical properties. Through the optical confinement of the SWOLT, it would also be possible to consecutively add more filaments to the trap thereby creating bundles of an increasing number of filaments. Additionally, actin and myosin filaments can be mixed and one could assemble an active bundle [214–222]. Fiber bundles are prevalent in nature [205, 206, 215, 223–225], however there is currently no model experiment which can systematically study the mechanics of biological bundles. Additionally, it should also be possible to trap fibers in a wide 2D plane using the pancake trap. This would allow full thermal diffusion, including rotation. Potentially the formation of 2D fiber networks could be observed and studied.

7.3 Single-File Diffusion, Pores & Ion Channels

I have shown that particles can be precisely confined to a one-dimensional channel using the SWOLT (chapter 2.3). Particles are not able to pass each other along the length of the trap and thus maintain their order, but the particles are still relatively free to diffuse along the long axis of the SWOLT.

This trapping geometry is therefore an ideal system for studying single-file diffusion dynamics[226]. Typically, these studies are attempted in physical channels such that the particles within the channels come in direct contact with the hard surfaces [176–185, 227–229]. The frictional and drag forces associated with motion near a surface are the major challenge in extracting meaningful information from these systems. Therefore, it would be ideal to use the SWOLT where the particles can be confined to 1D without the presence of surfaces. Single file diffusion plays a major role in many biological functions, such as the transport of molecules through ion channels [186–191], and therefore development of an experimental model system would prove useful in future research studies.

Part II

Assembling "Optical Molecules" Using the Optical Binding Force

Chapter 8

Background

8.1 From Single- to Multi-Particle Interactions

Since the first demonstration of optical trapping using the optical scattering and gradient forces [32, 33, 44, 46, 47], optical manipulation of matter has found wide application not only in fundamental physics but also in fields as diverse as physical chemistry, cell biology and nanotechnology [32, 33, 44, 46, 47, 85, 100, 138, 140, 165, 197, 230]. At first, micrometer sized objects were trapped such as bacteria, while smaller objects required increased laser intensity in order for optical forces to overcome thermal forces. Stable trapping of single atoms was eventually achieved only when advanced techniques for cooling atoms to near absolute zero were employed, thus minimizing thermal motion. Yet the most groundbreaking results came when *multiple* atoms were trapped simultaneously, which is essential for the observation of macroscopic quantum phenomena such as the Fermi gas [231, 232], the Bose-Einstein condensate [233, 234] and the atom laser [235].

Unfortunately cooling is not an option for studying dynamics which occur at room temperature or in aqueous solution, and an efficient way to manipulate and study large numbers of nanoparticles with high precision has yet

to be developed. Multiple particles can be manipulated by using, for example, holographic or scanning optical tweezers [138, 140, 197, 230]. However, such techniques require the laser intensity to be widely distributed, and the specially shaped light fields are easily perturbed by the introduction of additional optics resulting in reduced trapping strength and precision [230]. Therefore particles must typically be micrometers in size in order for optical forces to overcome thermal forces, and precise control is still lost due to thermal motion. Increased laser intensity can be used to generate stronger forces, finer control or for trapping smaller objects. However, the maximal intensity is limited by heating and radiation damage to the sample, such as with biological material [230, 236–239]. Focus has been mainly placed on strengthening the optical gradient force while weakening the destabilizing optical scattering force, such as with variations on optical tweezer geometry [85, 88, 100, 138, 165, 197, 236], yet this path has so far produced only limited improvement.

In the following work I will demonstrate that a third optical force, the optical binding (OB) force [100, 115, 116, 118, 164, 196–201, 240–270], can be used as a powerful tool for high-precision, simultaneous control of multiple nanoparticles without the need for specially shaped light fields. Optical binding was originally assumed to be significant only in intense optical fields and weaker than the gradient force [116, 199]. However, I will show that trapping by optical binding can be 20 times stronger and more efficient than by the gradient force in even the best optimized optical tweezers. This leads to ultra-strong interactions between multiple nanoparticles that freeze their

relative position within tens of nanometers – a realization of "optical matter" [116]. In the following chapters, I will characterize in detail the formed "optical molecules," which resemble traditional molecules where nanoparticles substitute for the atoms, and optical binding forces substitute for the chemical bonds, as model systems for larger scale optical matter.

8.2 Lateral Optical Binding

Shortly after Arthur Ashkin demonstrated the first single beam optical gradient force trap in 1986 [44], many researchers around the world began experimenting with trapping objects in different geometries. On such group was composed of Michael M. Burns and Jean-Marc Fournier of the Rowland Institute of Science in Cambridge, Massachusetts along with Jene A. Golovchenko of Harvard University. In 1989, only a few years after Ashkin's demonstration, Burns and his colleagues experimented with using cylinder lenses to extend the trapping region of a standard single beam optical tweezer. Although this geometry caused the trap to be unstable due to the stronger scattering forces and weaker gradient forces, the team could still align objects to the line intensity profile provided that a transparent glass surface was place behind them to physically prevent the particles from being pushed away by the scattering forces. Figure 8.1 shows the experiment the team performed.

In monitoring the positions of the particles within their optical line trap, the team noticed some intriguing behavior. It was expected that the particles would move smoothly from the outer edges of the line trap to the

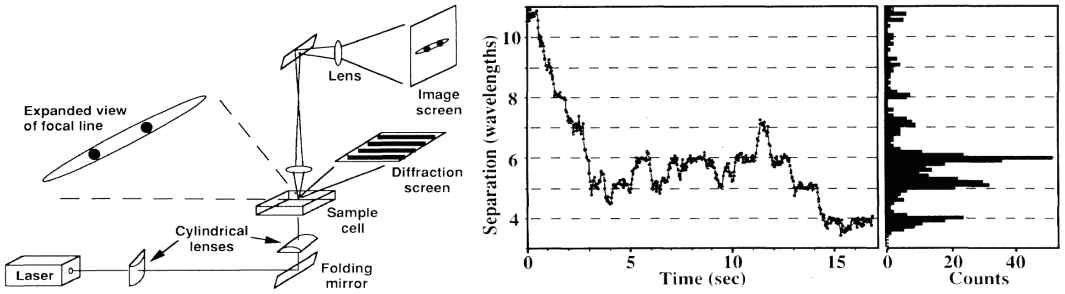

Figure 8.1: Original optical binding experiment by M. M. Burns and colleagues in 1989. The left panel shows the experimental setup. Cylinder lenses are used to focus and stretch the beam to generate a long line intensity profile in the sample for particles to be trapped. The particles, $1.43\mu m$ in diameter, are pressed against a glass surface due to the strong scattering forces. The right panel shows experimental data of the separation distance between two particles in the intensity field as they move toward the high intensity trap center from the outer edges. Figure adapted from reference [115].

higher intensity center by the optical gradient force. This was indeed the case for a single particle in the trap, but when multiple particles were trapped simultaneously their motion was no longer smooth. Instead, the team observed step-like behavior in their positions with step sizes of approximately the wavelength of the excitation light (λ) [115, 116]. Figure 8.1 shows the data they measured for two particles in the same optical line trap. They correctly attributed this step-like motion of the particles to an optical interaction between the two particles which they called the *optical binding force* [115, 116].

Optical binding is different from the optical gradient and scattering forces in that it is an inter-particle optical force, rather than a force applied to the particle directly by the incident laser beam. The magnetic field component ($\vec{B}$) of the scattered optical field from one particles interacts with the

induced electric currents ($\vec{I}$, through rapid oscillations in the dipole moment) of the other particle. This produces a force proportional to $\vec{I} \times \vec{B}$ as given by the Lorentz force relationship. Since the magnitude and direction of these magnetic fields and induced electric currents are oscillating, there is a strong relationship of this optical binding force to the relative phases of these oscillating parameters. This phase difference is determined largely by the separation distance between the particles, as the time for the scattered field from one particle to reach the other is linearly dependent on this distance. For this case where the particles are aligned perpendicular to the axis of excitation light propagation (which is called the *lateral* binding configuration), this means that the optical binding force on the second particle is an oscillating function with respect to the distance between the particles, and the oscillation has a wavelength equal to the wavelength of the excitation light. Therefore, there are locations where the second particle can sit where the magnitude of the force is zero and small displacements result in a restoring force, resulting in a form of optical trapping by optical binding forces. Figure 8.2 shows a plot of the lateral optical binding force as a function of the distance between the two particles and the angle of polarization of the incident beam with respect to the inter-particle axis.

Burns and his colleagues were only able to observe this optical binding interaction in their specially designed line trap which weakened the gradient force along the axis of binding, and the binding forces between particles were far from producing stable trapping locations. Because of this, the team was

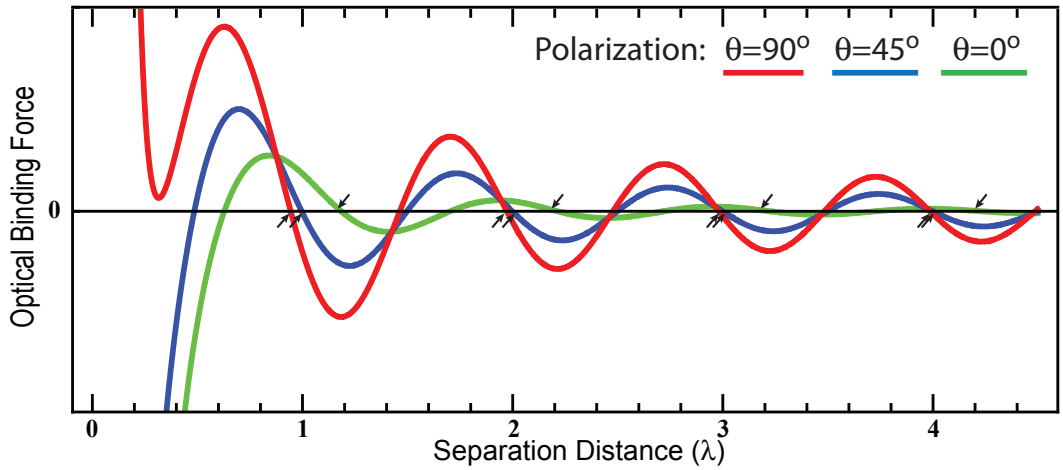

Figure 8.2: Theoretical calculation of the lateral optical binding force oscillation with separation distance. The stable binding positions are marked with arrows and can be seen to shift with change in polarization angle of the incident beam. The calculation was based on the equations in references [196, 240].

quick to assume that the binding force was much weaker than the gradient force and was only significant in intense optical fields [115, 116]. This seemed to make sense as the scattering of light from the particles was only a very small fraction of the excitation light, and this idea pervaded in the optical binding community for the years to come [196, 199]. However, no research team was able to dispel this myth by providing accurate quantitative measurements of the strength of the optical binding force within the Rayleigh regime. The system which Burns and his team used required the particles to be pressed against a surface, and this prevented quantitative measurement of the binding force due to the dampening of the particle motion. In addition, the particles were very large compared to the wavelength of excitation light, and the analytical theories of optical binding forces require the particles to be within the

Rayleigh regime.

Using an optical line trap with no surface with which to press the particles against is typically very unstable as the ratio of the axial gradient forces to scattering forces is much lower than in a point focused optical tweezer. This makes optical binding measurements in such a line trap very difficult as the particles are only "trapped" for very short timescales. The only improved measurement of the lateral optical binding interaction came in 2004 [118]. They were able to trap particles free from surface contact for timescales on the order of 30 seconds, which was far too short to gather enough statistics for a quantitative measurement of the forces. At best they were able to confirm the qualitative properties which were already known, that the optical binding stable positions appear at multiples of the excitation wavelength and have some dependence on the polarization angle of the incident beam.

Although quantitative measurements have eluded scientists, this lateral optical binding configuration where the particles are aligned perpendicular to the incident beam is arguably the most basic form of optical binding. Both particles are excited by the incident beam simultaneously (in phase), which makes the mathematical and conceptual understandings simpler. However, if particles are separated by some distance in the direction of light propagation, their induced dipole moments are now likely out of phase by an amount dependent on the distance they are separated. If the particles are perfectly aligned on the optical axis, this type of optical binding is known as *longitudinal* optical binding.

8.3 Longitudinal Optical Binding

Optical binding between two particles aligned along the propagation axis of the excitation light is known as *longitudinal* optical binding. This is the most well studied experimental system, although the theoretical description is not a simple as in the lateral binding case. There are two main differences between lateral and longitudinal binding. First, the particles in question are not excited in phase with one another but rather with a phase difference associated with the distance between them. Second, the binding forces on the two particles are not symmetric. The scattered photons between the particles are either propagating in the same direction as the incident beam, or in the opposite direction [196, 252, 256]. For example, assume particle A is excited first and particle B is downstream of A. Particle A scatters a photon towards particle B in the same direction as the incident excitation beam with the same wavelength. Since the phase shift between scattered and incident light does not change, the optical binding force on particle B is independent on the separation distance between the two particles. In contrast, particle B scatters a photon toward particle A which is in the opposite direction of the incident beam. Therefore the phase shift between the scattered and incident light depends on twice the distance between the particles and gives the oscillatory behavior of the optical binding force on particle A.

Experimentally however, stable trapping of the two particles along the optical axis requires two counter-propagating beams [242, 246, 249, 250, 252, 256, 269, 271, 272]. So the binding forces on each particle are symmetric in

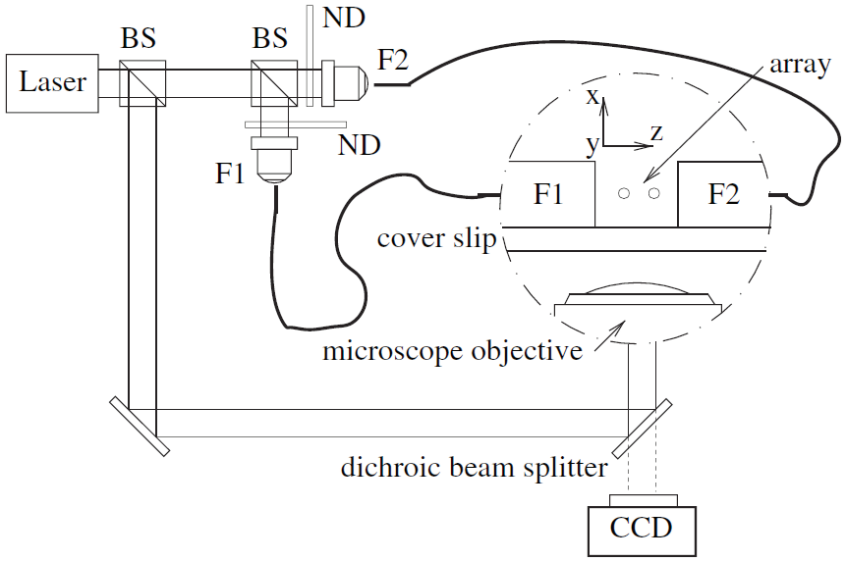

Figure 8.3: Schematic of a typical longitudinal optical binding experiment. An incident laser beam is split evenly between two fiber optical cables. The ends of the fibers are mounted in the sample chamber and particles are trapped between them. Difference in lengths of the fibers is much longer than the coherence length of the laser, thus no standing wave pattern is generated in the sample. Optionally, traditional optical tweezers may be used to position particles within the fiber trap. Figure from reference [250].

this case. Figure 8.3 shows a typical configuration for studying longitudinal optical binding between two or more particles.

While stable trapping of objects is much easier in this longitudinal, counter-propagating system compared to the lateral system, this system has its drawbacks as well. In order to measure optical binding phenomena the particles must be free to move along the axis of binding such that any influences on the motion of the particles along that axis can be attributed to the binding forces. This prohibits use of counter-propagating beams which

generate standing wave patterns which would strongly confine the particles into discrete positions. However, just like Ashkin's original work with counter propagating beams [32], this type of trapping is generally not very stable since the intensity gradients perpendicular to the optical axis are very weak (see chapter 1.2). Therefore, usually particles which are very large compared to the wavelength of excitation light can be stably trapped and studied. However, it becomes difficult to compare with theoretical predictions since simple analytical descriptions are provided only for Rayleigh particles [196], and binding between larger particles generally requires advanced numerical simulations [249, 260, 263, 265, 266].

Improvement to the trapping stability of the counter-propagating geometry has come through using Bessel beams which can generate stronger radial intensity gradients [256]. However, Bessel beams have the unique property that the wavefront propagates as the conical intersection of plane waves traveling at an angle θ with respect to the optical axis. Thus, the component of the wave vector $\vec{k}$ along the optical axis is $|\vec{k}_z| = |\vec{k}| \cos\theta$. This complicates the optical binding description because while the particles scatter photons with wave vector $\vec{k}$, the excitation beam propagates with wave vector $\vec{k}_z$ along the optical axis. So the interplay between the relative phases of the scattered photons and the excitation photons incurs additional phase shifting dependent on the beat frequencies, as shown in figure 8.4. This leads to both long-range and short-range modulation in the optical binding force on the particles. Therefore the optical binding measurements using this configuration must be interpreted

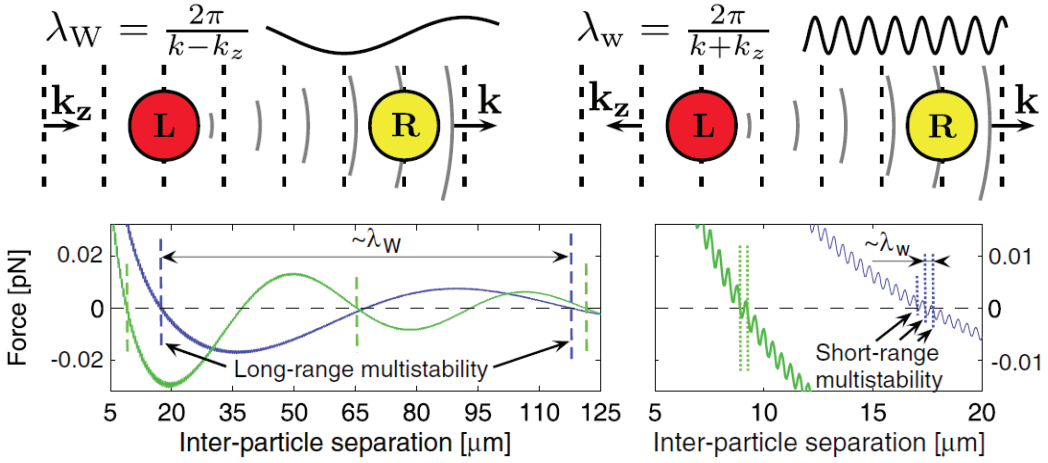

Figure 8.4: Conceptual model of longitudinal optical binding using counter-propagating Bessel beams. Particles are trapped within the field of two counter-propagating Bessel beams. The Bessel beam wavefront propagates with wave vector $\vec{k}_z$ along the optical axis, but the scattered photons propagate with wave vector $\vec{k}$. Thus, the relative phases between incident and scattered photons are modulated by the beat frequencies yielding both long and short wavelength binding positions. Figure adapted from reference [256].

under this even more complicated understanding of the interaction [256]. Still, this non-interfering counter-propagating Bessel beam geometry has yet to produce stable trapping of particles small enough to be suitable for measurements of the optical binding force in the Rayleigh regime.

8.4 Optical Binding in 2D

The optical binding forces are not simply attractive or repulsive, but can also generate torques in two and three dimensions. These multidimensional forces would only be observable if the particles had freedom to rotate about

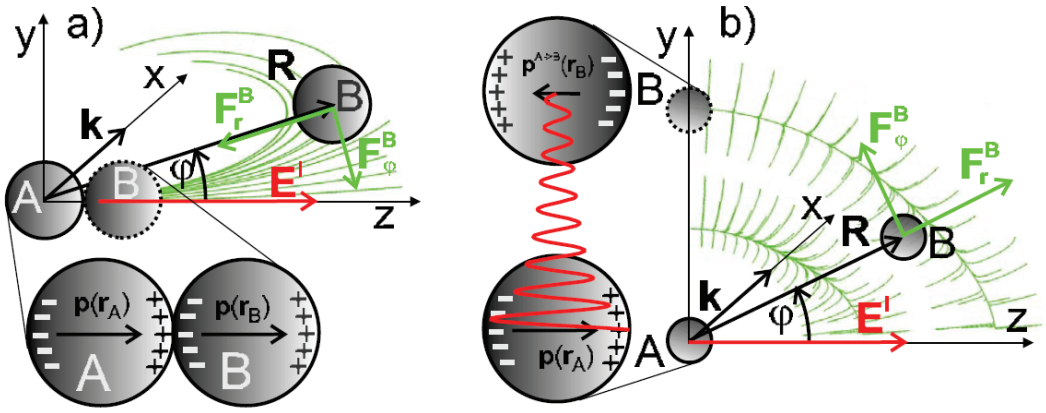

Figure 8.5: Schematic of torques produced by optical binding forces between Rayleigh particles acting in 2D. Green arrows represent the optical binding force field. a) In the near field, the force pulls the particles to align along the axis of light polarization. b) In the far field, the force pulls particles to align perpendicular to the axis of light polarization. Figure from reference [196].

each other, rather than be confined to a single line. Figure 8.5 illustrates the complexity of the optical binding force in 2D and how it can generate torques in the near field and far field. In addition, the organization and self-assembly [273] of nanoparticles through optical binding forces may be better studied in multiple dimensions where much more complex geometries can be accessed. For example, figure 8.6 shows results from numerical simulations of optical binding [199, 274] predicting stable configurations of multiple particles which are held together only through optical binding forces. We can see a distinct difference between the predictions in the ray optics regime and in the Rayleigh regime. Notably, the preferred alignment of the particles with respect to the axis of light polarization is parallel to that axis (horizontal axis) for the ray optics regime which is the opposite of what is predicted for Raleigh particles

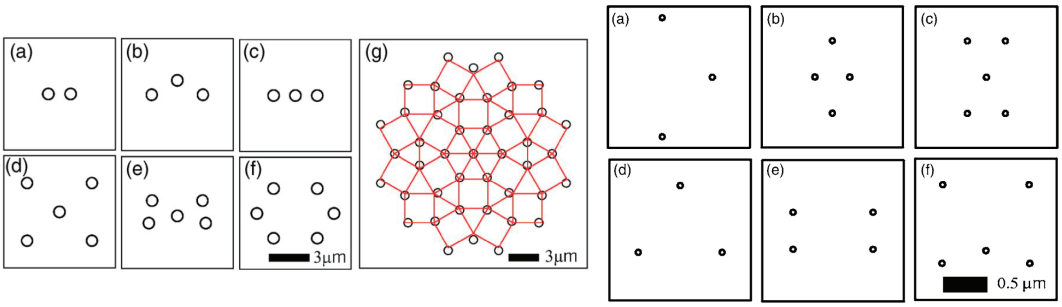

Figure 8.6: Numerical simulations of 2D optically bound clusters in the ray optics regime and in the Rayleigh regime. Left panel: Stable configurations of optically bound particles in the ray optics regime. Right panel: Stable configurations of 33nm diameter Rayleigh particles. All panels drawn to scale. The axis of light polarization is horizontal. Figure adapted from reference [199].

(see also figure 8.5).

Studying optical binding in two dimensions is especially difficult since point-focused or line-focused optical traps do not allow the particles to have freedom of motion in 2D. The current best attempts at observing 2D optically bound structures used evanescent field optical traps [196, 201, 275]. Figure 8.7 shows the experimental system studied and the resulting cluster formations.

As described in chapter 1.5.1, there are several challenges to using evanescent field trapping techniques. First, trapping of particles to a 2D plane is achieved by pulling the particles into contact with a flat surface using the strong gradient forces of the evanescent wave. Thus the mobility of the particles is greatly reduced due to strong frictional forces between particle and surface, and they cannot freely explore all possible binding configurations. Furthermore, in order to compensate for the scattering force which would

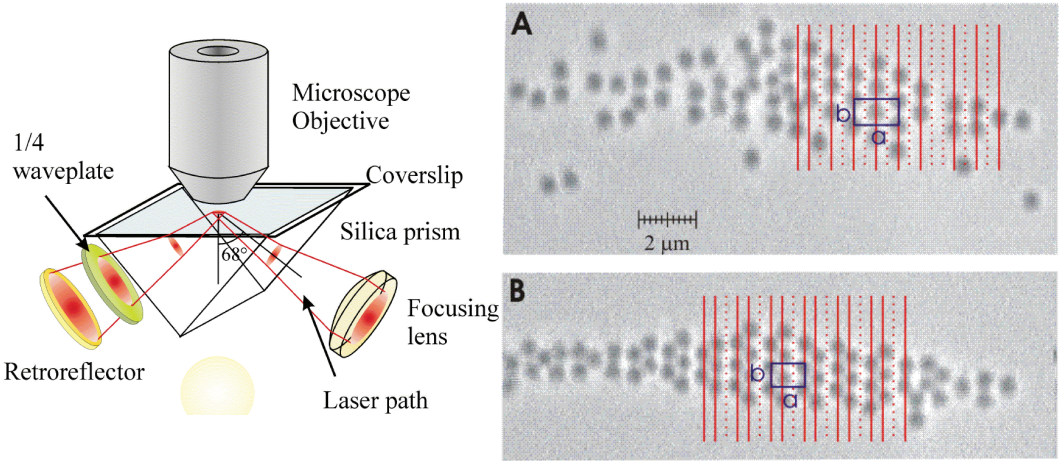

Figure 8.7: Optically bound clusters on a glass surface formed in evanescent field optical trapping. Polystyrene particles $520nm$ in diameter can be seen to form hexagonal structures due to both optical binding forces and the interference pattern generated by the two counter-propagating beams. The red lines show the locations of the intensity maxima of the interference pattern. Figure adapted from reference [201].

otherwise push the particle out of the field of view, a retroreflector was incorporated to generate a counter-propagating beam of equal strength. However, this imposes additional problems. If the interfering beams have the same polarization state, an interference pattern is generated, and therefore the particle arrangement is dominated by this intensity pattern rather than by the optical binding interaction. Figure 8.7 shows that particles are primarily aligned with the interference fringes while optical binding effects play a lesser role. It is possible to rotate the polarization of one of the beams such that the beams are cross polarized. However, the optical binding interaction is strongly dependent on the polarization state of the excitation beam (see figure 8.2 for example). Understanding of optical binding in this case is not straightforward

as the net polarization of the intensity pattern would be elliptical and would vary in its ellipticity as a function of position on the sample surface. Lastly, evanescent field geometries using metal-dielectric interfaces have been used to try to amplify the optical forces. However, these techniques have displayed other effects as thermophoresis, optical spatial soliton propagation, and surface plasma polariton excitation [196, 276, 277], and these effects tend to mask the intrinsic behavior of the optical binding mechanism.

8.5 Why a SWOLT or Pancake Trap is More Efficient

Many of the limitations to measuring the optical binding interaction between Rayleigh particles can be eliminated by using the standing wave optical line trap (chapter 2) or the pancake trap (chapter 6) designs. There are four important criteria in which only these designs can simultaneously meet. First, the trapping stability must be sufficient to trap Rayleigh particles for long timescales (minutes to hours). Second, the particles must be trapped free in solution such that their motion is not dampened from proximity to or contact with a surface. Third, the polarization of the beam must be in a single defined direction at all locations in the trap. And finally, the phase of the incident beam must be uniform at all locations in the plane perpendicular to the propagation axis. As I have described in chapter 1, there are no techniques currently available which simultaneously meet all of these criteria. However, I have shown that the optical trapping instruments developed in Part I, the SWOLT and the pancake trap, do meet these criteria.

Let's consider for example the current best attempts at measuring the optical binding interaction between Rayleigh particles. In the experiments described in reference [118], a line focused optical tweezer was used to trap particles free from surface contact. However, due to the weakened gradient to scattering force ratio in this trapping geometry, their nanoparticles could only be trapped for timescales on the order of 30 seconds. This was only long enough to show qualitative agreement already known optical binding behavior.

In contrast, I can improve these measurements by the dramatically enhanced trapping efficiency of the standing wave optical line trap which allows for stable trapping of nanoparticles for timescales of hours. This potentially allows for gathering at least two orders of magnitude more data of particle positions, which is a significant statistical improvement. Figure 8.8 shows an example of the binding interaction between two $500nm$ polystyrene particles in the SWOLT over the course of 4.7 minutes. We can clearly see that the particles are separated by discrete steps of approximately λ spacing. We can then generate a histogram of the separation distances, which is shown in the top panel of figure 8.9, and again we can see clear peaks which indicate the stable binding positions.

We can further quantify the binding interaction by calculating the energy landscape from the position histogram using Maxwell-Boltzmann statistics (see chapter 10.1.1 for details on this type of calculation). The lower panel of figure 8.9 shows the measured energy landscape of the two particle optical binding interaction. We see now a quantitative measurement of the depths and

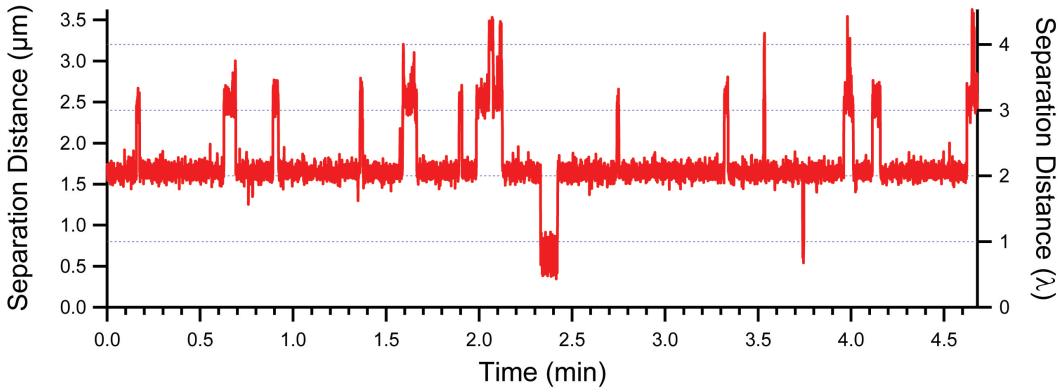

Figure 8.8: Separation distance vs time data series for two $500nm$ diameter polystyrene particles in the standing wave optical line trap. Optical binding effects cause the particles to take on primarily "quantized" position states at distances of multiples of the excitation wavelength ($\lambda = 800nm$ in water). This is indicated in the time series by the discrete steps of the separation distance.

locations of the energy minima. We see that the energy minima get shallower as the distance between the particles increased with the exception of the first energy minimum. The higher energy state of the particles when they are in closer proximity is due to the contribution of electrostatic repulsion between the pair. Aside from this exception, the binding energy of the minima can be seen to decrease roughly linearly with distance, as is predicted in references [115, 116, 196, 241]. Until now, this level of precision in measurement of the optical binding interaction between nanoparticles has not been possible [196]. With this level of improvement, we now aim to study even smaller particles which have a size nearer to the Rayleigh regime. In order to provide the strongest possible optical binding interaction for measurement, we now will use gold particles which are much stronger scatterers than polystyrene. Thus,

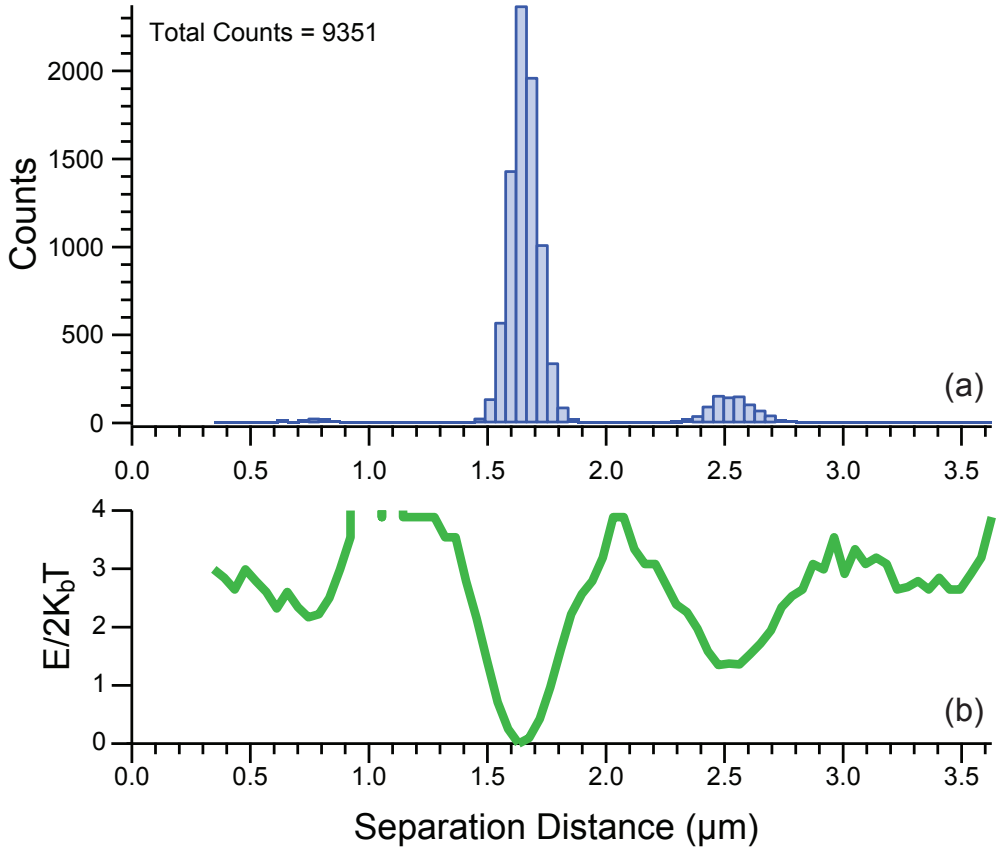

Figure 8.9: Optical binding interaction energy between two $500nm$ diameter polystyrene particles in the standing wave optical line trap. a) Histogram of the separation distances measured from the time series shown in figure 8.8. b) Measured energy landscape of the optical binding interaction in the SWOLT determined from the histogram data. We see clear energy minima at positions near multiples of the excitation wavelength ($\lambda = 800nm$ in water). The depth of the energy minima is seen to decrease with distance, indicating weaker binding strength. The exception is the first minima near $800nm$, which is a higher energy state due to electrostatic repulsion between the particles.

the optical binding interaction between gold should be more easily observed even for smaller particles.

Chapter 9

1D Optical Binding in a SWOLT

Optical binding between a pair of particles can be described by classical electrodynamics, and most simply for Rayleigh particles ($ka \ll 1$, where $k = 2\pi/\lambda$ is the wavenumber of excitation light in the medium and a is the particle radius). However, until now, a detailed quantitative experiment dealing with nanoparticle binding has not been reported [196]. By utilizing the standing wave optical line trap (SWOLT) (see chapter 2), it is possible to stably confine nanoparticles to essentially one-dimension due to the shape of the optical intensity field (see figure 9.1). Individual particles are free to diffuse over many microns along the long axis of the trap (x-axis) while confined to only tens of nanometers along the other two axes. When two or more particles are confined in the same SWOLT, their thermal motion becomes further restricted by optical binding forces. However, this restriction is placed on their relative positions, not absolute positions, resulting in coupled motion. The optical binding energy landscape between two particles is known to be a series of roughly equally spaced energy minima at particle-particle separations of $R_N \approx N\lambda$ where $N = \{1, 2, 3 \ldots\}$. Therefore, it has been observed that particle pairs transiently "hop" between these minima due to their combined thermal energy being larger than the optical binding energy bar-

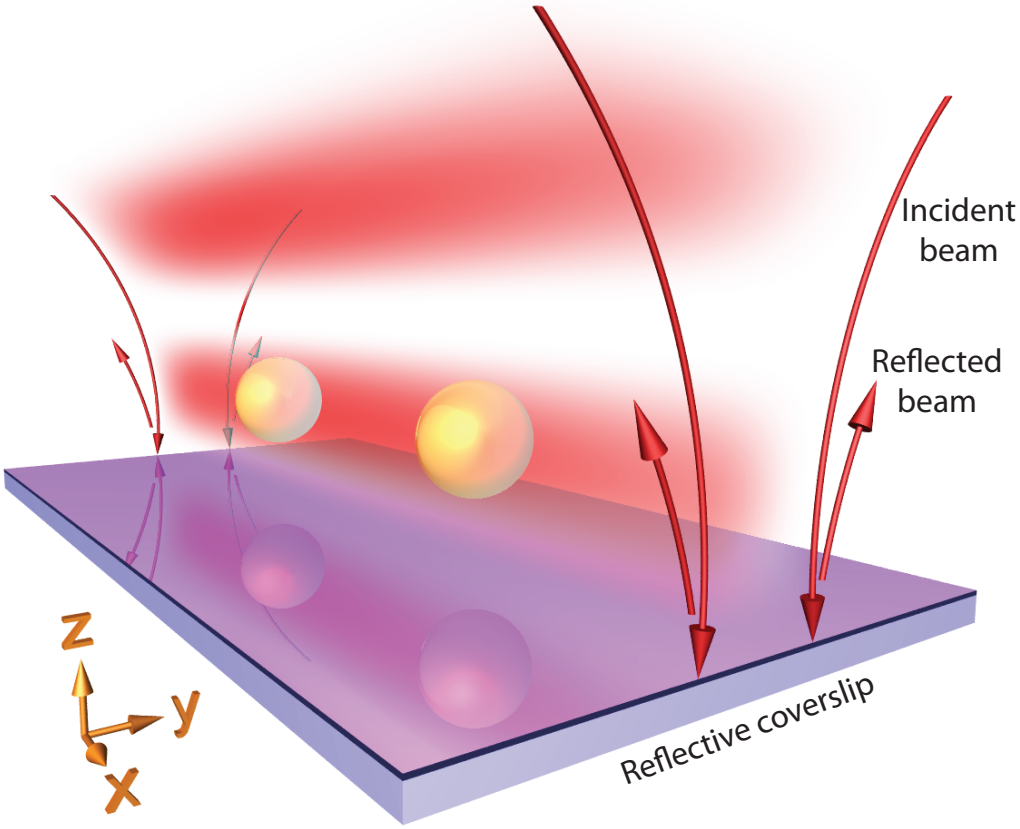

Figure 9.1: 3D schematic representation of two gold nanoparticles trapped and aligned in the first intensity maximum of the standing wave optical line trap. The intensity gradients along the y- and z-axes are much greater than along the x-axis, essentially restricting motion to 1D along the x-axis. Figure from my publication [278].

riers [115, 116, 118]. In the case where optical binding forces dominate over thermal forces, we would expect that the particles maintain a constant separation distance determined by the nearest optical binding energy minimum when the particles become first illuminated. This effect has previously been observed only for very large particles ($ka > 1$) along the axis of light propagation (termed longitudinal optical binding) [242, 246, 256] or for particles whose thermal motion is dampened from contact with a surface [115, 116, 200] as in total internal reflection methods.

In our experiments, we observe dramatic binding strength between particles with size closer to the Rayleigh regime ($ka \approx 0.8$) and in a direction perpendicular to the direction of light propagation (termed lateral or transverse optical binding). This lateral optical binding configuration allows us to precisely image the particles using the same microscope optics which focus the laser and also study the polarization dependence of the optical binding, which is not possible in longitudinal optical binding experiments. Using the SWOLT, we confine $200nm$ diameter gold particles in water ($n_m = 1.33$) using a $\lambda_0 = n_m\lambda = 1064nm$ wavelength laser at roughly $\lambda/4 = 200nm$ above the reflecting coverslip surface. At this distance above the surface, about two particle radii, near-surface effects to optical binding forces have been shown to be minimal [196, 241, 279, 280], and more importantly there is no contact between particle and surface due to the strong axial intensity gradients [88]. There is, however, an effect to the optical binding due to the addition of the reflective coverslip. Figure 9.2 shows a simple ray diagram of the optical binding

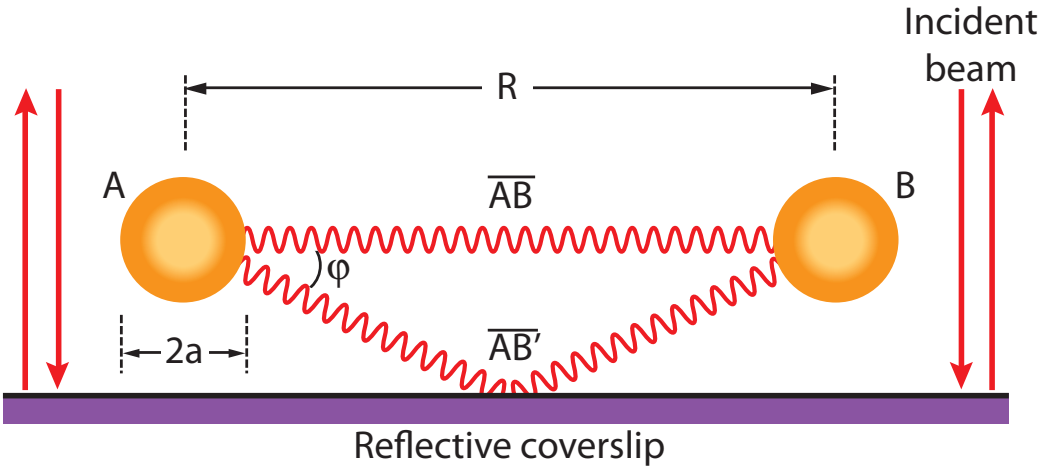

Figure 9.2: Diagram showing the interaction of two particles of radius a via scattered light waves (wavy lines). The optical binding force in this system is due to the direct scattered wave from particle A to particle B (path length $\overline{AB}$), as well as the portion of the scattered wave reflected off the dichroic coverslip surface ($\overline{AB'}$). Figure from my publication [278].

interaction when the particles are near a reflective surface.

Since the particles are only $\lambda/4$ above the coverslip surface, but are separated by distances of multiples of λ, the angle ϕ is small. Therefore we can still consider the binding to be lateral rather than longitudinal, but the magnitude of the binding is roughly doubled by inclusion of this reflection. Additional minor effects on the binding of particles due to this small angle of reflection ϕ can be measured and are discussed in chapter 9.1.2.

9.1 Stable Positions for Optically Bound Particle Pairs

A major discovery of this work was the direct measurement of the optical binding forces between metallic nanoparticles. We actually find that the strength of the optical binding can be one of the strongest optical forces measured when normalized to the required input laser intensity. This was initially noted in my work when I observed that optically bound particles would maintain a precise separation distance of several microns with deviations from that precise separation distances of only a few tens of nanometers. In addition, this precise separation could be maintained over very long timescales (several hours), even when using only modest laser power (typically $P \approx 70mW$, measured in the focal plane). Images of this optical binding behavior is shown in figure 9.3.

Figure 9.3 shows dark-field images of optically bound particles in the SWOLT in different binding positions. We stress that these binding positions are stable for many hours despite thermal fluctuations at room temperature. We prompt particles to hop to different positions either by briefly decreasing laser power (below 10%), thus lowering the optical binding energy barrier, or by releasing and re-trapping the particles (turning the laser off then on). For each binding position, we obtain a video of the particle motion for quantitative tracking and analysis. Figure 9.4 shows histograms of the measured separation distance R between the particles. Eight individual data sets are shown corresponding to the eight peaks in Fig 9.4.

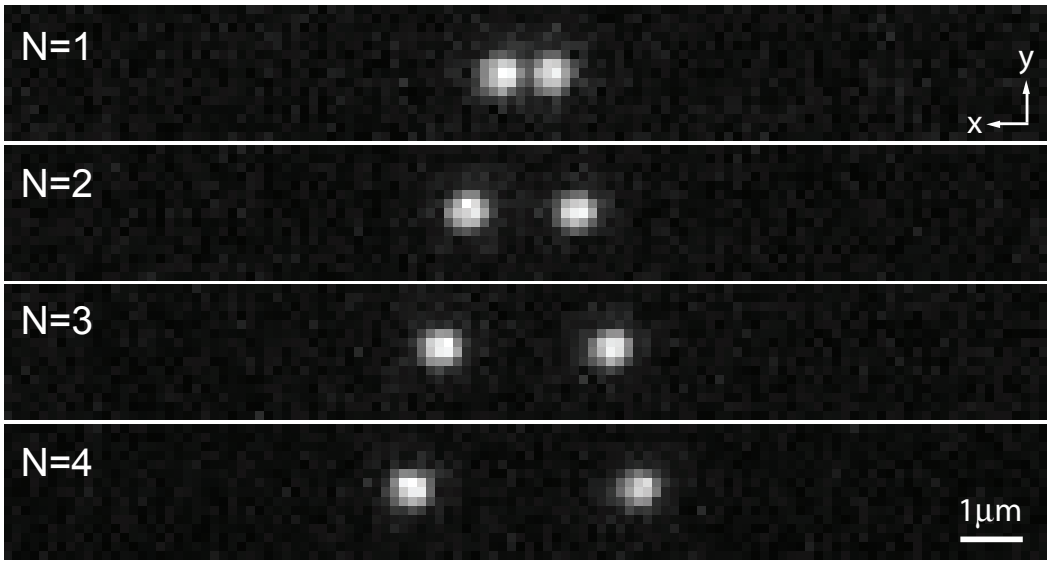

Figure 9.3: Dark-field images of $200nm$ diameter gold particles exhibiting optical binding while confined to 1D motion along the x-axis in the SWOLT. These optically bound particles diffuse easily along the x-axis, but maintain a precise separation distance R over long timescales (typically hours) with only slight fluctuations. Only by releasing and re-trapping the particles can they quickly fall into different binding configurations. The closest (most stable) 4 binding positions are shown. Videos were recorded at 70fps with $10\mu s$ exposure time and particle positions were obtained by video tracking. Scale bar: $1\mu m$. Figure from my publication [278].

The histograms in figure 9.4 show particle separation distances near multiples of the laser wavelength $R_N \approx N\lambda$. However, we can also see deviation from this simple approximation. Notably, we see distinct shifts in the histogram centers when the polarization is rotated for a given binding position N. This shift is on the order of tens of nanometers, and becomes smaller as R increases. This is in agreement with theoretical predictions [196, 240, 241].

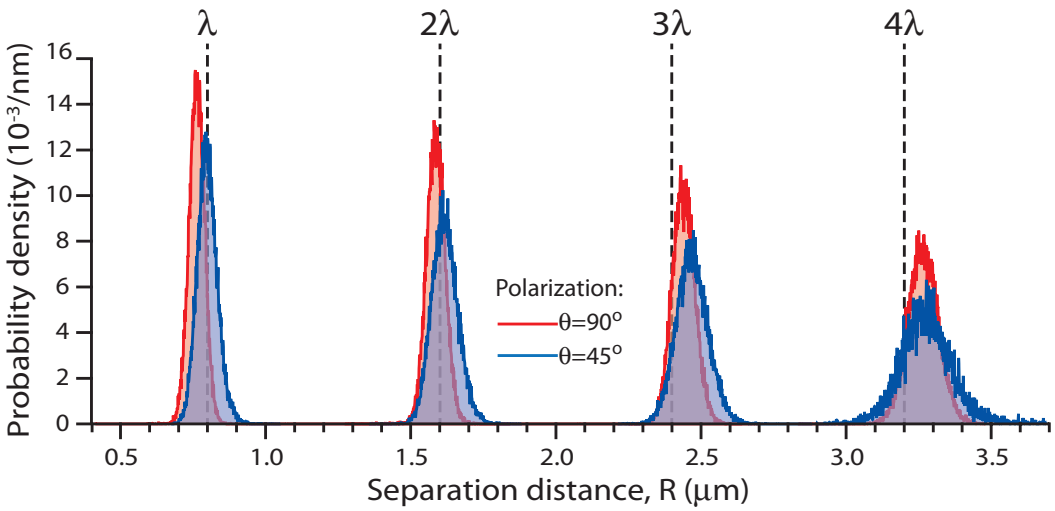

Figure 9.4: Histograms of the particle separation distance were constructed from the data of particle motion. Shown are individual histograms from 8 different data traces using the same pair of gold nanoparticles but in 4 different binding positions and for 2 different polarization angles of the incident laser relative to the binding axis (x-axis). Each histogram is composed of $30,000$ data points ($\approx 7min$ video) except for the histogram of $N = 4$ with $\theta = 45°$ which consists of only $10,000$ data points due to the lower stability. Bin width $= 1nm$. The average binding distance is notably different than simple multiples of the wavelength and shifts when the polarization of the incident light is rotated. The widths of the histograms, while only tens of nm wide, can be seen to increase with greater separation distance, indicating weaker binding as the scattered field decreases in strength with distance. Figure from my publication [278].

9.1.1 Theoretical Optical Binding Stable Positions

We can calculate the theoretically predicted values of separation distance for our specific system parameters for quantitative comparison with the measurements. We start with the formulation of the lateral optical binding (OB) force as given in references [196, 240]:

$$F_x^{AB} = \frac{|\alpha|^2|E_0|^2}{8\pi\epsilon_0\epsilon_m R^4}\Big\{ \left[2k^2R^2\left(2\cos^2\theta - 1\right) + 3\left(1 - 3\cos^2\theta\right)\right]\cos\left(kR\right) + \left[k^3R^3\left(\cos^2\theta - 1\right) + 3kR\left(1 - 3\cos^2\theta\right)\right]\sin(kR)\Big\} \quad (9.1)$$

where R is the distance between the two particles, k is the wavenumber of the excitation light in the medium, θ is the polarization angle of the incident light with respect to the binding axis, α is the effective complex polarizability of the particles [39, 196], E_0 is the amplitude of the electric field on each particle, ϵ_0 is the dielectric permittivity of free space and ϵ_m is the dielectric constant of the medium. This model assumes the particles are in the Rayleigh regime ($ka \ll 1$, where a is the particle radius) such that the electric field throughout the particles volume is uniform, and is induced only by the incident laser. While our experiments are not entirely at the Rayleigh limit ($ka \approx 0.8$), they are closer to the Rayleigh regime than previously reported experiments which have shown reasonable agreement with Rayleigh theory for values of $ka > 1$. It is accepted that Rayleigh theory is a reasonable approximation even for such large nanoparticles [196]. To find the stable binding positions, we solve equation (9.1) for distances R where the optical binding force is zero ($F_x^{AB} = 0$) and small displacements relative to that location results in a restoring force

Binding Position, N	1	2	3	4
$\theta = 90°$	$757nm$	$1579nm$	$2386nm$	$3190nm$
$\theta = 45°$	$799nm$	$1600nm$	$2400nm$	$3200nm$

Table 9.1: Theoretical calculation of stable binding separation distances R_N for parameters matching experimental conditions. Parameters used: $\lambda_0 = 1064nm$, $n_m = 1.33$, and $\theta = \{90° \text{ or } 45°\}$

($\frac{\partial}{\partial R} F_x^{AB} < 0$). With these conditions, we find that the locations of the stable positions R_N are only a function of k and θ. We solve equation (9.1) for the two above conditions numerically. Table 9.1 shows the calculated stable separation distances for our experimental conditions of $\theta = \{90° \text{ or } 45°\}$ and $k = (2\pi n_m)/\lambda_0$, where $n_m = 1.33$ is the index of refraction of the medium (water) and $\lambda_0 = 1064nm$ is the vacuum wavelength of the trapping laser.

9.1.2 Measurements Compared with Theory

Figure 9.5 shows measurements of the average separation distance R_N compared with theoretical predictions of the stable positions for our system and illustrates the precision of our measurements. While the difference between measurement and theory is relatively small ($< 100nm = \lambda/8$), we can see that the particles tend to be separated by greater distances than predicted, especially at larger average separations. This difference arises because the particles are not point objects and from the inclusion of the reflective surface

The theoretical values were calculated using an analytical description of the optical binding force given in references [196, 240]. The model assumes

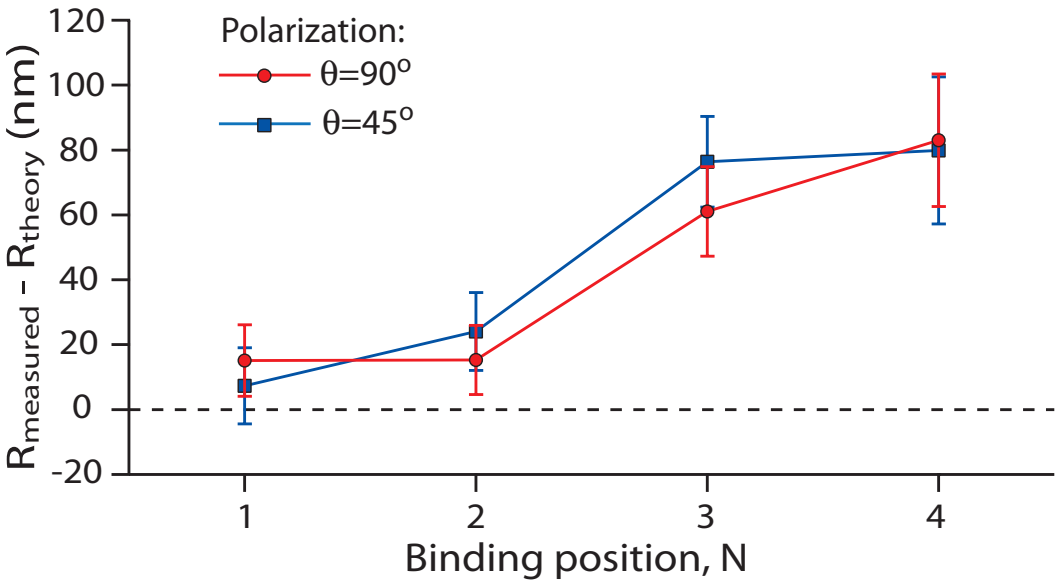

Figure 9.5: The measured average separation obtained from the histograms is compared with theoretical predictions (see chapter 9.1.1). The particles sit further apart than theoretical predictions, but are pulled closer together at shorter separations due to path length differences between the direct and reflected scattered waves (see figure 9.2). The error bars include consideration of the error in least squares fitting, particle tracking algorithm, camera field of view calibration, long timescale drift and the standard error. Figure from my publication [278].

Rayleigh particles ($ka \ll 1$) are used such that the electric field throughout the particle volume is uniform and is induced only by the incident laser. Since we use metal particles, it is likely that the electric field amplitude is not uniform throughout the particle volume, but rather decays exponentially as it passes from particle surface to center by a characteristic length scale known as the skin depth [281]. So it is likely that the particles are not completely transparent, and thus surface atoms of the particles exhibit somewhat stronger optical

binding forces than atoms at the particles centers. Also, the near surfaces likely exhibit stronger binding than the far surfaces which may be slightly shielded by the particle volume itself. Therefore the average optical binding force on the pair would displace the particle centers to be further apart than the above model predicts but still within one particle diameter, which is in agreement with the data shown in figure 9.5. The reflections of the scattered light off the coverslip surface were also neglected in the above model. Figure 9.2 illustrates the paths of the scattered light which determine the binding position. For shorter binding distances, the difference in path length for the direct ($\overline{AB}$) and reflected ($\overline{AB'}$) rays becomes significant, and can be approximated by $R_N - R_N \cos\phi \approx 115nm$ for $N = 1$. Figure 9.5 shows that as N decreases (ϕ increases), the particles are pulled closer together by up to about $60nm$, half this path length difference. In the future, more comprehensive calculations or simulations of metal particles may be required [241, 249, 260, 279].

9.2 Characterizing the Strength of the Optical Binding Force

If we are to consider the optical binding observed in these experiments as one of the strongest optical forces, it is then important to accurately quantify the strength of these optical binding forces so they can be compared to the strength of typical optical forces used for manipulation of nanoparticles in the optics, biophysics, and nanotechnology communities. The widths of the histograms in figure 9.4 can be used as reporters on the precision and strength

of the optical binding forces. A stronger force would yield stronger coupling of the motion of the two particles. This in turn would cause their separation distance to become more precisely confined around the specific binding distances noted in the previous section (chapter 9.1). We can see in figure 9.4 that as the separation distance increases, the widths of the histograms also increase which indicates weaker binding. This is due to the magnitude of the scattered field decaying with distance from the scatterer. We also see weaker binding when the polarization angle θ decreases because the scattered field is weaker and decays much more quickly along the axis of the induced dipole moment. These qualitative results are in agreement with theory [196, 199, 240, 241].

9.2.1 Quantitative Binding Strength Measurement

Quantitative measurements of the optical binding spring constants can be made using the time-series data of the particle motion. Since the optically bound particles keep a precise separation distance R_N with only slight thermal fluctuations about this distance, we can model the optical binding force between them as a spring of rest length R_N and spring constant κ_N which joins the particles. This model is illustrated in figure 9.6.

The thermal fluctuations of the particle-particle separation distance about the average binding position R_N is related to the spring constant κ_N through Maxwell-Boltzmann statistics. From each of the 8 individual time-series data sets (for $N = \{1, 2, 3, 4\}$ and $\theta = \{90°, 45°\}$), we calculate the probability (W) of the particles to be separated by a distance R and plot the

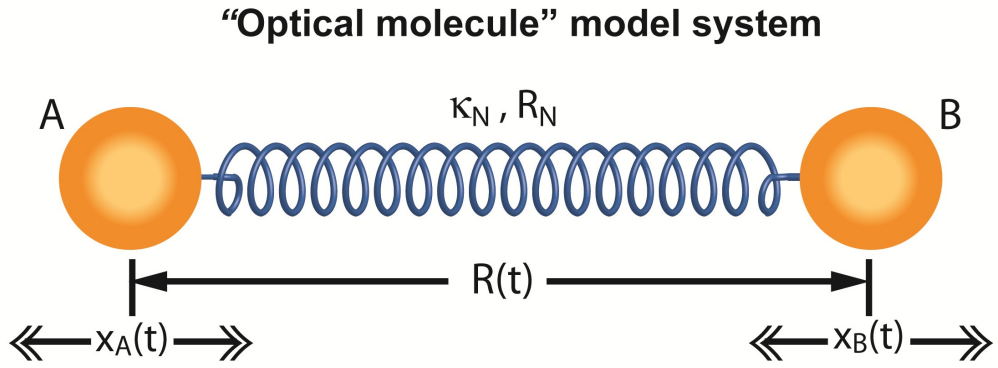

Figure 9.6: Ultra-stable optically bound particle pairs can be modeled as two particles attached by a spring of rest length R_N and spring constant κ_N. Each particle contains thermal energy of k_BT which causes fluctuations in the measured center-to-center distance $R(t)$ about R_N. Figure from my publication [278].

histograms of the probability distributions $W(R)$ (which is what is shown in Figure 9.4). The probability of finding the particles at a given separation R is related to the energy U of being in that position normalized to the thermal energy of the system ($2k_BT$ for a two particle system) through Boltzmann statistics as:

$$W_N(R) = \frac{1}{Z} e^{\frac{-U(R-R_N)}{2k_BT}} \tag{9.2}$$

where $k_B = 1.38 \times 10^{-23} \frac{m^2 kg}{Ks^2}$ inf is Boltzmanns constant, $T \approx 295K$ is the temperature of the sample (room temperature), and $Z = \int_{-\infty}^{\infty} e^{\frac{-U(R-R_N)}{2k_BT}} \mathrm{d}R$ is a normalizing factor ensuring the total probability is 1. Since the measured probability distributions are approximately Gaussian, modeling the energy landscape as a harmonic potential is reasonable: $U\left(R - R_N\right) = \frac{1}{2}\kappa_N \left[R - R_N\right]^2$.

Thus the probability can be expressed as:

$$W_N(R) = \frac{1}{A} e^{\frac{-[R-R_N]^2}{\sigma_N^2}} = \frac{1}{Z} e^{\frac{-\kappa_N [R-R_N]^2}{4k_B T}} \tag{9.3}$$

where σ_N is the width of the Gaussian probability distribution, and $A = \int_{-\infty}^{\infty} e^{\frac{-[R-R_N]^2}{\sigma_N^2}} \mathrm{d}R = \sigma_N \sqrt{\pi}$ and $Z = \int_{-\infty}^{\infty} e^{\frac{-\kappa_N [R-R_N]^2}{4k_B T}} \mathrm{d}R = \sqrt{\frac{4\pi k_B T}{\kappa_N}}$ each normalize their respective descriptions of the probability distribution. It is then a simple matter to solve equation (9.3) for the relationship between σ_N and κ_N. The next few steps leading from equation (9.3) to (9.6) are shown:

$$\frac{1}{\sigma_N} e^{\frac{-[R-R_N]^2}{\sigma_N^2}} = \sqrt{\frac{\kappa_N}{4k_B T}} e^{\frac{-\kappa_N [R-R_N]^2}{4k_B T}} \tag{9.4}$$

$$\frac{-[R-R_N]^2}{\sigma_N^2} + \ln\left[\frac{1}{\sigma_N}\right] = \frac{-\kappa_N [R-R_N]^2}{4k_B T} + \ln\left[\sqrt{\frac{\kappa_N}{4k_B T}}\right] \tag{9.5}$$

$$\left[\frac{\kappa_N}{4k_B T} - \frac{1}{\sigma_N^2}\right][R-R_N]^2 + \frac{1}{2}\left[\ln\left(\frac{1}{\sigma_N^2}\right) - \ln\left(\frac{\kappa_N}{4k_B T}\right)\right] = 0 \tag{9.6}$$

This equation must be true for any position of the particles $[R - R_N]$, so each term must individually be zero:

$$\left[\frac{\kappa_N}{4k_B T} - \frac{1}{\sigma_N^2}\right] = 0 \tag{9.7}$$

$$\ln\left(\frac{1}{\sigma_N^2}\right) - \ln\left(\frac{\kappa_N}{4k_B T}\right) = 0 \tag{9.8}$$

The solution to both of these equations is the same:

$$\kappa_N = \frac{4k_B T}{\sigma_N^2} \tag{9.9}$$

We can now calculate the spring constants κ_N of each binding position by first fitting Gaussian functions to the probability distributions of the

Binding Position, N	$\theta = 90°$		$\theta = 45°$	
	$\sigma_N(nm)$	$\kappa_N(\frac{pN}{\mu m})$	$\sigma_N(nm)$	$\kappa_N(\frac{pN}{\mu m})$
1	36.8 ± 1.6	12.0 ± 1.1	45.9 ± 2.0	7.7 ± 0.7
2	44.0 ± 1.7	8.4 ± 0.7	62.0 ± 2.9	4.2 ± 0.4
3	54.5 ± 1.2	5.5 ± 0.3	75.4 ± 1.5	2.9 ± 0.1
4	73.1 ± 2.2	3.0 ± 0.2	110.1 ± 2.5	1.3 ± 0.1

Table 9.2: Measured values of the optical binding spring constants κ_N. Values were calculated from the measured Gaussian widths σ_N of the probability distribution data shown in figure 9.4 using equation (9.9). The temperature of the sample was estimated to be approximately room temperature ($T \approx 295K$).

particle separation distances (see figure 9.4) to find the widths of the distributions σ_N. Then we use equation (9.9) to calculate κ_N from σ_N for each of the eight data sets. Table 9.2 shows the measured values of σ_N and the corresponding values of κ_N for each of the four binding positions and two angles of polarization of the incident beam. The error bars for σ_N in table 9.2 include consideration of the error in least squares fitting, particle tracking algorithm, camera field of view calibration, room temperature fluctuations, and long timescale drift. The error bars for κ_N are calculated from σ_N by error propagation through equation (9.9).

9.2.2 Consideration of Particle Heating by Laser Excitation

Heating of objects in optical traps due to laser radiation has been well documented [282–286]. Metallic nanoparticles, such as gold and silver, are known to be especially heated due to their high electrical conductivity

[101, 287–290], and this can affect the interpretation of the measurements due to increased thermal motion. Note that the value of the binding strength determined from the measured thermal fluctuations of the particles requires one to know the temperature T of the sample (see equation (9.9)). Recent experiments [288] have characterized the heating of trapped $200nm$ diameter gold nanoparticles using a $1064nm$ vacuum wavelength laser (equivalent parameters to the experiments described here) in a *standard* optical tweezer design. They found the heating of the gold nanoparticles to be about $242\frac{K}{W}$. However, the standard optical tweezer design utilizes a point-focused laser beam, whereas the focal volume of our standing wave optical line trap (SWOLT) is stretched greatly in one dimension to form a line-focus. Thus the laser power is widely distributed, and much of it misses the trapped gold particles all together. The important parameter to consider is the local laser intensity at the particle location rather than the total laser power used. Using the method described in chapter 9.2.4, we can estimate the peak field intensity (equation (9.20)) of a $1W$ point-focused (by NA=1.3 objective lens) optical tweezer to be about $3.5\frac{W}{\mu m^2}$. Thus, relative to the local laser intensity rather than the total laser power, we estimate the gold particles are heated by about $69\frac{K}{[W/\mu m^2]}$. For our SWOLT at $70mW$, the method in chapter 9.2.4 is used again to estimate the peak intensity (equation (9.21)) to be about $0.018\frac{W}{\mu m^2}$. This laser intensity would yield a temperature increase of the gold nanoparticles of about $1.2K$ (0.4%) which is insignificant. Therefore, we do not expect heating of the gold nanoparticles to play any significant role in our current measurements,

and we can assume the temperature of the sample to be room temperature ($T \approx 295K$).

Additionally, *if there were* significant heating of the particles this would have two primary effects. Heated particles would exhibit greater thermal fluctuations than compared to room temperature, and local heating of the fluid surrounding the particles would lower the local fluid viscosity. If this heating were unaccounted for in our measurements, it would mean our measurements are *underestimates* of the actual optical binding strength since we would have assumed that the larger thermal fluctuations are occurring at room temperature. Thus the binding strength would be *even stronger* than measured here thereby reinforcing our main point that optical binding is ultra-strong.

9.2.3 Consideration of Position Autocorrelation Time

In addition to the temperature of the sample, it is important to consider the exposure time of the camera used to image the motion of the particles. Long exposure times would cause moving objects to appear elongated or *smeared*. This is also known as motion blurring. Such a motion blurring effect would reduce the measurement accuracy of the particle location at any instant in time. The center of the blur may be tracked, but if the object is exhibiting oscillatory motion this would cause the measured amplitude of the fluctuations to be smaller than the actual fluctuations. This is a similar effect to low pass filtering of the "true" time series position data. Since our measurements of the optical binding strength depend on the Gaussian widths of the particle

fluctuations, we must take this motion blurring effect into account. In fact, if significant motion blurring were to be present, we would measure the widths (σ_N) to be smaller than they actually are, which would lead us to calculate stronger optical binding forces than actually exist in our experiments. Since the unprecedented strength of these forces is a primary result of my work, I must take care to reduce the motion blurring or to take it into account in the calculations if it is unavoidably significant.

To determine if there is significant motion blurring when imaging a Brownian oscillator [291, 292] confined in a harmonic potential of spring constant κ_N, we consider its position autocorrelation time (τ):

$$\tau = \frac{\gamma}{\kappa_N} = \frac{6\pi\eta a}{\kappa_N} \tag{9.10}$$

where γ is the Stokes drag coefficient, $\eta = 0.001\frac{Ns}{m^2}$ is the viscosity of the surrounding fluid (water at $20°C$), and $a = 100nm$ is the particle radius. This is the characteristic time scale for the particle to traverse the potential energy well it is contained in. In order to obtain accurate measurements of the location of the particle through dark-field imaging, we must make sure that the camera exposure time is much shorter than this time scale to avoid the motion blurring effect. We calculate that the shortest autocorrelation time in our series of experiments is:

$$\tau \approx \frac{6\pi\left(10^{-3}\frac{Ns}{m^2}\right)\left(10^{-7}m\right)}{12\times10^{-6}\frac{N}{m}} = 157\mu s \tag{9.11}$$

Therefore we set the exposure time of the CCD camera used to image the particles to $10\mu s$, more than an order of magnitude shorter which is sufficient to

avoid significant motion blur and accurately image the instantaneous positions of the particles. Using the method described in references [207, 293], we find that the error in our measurements due to motion blurring is less than 2% when using this exposure time.

9.2.4 Theoretical Calculation of Optical Binding Strength

Now we can also compare our quantitative measurements of the optical binding spring constants with theoretical estimates using equation (9.1) with one correction. The introduction of the reflective surface (reflectivity $> 99\%$ for $1064nm$ vacuum wavelength in water) in our system creates an additional optical binding path, $\overline{AB'}$, in addition to the direct path, $\overline{AB}$ (see figure 9.2). But since the particle-coverslip distance is small ($\approx \lambda/4$) compared to the particle-particle separation distance ($R_N \approx N\lambda$), the angle of reflection and path length difference are also small. Thus the binding due to reflection has approximately the same magnitude as the direct binding, and we can estimate the total binding force to be:

$$F_x^{AB} + F_x^{AB'} \approx 2F_x^{AB}. \tag{9.12}$$

The optical binding spring constants κ_N are then calculated for each stable position R_N using Hookes law:

$$\kappa_N = -\left[\frac{\partial}{\partial R} 2F_x^{AB}\right]_{R \to R_N} \tag{9.13}$$

The values of κ_N are computed numerically using equation (9.1) with (9.13) and using the data in table 9.1 as the values of R_N. Experimentally measured

values or estimates are used for the remaining parameters: $\lambda_0 = 1064nm$, $n_m = \sqrt{\epsilon_m} = 1.33$, $\epsilon_0 = 8.85 \times 10^{-12} \frac{s^2 C^2}{m^3 kg}$, and $\theta = \{90^\circ \text{ or } 45^\circ\}$. The complex effective polarizability α was calculated as in references [39, 196]:

$$\alpha = \frac{\alpha_0}{1 - \frac{ik^3\alpha_0}{6\pi\epsilon_0\epsilon_m}} \tag{9.14}$$

$$\alpha_0 = 4\pi\epsilon_0\epsilon_m a^3 \left[\frac{\epsilon_p - \epsilon_m}{\epsilon_p + 2\epsilon_m}\right] \tag{9.15}$$

where α_0 is the polarizability of the particle using the Clausius-Mossotti relation, and α is the radiative reaction correction to α_0. Values of the particle radius ($a = 100nm$) and dielectric constant ($\epsilon_p = -26.18 + i1.85$ for gold [203]) were estimated from the manufacturers specifications of particle size and from the known dielectric constant of gold. The amplitude of the electric field E_0 at the locations of the particles in the standing wave optical line trap (SWOLT) was calculated as:

$$|E_0|^2 = \frac{2I_{x,y}}{c\epsilon_0 n_m} \tag{9.16}$$

$$= \frac{2(4P)e^{\frac{-x^2}{\sigma_x^2}} e^{\frac{-y^2}{\sigma_y^2}}}{c\epsilon_0 n_m \pi\sigma_x\sigma_y} \tag{9.17}$$

$$\approx \frac{2(4P)}{c\epsilon_0 n_m \pi\sigma_x\sigma_y} \tag{9.18}$$

where $c = 3 \times 10^8 \frac{m}{s}$ is the speed of light in vacuum, and $I_{x,y}$ is the intensity of the light field at a location (x, y) relative to the location of peak intensity defined as $(0, 0)$. For a 2D Gaussian beam centered about the origin $(0, 0)$, the intensity at each location is related to the total power ($P \approx 70mW$, measured

in the focal plane) and the dimensions (σ_x,σ_y) by:

$$I_{x,y} = \frac{P e^{\frac{-x^2}{\sigma_x^2}} e^{\frac{-y^2}{\sigma_y^2}}}{\pi \sigma_x \sigma_y} \tag{9.19}$$

Since the particles are only displaced from the center of the SWOLT intensity profile by at most a few microns along the long axis (x-axis) compared to the width of the beam ($\sigma_x \approx 15\mu m$), and are not displaced along the y-axis (except by small thermal fluctuations), we can approximate the intensity as:

$$I_{x,y} \approx I_0 = \frac{P}{\pi \sigma_x \sigma_y} \tag{9.20}$$

If we now take into account the amplification of the intensity due to the standing wave (interference of two counter-propagating waves of equal power), the intensity increases by a factor of four:

$$I_0^{SW} = \frac{4P}{\pi \sigma_x \sigma_y} \tag{9.21}$$

Finally, the width of the diffraction limited focal spot is estimated using the well-known relation:

$$\sigma_y \approx \frac{\lambda_0}{2 n_m NA} \tag{9.22}$$

where NA is the numerical aperture of the focusing lens. We use a Plan-Neofluar 100x/1.3 Oil Iris (Carl Zeiss, Germany) objective lens for focusing the laser and forming the SWOLT. The built in iris allows us to reduce the numerical aperture slightly in order to image using dark-field microscopy. We estimate the adjusted numerical aperture to be $NA \approx 1.2$. Taking into account the above parameters, we perform the calculation of the spring constants κ_N

Binding Position, N	1	2	3	4
$\theta = 90°$	$12.0\frac{pN}{\mu m}$	$6.2\frac{pN}{\mu m}$	$4.1\frac{pN}{\mu m}$	$3.1\frac{pN}{\mu m}$
$\theta = 45°$	$6.6\frac{pN}{\mu m}$	$3.2\frac{pN}{\mu m}$	$2.1\frac{pN}{\mu m}$	$1.6\frac{pN}{\mu m}$

Table 9.3: Theoretical calculation of optical binding spring constants κ_N for the first 4 stable binding positions. Parameters used match experimental conditions (see text).

using equations (9.1) and (9.13) at the stable positions R_N given in table 9.1. The results are listed in table 9.3:

9.2.5 Theory of Binding Strength Decay vs. Distance

If one intends to use the optical binding force for assembly of optical matter or for optical manipulation of matter, it is important to know how the optical binding force decays with distance. While equation (9.1) provides the lateral optical binding force for all particle pair orientations within a plane perpendicular to the direction of light propagation, the form is very complex with multiple oscillatory terms. Here, I will simplify the equation to reveal the "envelope" function which describes the general decay of the optical binding strength of the stable binding positions.

A simple approximation to equation (9.1) can be made in the case of the far-field limit ($kR \gg 1$). If all variables are non-zero (including θ), the dominant term is:

$$F_x^{AB} \approx \frac{-|\alpha|^2|E_0|^2k^3}{8\pi\epsilon_0\epsilon_m R}\sin^2(\theta)\sin(kR) \tag{9.23}$$

If we then solve equation (9.23) for the stable separation distances R (when $F_x^{AB} = 0$, and $\frac{\partial}{\partial R} F_x^{AB} < 0$), we find that these distances occur when $kR = 2N\pi$ where $N = \{1, 2, 3 \ldots\}$. If we solve for the spring constants using equation (9.13) with (9.23) and substitute this condition for the stable binding positions we get:

$$\kappa_N \approx \frac{|\alpha|^2 |E_0|^2 k^5 \sin^2 \theta}{8\pi^2 \epsilon_0 \epsilon_m N} \propto \frac{1}{N} \tag{9.24}$$

We find in this simple approximation that the magnitude of the optical binding spring constants decay proportionally to $1/N$ in the far field. This is essentially the same as a $1/R$ dependence if the stable positions are at roughly $R_N \approx N\lambda$.

9.2.6 Binding Strength Measurements Compared with Theory

Now we directly compare our measurements of the optical binding strength with values calculated from theory. Figure 9.7 compares the measured values of κ_N (see also table 9.2) with calculated values (see table 9.3). We see good agreement between our measurements and the predictions by Rayleigh theory. This confirms that my optical trapping scheme (the SWOLT) was able to provide the foundation for direct quantitative study of nanoparticle interactions near the Rayleigh regime. We also see that the optical binding spring constant decreases as roughly $1/N$ as predicted by the simple approximation made in the previous chapter (chapter 9.2.5).

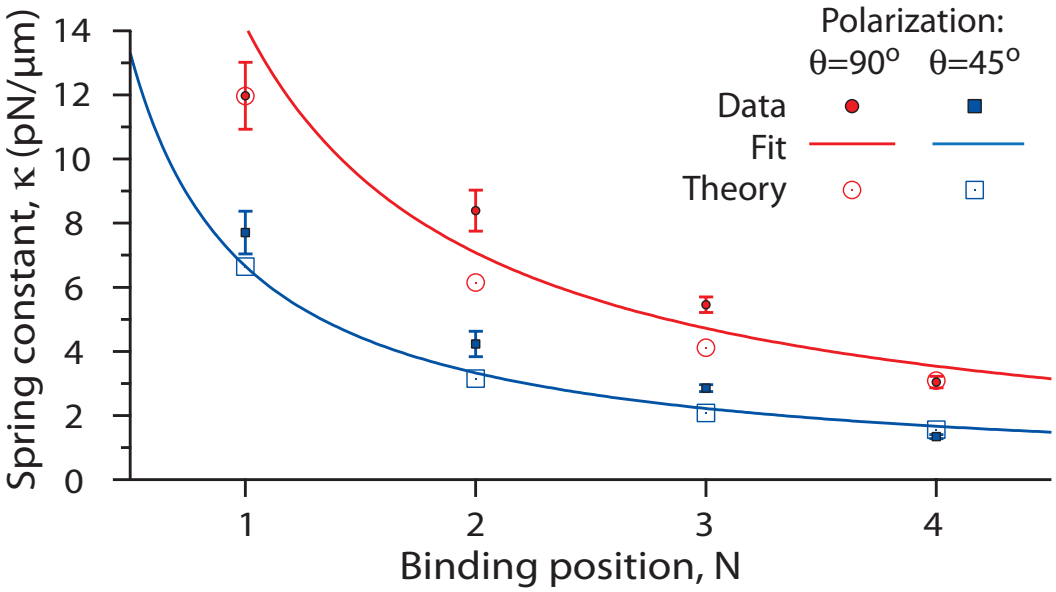

Figure 9.7: The measured optical binding spring constant is compared to theoretical predictions and a β/N fit to the data where β is the only fitting parameter. The inter-particle spring constant κ is calculated directly from the widths of the histograms. The strength of the binding is seen to decrease with distance and with rotation of the polarization of the incident beam as predicted by the theory. The error bars include consideration of the error in least squares fitting, particle tracking algorithm, camera field of view calibration, room temperature fluctuations, and long timescale drift. Figure from my publication [278].

9.2.7 Comparing Optical Binding to Optical Tweezers

The strength of the optical binding force and its decay with distance is an important consideration if one intends to design an instrument for optical manipulation using optical binding forces [245, 248], but equally important is the laser intensity used to generate these forces. Trapping smaller objects generally requires larger laser intensities which may eventually heat or damage the objects [230, 236, 237]. Additionally, it has been shown that biological ob-

jects are particularly susceptible to heating and photo-damage during optical manipulation and can be a limitation for certain biological experiments [236]. Of course the damage increases with increased laser intensity used and has been shown to be highly nonlinear above a given threshold due to generation of multiphoton effects (see for instance references [238, 239]). This threshold can be near intensity levels of a typical optical trapping experiment, only a few tens of $mW/\mu m^2$. Thus it is necessary for researchers to minimize the laser power in order to minimize damage. I therefore use this section to compare my measurements of the optical binding strength relative to the laser intensity needed to generate those forces with the most well developed and commonly used optical manipulation technique, optical tweezers (OT).

We therefore define the *trapping efficiency* (ξ) as the spring constant of the trapping force (κ) normalized to the local intensity of the light field at the location of the particle ($I_{x,y}$). If the intensity field is Gaussian distributed and the particle is near the location of peak intensity (I_0) we can approximate:

$$\xi \equiv \frac{\kappa}{I_{x,y}} = \frac{\kappa}{I_0 e^{\frac{-x^2}{\sigma_x^2}} e^{\frac{-y^2}{\sigma_y^2}}} \approx \frac{\kappa}{I_0} \tag{9.25}$$

where x and y are the coordinates of the particle relative to the center of the 2D Gaussian intensity profile, and σ_x and σ_y are the widths of the profile. The peak intensity of a Gaussian beam is related to the total power (P) by $I_0 = \frac{P}{\pi\sigma_x\sigma_y}$. In the case of a standing wave, the interference of the incident and reflected beams amplifies the peak intensity by a factor of 4. So in that case $I_0^{SW} = \frac{4P}{\pi\sigma_x\sigma_y}$. We calculate the trapping efficiency due to strongest op-

tical binding forces measured here (at $N = 1$, $\theta = 90°$) for our experimental parameters:

$$\xi_{OB} = \frac{\kappa}{4P}\pi\sigma_x\sigma_y \tag{9.26}$$

$$= \frac{12\frac{pN}{\mu m}}{4 \times 70mW} \times \pi \times 15\mu m \times 0.33\mu m \tag{9.27}$$

$$= 0.67\frac{pN/\mu m}{mW/\mu m^2} \tag{9.28}$$

where the total power P was measured in the focal plane, σ_x was measured as in chapter 9.2.4, and σ_y was calculated using equation (9.22) (see chapter 9.2.4).

To calculate the trapping efficiency of similar sized gold particles in an optimized optical tweezer (OT) of the same wavelength and in the same medium (water), we use the data presented in reference [193]. Using figure 2 of reference [193] we estimate the value $\frac{\kappa}{P} \approx 0.1\frac{pNm}{mW}$ for $200nm$ diameter gold particles. Thus we calculate the trapping efficiency to be:

$$\xi_{OT} = \frac{\kappa}{P}\pi\sigma_x\sigma_y \tag{9.29}$$

$$= 0.1\frac{pN/\mu m}{mW} \times \pi \times (0.30\mu m)^2 \tag{9.30}$$

$$= 0.03\frac{pN/\mu m}{mW/\mu m^2} \tag{9.31}$$

where $\sigma_y = 0.30\mu m$ was calculated for a $NA = 1.3$ lens using equation (9.22) as described in chapter 9.2.4. The ratio of these values is:

$$\frac{\xi_{OB}}{\xi_{OT}} = \frac{0.67\frac{pN/\mu m}{mW/\mu m^2}}{0.03\frac{pN\mu m}{mW/\mu m^2}} = 22.3 \tag{9.32}$$

Therefore, under these experimental conditions, optical binding requires about 22.3 times *less* laser power to generate the same strength optical trap as even the best optimized optical tweezers. Thus, sensitive biological experiments may benefit from applying strong optical forces using far less laser power, thereby causing far less photo-damage and heating.

9.3 Optical Trapping Using Optical Binding Forces

This ultra-efficient optical binding force has potential to be used in new optical trapping designs where sensitivity to laser intensity is a concern. One possible design uses the strong optical binding forces generated between large particles to assist trapping of smaller particles. The dark-field images in figure 9.8 show configurations of large ($200nm$ diameter) and small ($100nm$ diameter) gold particles in the SWOLT. The smaller particles individually fluctuate long distances in the SWOLT, but in the presence of larger anchor particles, they are effectively contained by optical binding forces.

Additionally, optical binding between three or more particles has previously shown intriguing results, such as changes to inter-particle spacing as more particles are added to the system [196, 200, 242, 256]. We find similar results, notably the appearance of spacings of 1.5λ as can be seen in figures 9.8a and 9.8e. This is in distinct contrast to binding between only 2 particles where we only observe spacings near multiples of λ.

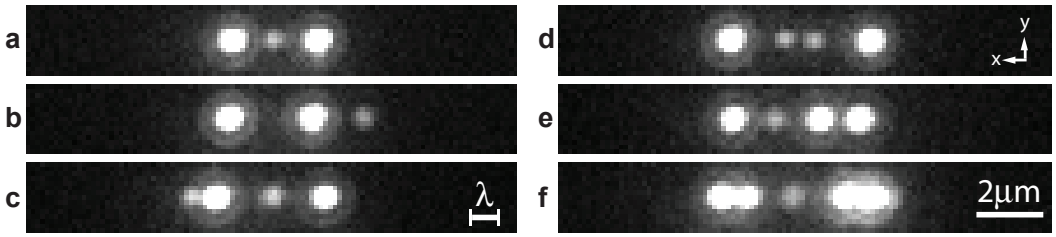

Figure 9.8: Assisted trapping of nanoparticles using optical binding forces. A mixture of $200nm$ and $100nm$ diameter gold particles were trapped and aligned in the SWOLT. For the trapping laser power used ($70mW$ in the focal plane), the smaller particles on their own exhibit large thermal fluctuations along the x-axis. However, by using the larger particles as an anchor, the smaller particles become effectively confined due to the strong optical binding forces. Shown are a few sample configurations of small particles trapped with help from the larger anchor particles. c) Scale bar: $\lambda = 800nm$. Figure from my publication [278].

9.4 Predictions of Optical Binding at the Plasmon Resonance

I have shown that the ultra-strong optical binding interactions between nanoparticles can localize their positions to within a few tens of nanometers. Since the binding strength between two particles (A and B) is dependent on the polarizabilities of the particles (proportional to $\alpha_A \alpha_B$), and the polarizability is dependent on the wavelength of excitation light (see equation 9.14), we expect that we can tune the excitation wavelength to generate maximum optical binding strength for a given set of conditions. This wavelength is known as the plasmon resonance, and has been used to increase the strength of traditional optical gradient force traps [102, 255, 294–299]. We calculate the plasmon resonance using the data for the wavelength dependent refractive

Binding Position, N	$\theta = 90°$		$\theta = 45°$	
	$\sigma_N(nm)$	$\kappa_N(\frac{pN}{\mu m})$	$\sigma_N(nm)$	$\kappa_N(\frac{pN}{\mu m})$
1	3.74	1162	5.02	645
2	5.22	597	7.29	306
3	6.38	400	8.98	202
4	7.37	300	10.4	151

Table 9.4: Calculations of optical binding spring constants for $200nm$ diameter gold particles excited at the plasmon resonance. Additional parameters: $\lambda_0 = 638nm$ and $I_0 = 468\frac{mW}{\mu m^2}$

index of gold as given in references [203, 300–304] and the Clausius-Mossotti relation including the radiative reaction term as in equation (9.14). For $200nm$ diameter gold particles, we calculate the wavelength needed to excite the plasmon resonance as $\lambda_0 \approx 638nm$ in vacuum ($\lambda \approx 480nm$ in water). While the plasmon resonance for gold particles of this size is relatively broad compared to smaller (sub $100nm$) particles, it can still be used to assist in generating even stronger binding between metal nanoparticles (about a 3.5 times stronger spring constant compared to using a $\lambda_0 \approx 1064nm$ laser at the same power). If we assume we use this wavelength laser and the field intensity on the sample is comparable to typical optical tweezer experiments (peak intensity of a diffraction limited Gaussian focal spot when considering $50mW$ of laser power in the sample plane focused by a $NA = 1.3$ objective lens is about $I_0 \approx 468\frac{mW}{\mu m^2}$, we can calculate the expected width of the thermal fluctuations of the particles as described in chapters 9.1.1, 9.2.1 & 9.2.4. We see in the table 9.4 that

Binding Position, N	$\theta = 90°$		$\theta = 45°$	
	$\sigma_N(nm)$	$\kappa_N(\frac{pN}{\mu m})$	$\sigma_N(nm)$	$\kappa_N(\frac{pN}{\mu m})$
1	41.1	9.64	55.2	5.35
2	57.3	4.96	80.1	2.54
3	70.1	3.32	98.6	1.68
4	80.9	2.49	114	1.25

Table 9.5: Calculations of optical binding spring constants for $45nm$ diameter gold particles excited at the plasmon resonance. Additional parameters: $\lambda_0 = 524nm$ and $I_0 = 694\frac{mW}{\mu m^2}$

we should be able to achieve precision of only a few nanometers under these reasonable conditions, even over long range (distance of many wavelengths).

We can also determine the size of the smallest particles that would exhibit similar ultra-strong optical binding behavior under plasmon resonance conditions compared to our experiments with larger 200nm particles but excited off resonance. The plasmon resonance wavelength is size dependent, and so we determine that for gold particles $45nm$ in diameter (2 orders of magnitude smaller in terms of volume than $200nm$ diameter particles) the plasmon resonance is at about $\lambda_0 \approx 524nm$ in vacuum ($\lambda \approx 394nminwater$). The field intensity when we again consider $50mW$ of laser power in the sample plane is $I_0 \approx 694\frac{mW}{\mu m^2}$ (the peak intensity increases because the shorter wavelength results in a smaller focal spot). The results of the calculations are in table 9.5. We see that even for such small particles, if we take advantage of the plasmon resonance we expect to see binding roughly as strong as we currently find in

our experiments for $200nm$ diameter gold with $\lambda_0 = 1064nm$, and $I_0 \approx 18\frac{mW}{\mu m^2}$ (see also table 9.2). We suspect that clusters of more than 2 particles should be even more stable, however more in depth calculations or simulations are needed to solve such multi-bodied systems [199].

9.5 Summary

A description of how the standing wave optical line trap (SWOLT) can be used to study the optical binding force was presented. Pairs of $200nm$ diameter gold nanoparticles were trapped in the SWOLT for timescales on the order of an hour. It was observed that the particles would maintain a precise separation distance on the order or microns with only small fluctuations, on the order of a few tens of nanometers, about distance. This mechanism of particles "locking" into a precise configuration was previously never observed for nanoparticles, and we present a model where two particles are joined by a spring which accurately describes this ultra-strong optical binding interaction.

By recording the positions of the particles over 7 minutes, sufficient statistics could be gathered to accurately and quantitatively determine the optical binding interaction. With the increased trapping stability of SWOLT, over two orders of magnitude more data could be gathered compared to previous best attempts at similar measurements even when we use particles with size much closer to the Rayleigh regime. Therefore the first quantitative measurements of the optical binding force between Rayleigh particles was achieved. In addition, it was discovered that the optical binding force can be over 20

times stronger than the optical gradient force used for trapping in even the best optimized optical tweezers. These measurements were compared with theoretical calculations and were in agreement. We demonstrate that this ultra strong optical binding force could be used as the basis for new optical trapping schemes, such as trapping smaller particles between two or more larger "anchor" particles. Finally we show through calculation that even stronger optical binding forces can be generated by exciting the particles with a wavelength near their plasmon resonance.

Chapter 10

2D Optical Binding in a Pancake Trap

Direct quantitative measurements of the optically coupled motion of nanoparticles within a light field, known as "optical binding" (OB), have until now proven difficult [196]. This has been largely due to a lack of tools which can stably confine nanoparticles free from surface contact and simultaneously allow precise optical imaging. However, I have now provided direct quantitative measurement of the optical binding force between nanoparticles in one-dimension (see chapter 9). These results were only possible through the development of the standing wave optical line trap (SWOLT), which allows nanoparticles to be precisely confined along one-dimension away from surfaces and observed with high resolution video imaging. While numerous new and fascinating dynamics were observed in this 1D experiment, allowing particles to self-assemble in two-dimensions would dramatically increase the possible arrangements and behaviors which can be observed [273]. We can also begin to study the motion of nanoparticle clusters as a whole and how they may couple differently with the external optical field depending on the specific cluster geometry. For example, 2D patterned structures of nanoparticles have been shown to be of use in surprising new plasmonic nanodevices and materials such as for broadband light absorption and photocurrent generation [305, 306].

Until now, quantitative optical binding experiments between nanoparticles in two dimensions has not been possible. This was due to a lack of an efficent tool which can confine nanoparticles to a wide two dimensional plane far from surface contact. However, with the development of the optical pancake trap (PT) (see chapter 6), I solve this exact problem. Figure 10.1 illustrates how multiple nanoparticles can be trapped far from surfaces while confined to a two dimensional plane.

10.1 Optical Binding Energy Landscape for 2 Particles in 2D

While the motion of a single particle in an optical field can be used to study the gradient and scattering forces (see chapter 3 for example), studying the optical binding force requires at least two particles as it is an inter-particle force. It is known that the shape of the 2D optical binding energy landscape depends on the distance (R) between the two particles and the angle (θ) between the inter-particle axis and the polarization axis of the optical field (in our case, aligned with the x-axis) [196, 199, 240]. We can directly measure this energy landscape by trapping exactly two particles in the same plane within the pancake trap and observing the motion of the pair through high resolution dark-field microscopy. The videos can then be analyzed to quantify the 2D interaction. By using a sufficiently weak field intensity ($I_0 \approx 8.2\frac{mW}{\mu m^2}$ peak intensity) such that the particles are free to explore the energy landscape through thermal motion, we can then measure the relative positions of the

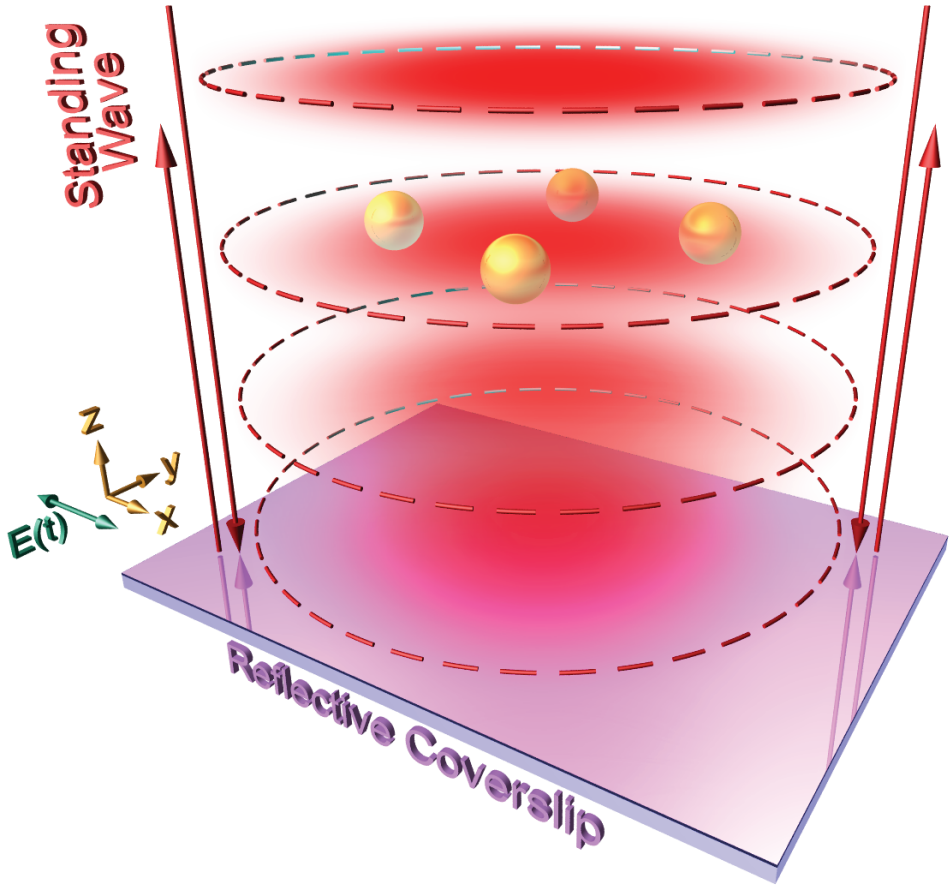

Figure 10.1: Illustration of the optical trapping mechanism of the pancake trap. The intensity distribution of the wide collimated standing wave generates strong axial confinement of particles while generating very weak confinement radially. Particles trapped in a given anti-node of the standing wave are relatively free to move in a single 2D plane. Optical binding effects between strong scattering particles (such as gold particles) can then be observed. The result is generally a self assembly the nanoparticles into different contactless geometries.

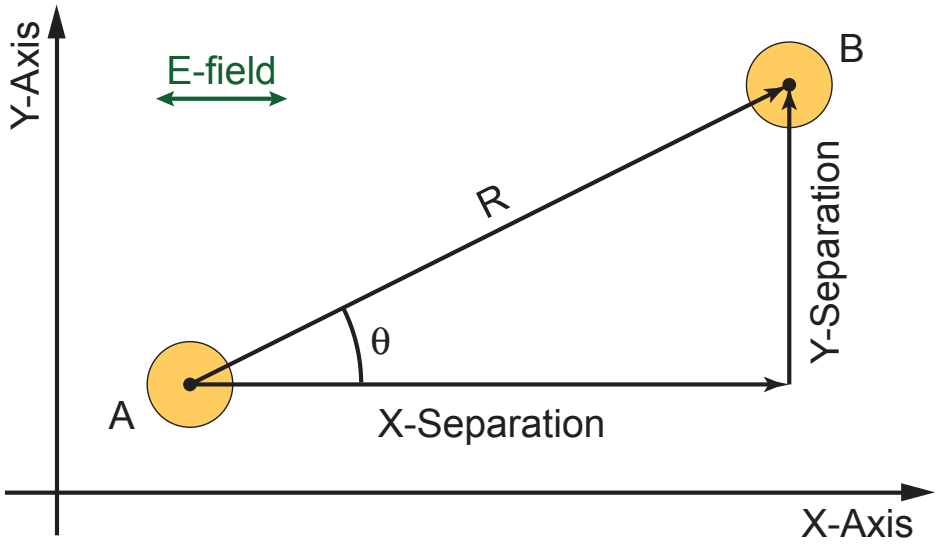

Figure 10.2: Diagram showing how the relative position between two particles is measured in 2D within the pancake trap. The positions of the centers of the two particles (labeled A and B) are tracked for each frame of video, and the relative separation distances can then be calculated.

two particles (figure 10.2) over long timescales. We can use this data to generate a 2D position histogram of the particle-particle separation and from this histogram we can directly determine the energy landscape of the interaction.

10.1.1 Measured Energy Landscape

The probability of finding a pair of particles in a given configuration is related to the potential energy of being in that configuration through Boltzmann statistics:

$$W_{\Delta x,\Delta y} = \frac{1}{Z} e^{\frac{-U_{\Delta x,\Delta y}}{2k_B T}} \tag{10.1}$$

where the configuration of the two particles in two dimensions can be represented by their relative separation distances along the x and y axes $(\Delta x, \Delta y)$, and the total thermal energy of the two particle system is $2k_BT$. If the probability distribution $(W_{\Delta x,\Delta y})$ is measured, it is then a simple matter to calculate the energy landscape $(U_{\Delta x,\Delta y})$ by taking the natural logarithm of equation (10.1):

$$\frac{U_{\Delta x,\Delta y}}{2k_BT} = -\ln\left(W_{\Delta x,\Delta y}\right) - \ln\left(Z\right) \tag{10.2}$$

where $\ln(Z)$ can be considered as an arbitrary additive constant to the energy landscape.

Figure 10.3 shows the measured energy landscape of the 2D, pairwise optical binding interaction within the pancake trap. While the inter-particle axis is essentially free to rotate through any angle (θ), the two-fold symmetry of this interaction allows us to directly map all the data from quadrants $2 \rightarrow 4$ into quadrant 1, thus increasing the statistical significance of each bin of the histogram and corresponding energy landscape. We can see from the measured energy landscape that two particles within the same optical field no longer have complete freedom of motion, but are in fact coupled through optical binding forces, even over long distances. A distinct wavelike pattern is observed which corresponds to the oscillatory nature of the optical binding force with distance. We can also see a strong dependence of the interaction with respect to the orientation of the particle pair. The strongest interaction occurs when the particles are oriented perpendicular to the polarization axis, and the radial locations of the energy minima shift slightly as the orientation is rotated. This

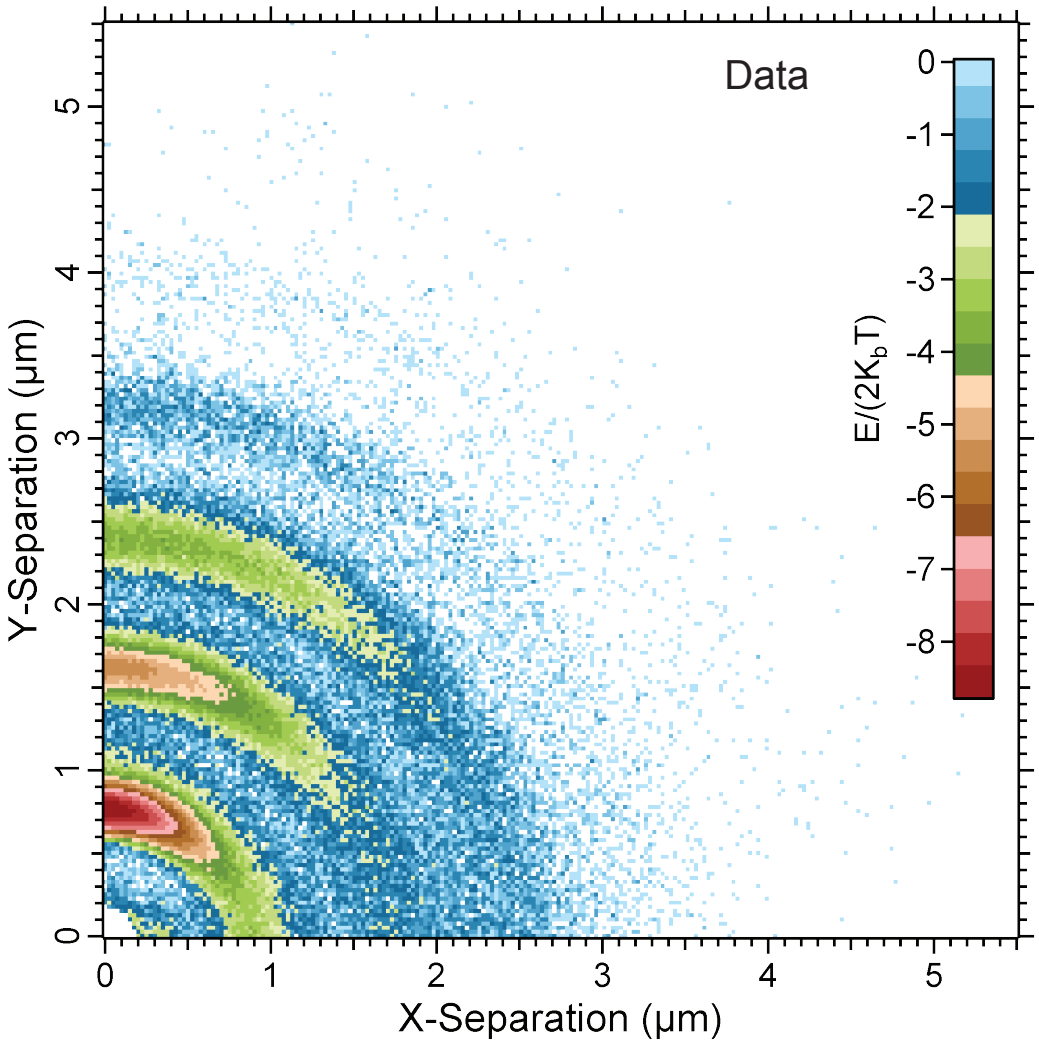

Figure 10.3: Pairwise optical binding energy landscape in 2D. The relative positions over 5.3×10^5 frames (3 hours of video at $50fps$) are used to construct the energy landscape of the pairwise optical binding interaction in two dimensions. We observe a distinct wavelike pattern radially with energy minima at roughly multiples of the laser wavelength ($\lambda = 800nm$ in water). A strong dependence on the angle (θ) can also be seen. This indicates a preference for the pair to orient perpendicular to the polarization axis (x-axis). The energy is normalized to the thermal energy of a two particle system. Bin size $= 25nm \times 25nm$. We can see excellent agreement with the theoretical calculations shown in figure 10.4.

is in excellent agreement with theoretical predictions, and these theoretical calculations are described in the next section (chapter 10.1.2). We also mention that the optical binding interaction may still be significant at much farther separation distances than shown here, as the diameter of the pancake trap was chosen to prevent the particles from straying too far in order to acquire enough statistics in a reasonable timeframe.

10.1.2 Theoretical Energy Landscape

We start with the formulation of the lateral optical binding (OB) force as given in references [196, 240]. The particles within the pancake trap are confined such that movement is restricted to a 2D plane perpendicular to the axis of light propagation. Therefore, we can consider only the two components of the force acting within the trapping plane since there is no significant motion along the third dimension:

$$F_r^{OB} = \frac{|\alpha|^2|E_0|^2}{8\pi\epsilon_0\epsilon_m R^4}\Big\{ \left[2k^2R^2\left(2\cos^2\theta - 1\right) + 3\left(1 - 3\cos^2\theta\right)\right]\cos\left(kR\right) + \left[k^3R^3\left(\cos^2\theta - 1\right) + 3kR\left(1 - 3\cos^2\theta\right)\right]\sin(kR)\Big\} \quad (10.3)$$

$$F_\theta^{OB} = \frac{|\alpha|^2|E_0|^2}{8\pi\epsilon_0\epsilon_m R^4}\sin(2\theta)\left[\left(k^2R^2 - 3\right)\cos\left(kR\right) - 3kR\sin(kR)\right] \quad (10.4)$$

where R is the distance between the two particles, θ is the angle between the inter-particle axis and the polarization direction of the incident light and E_0 is the amplitude of the electric field on each particle. In order to calculate the potential energy due to the optical binding force at a given point (R_2, θ_2) relative to a reference point (R_1, θ_1), we must integrate the force along a given

path (s) connecting these two points:

$$U_{R,\theta}^{OB} = -\int_{(R_1,\theta_1)}^{(R_2,\theta_2)} \vec{F}^{AB} \cdot \mathrm{d}\vec{s} \tag{10.5}$$

We compute that the curl of this 2D force field is equal to zero, and therefore is a conservative force. Thus the energy difference between two points is independent of the path chosen. Therefore, to simplify the integration, we convert equations (10.3) and (10.4) from polar to Cartesian coordinates and integrate numerically. We fix the reference energy point to be $(\Delta x_1, \Delta y_1) = (20\mu m, 20\mu m)$ and integrate to the point $(\Delta x_2, \Delta y_2)$ along two straight line paths: $(20\mu m, 20\mu m) \rightarrow (\Delta x_2, 20\mu m) \rightarrow (\Delta x_2, \Delta y_2)$. Since only the energy difference between two configurations is important, this result is correct up to an arbitrary additive constant.

Finally, we account for the energy contribution of the gradient forces acting on the particles due to the pancake trap (PT) intensity distribution. For a single particle in a 2D Gaussian intensity distribution a distance r from the peak intensity (see also equation (6.6)):

$$U_r^{grad} = -\frac{\alpha}{cn_m\epsilon_0}\left(\frac{4P}{\sigma_I^2\pi}\right)e^{\frac{-r^2}{\sigma_I^2}} \tag{10.6}$$

For the case of two optically bound particles, we make the approximation that the distance each single particle is from the peak intensity is equal to half the separation distance between the particles, $r = \frac{1}{2}R$. Therefore the total potential energy for two particles due to the pancake trap intensity distribution is:

$$U_r^{PT} = -\frac{2\alpha}{cn_m\epsilon_0}\left(\frac{4P}{\sigma_I^2\pi}\right)e^{\frac{-(R/2)^2}{\sigma_I^2}} \tag{10.7}$$

And the total potential energy due to the optical binding forces and the gradient forces is then:

$$U_{R,\theta}^{Total} = U_R^{PT} + U_{R,\theta}^{OB} \tag{10.8}$$

where U_R^{PT} and $U_{R,\theta}^{OB}$ are given by equations (10.7) and (10.5) respectively, and are calculated numerically as described above. The results of this calculation are shown in figure 10.4. These theoretical predictions are in excellent agreement with the measured pairwise optical binding energy landscape shown in figure 10.3 and with my previous experiments done in 1D in the standing wave optical line trap (see chapter 9).

10.2 Two-Dimensional Optical Binding Between 3 or More Particles

Now that the energy landscape of the two particle optical binding interaction has been experimentally measured in detail, the next step is to add more particles to the system and observe multi-body behavior. Again, we use low laser intensity ($I_0 \approx 8.2\frac{mW}{\mu m^2}$) in order to let the particles explore different configurations through thermal motion. Figure 10.5 shows examples of 2D multi-particle optical binding configurations observed in the pancake trap (see also Supplementary Videos 2-5).

While many different configurations can be seen, they are not equally stable. Among the most stable configurations are those that are elongated perpendicular to the polarization axis such as the linear configurations on the left-hand side of figure 10.5. This preference to align perpendicular to

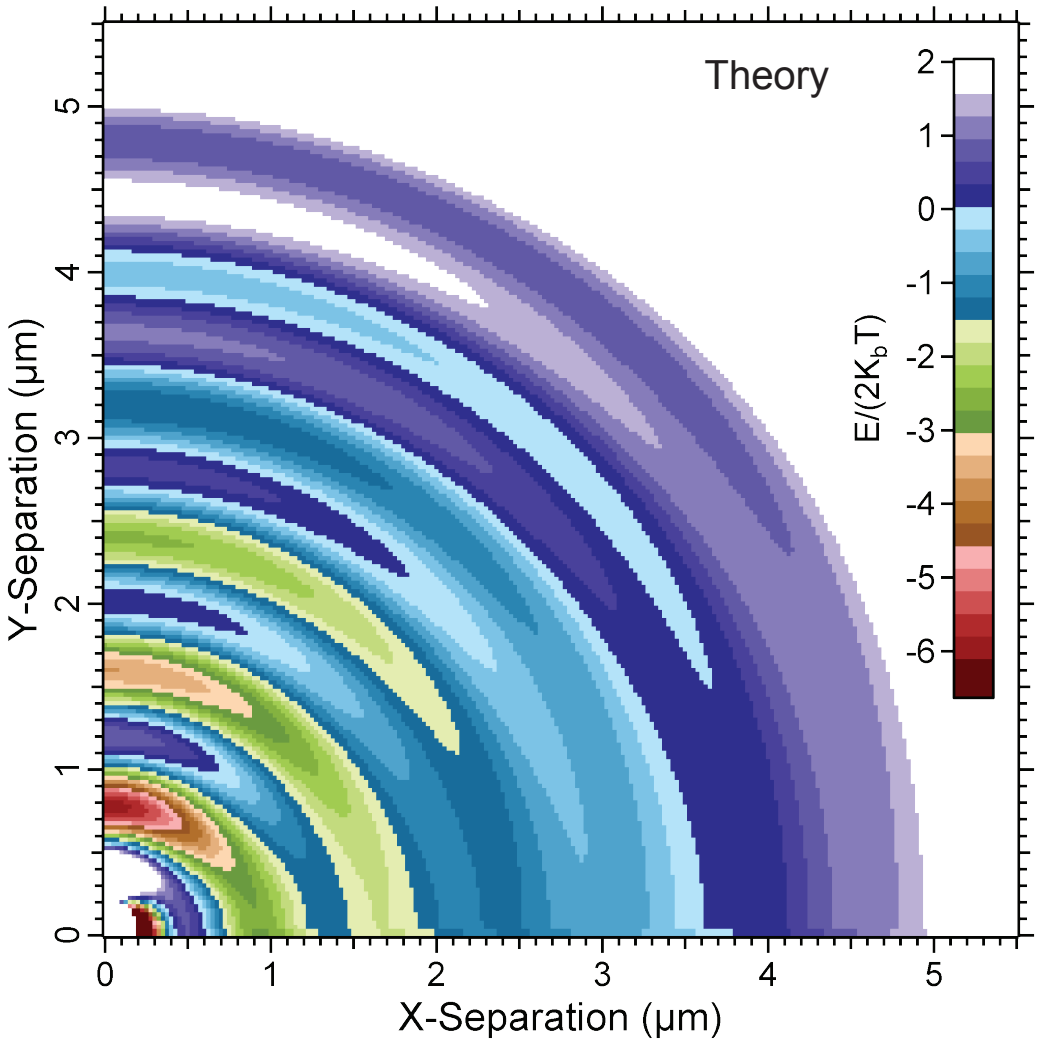

Figure 10.4: The theoretical optical binding energy landscape is calculated for two particles in the pancake trap under the same conditions as used in the experiment. The energy is normalized to the thermal energy of a two particle system. We can see excellent agreement with the experimental measurement shown in figure 10.3.

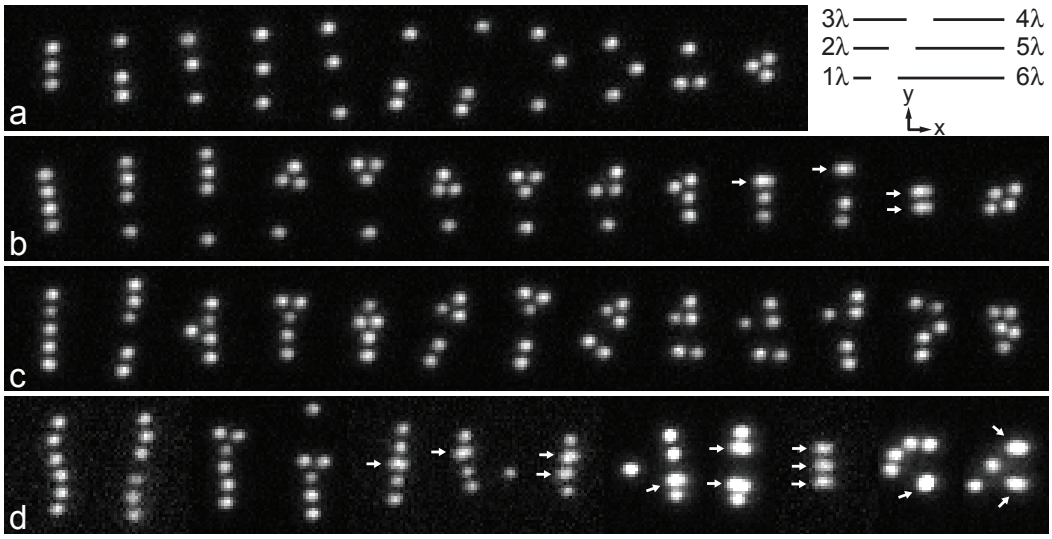

Figure 10.5: Optical matter formations in the pancake trap imaged using dark-field microscopy. Clusters containing exactly 3, 4, 5, and 6 particles are shown in rows a, b, c, and d respectively. Each row shows multiple images of the same number of particles. The most stable configurations seem to be those which are elongated perpendicular to the polarization axis (horizontal axis), such as the mainly linear conformations on the left-hand side. Particle pairs in contact are denoted with an arrow, and we note that these pairs only occur horizontally which is in agreement with theory (see figure 10.4).

the polarization axis is in agreement with the interaction potential shown in figures 10.3 and 10.4. We can also see that while inter-particle separation distances are roughly multiples of the laser wavelength ($\lambda = 800nm$ in water), some particles are actually in contact. This contact only occurs along the polarization axis, and is in agreement with theory which predicts that the near-field optical binding potential transitions from a repulsive force to an attractive force depending on the particle pair orientation [196, 240, 241] (figure 10.4). In addition, we note that there has been theoretical study of the formation of 2D

optical matter for both micrometer-scale particles and nano-scale (Rayleigh) particles [199]. Predictions of cluster geometries depend on the size of the particles, and our results shown in figure 10.5 are in agreement with those simulations for Rayleigh particles indicating our experimental measurements are clearly in the Rayleigh regime. We invite the reader to compare our images in figure 10.5 with those configurations predicted through simulation described in reference [199].

10.3 Geometry Dependent Cluster Motion

While the multi-body optical binding interaction between nanoparticles is seen to form complex arrangements of particles relative to each other, we also observe geometry specific coupling of the optically bound clusters with the external optical field of the pancake trap. We can track, for example, the center of mass (CoM) motion of the cluster as a simple reporter of the clusters behavior as a single entity. However, since the cluster motion is expected to be dominated by the sum of the optical gradient forces (as well as thermal forces) on each constituent particle rather than by inertia, we calculate an effective center of mass (eCoM) which weights each particles location proportionally to its polarizability (α) rather than its mass. The weighting for each constituent particle is easily determined since the polarizability is proportional to the square-root of the total scattered intensity. Additionally, the particles polarizability is also proportional to its volume (and therefore also its mass) meaning the CoM and eCoM should be identical calculations. Through this

tracking of the clusters eCoM, we can observe changes in cluster behavior depending on the cluster geometry. For example, in general we observe that as the number of particles in the cluster increases, the standard deviation of the eCoM fluctuations (due to thermal forces) decreases which indicates stronger confinement. This is expected, as more particles would collectively experience a stronger total optical gradient force.

However, while one might expect that the sum of the gradient forces on each constituent particle in the cluster would solely determine the average eCoM location in the optical field, our measurements contradict this expectation. For example, for a pair of identical particles trapped in a single plane in the pancake trap we would expect a completely axially symmetric system, and thus for any orientation of the pair the average eCoM position should not change. We can check this assumption in our measurements by keeping track of the identity of each particle (we label them as A and B) throughout the videos. Since the particle pairs prefer to align perpendicular to the polarization axis due to the optical binding interaction potential (see figures 10.3 and 10.4), we can separate the data into two groups: one where particle A is "on top" of particle B ($y_A > y_B$), and one where particle B is "on top" of particle A ($y_A < y_B$). In doing so, we find a surprising result (see figure 10.6) in that the entire cluster shifts several microns to a new position in the 2D trapping volume depending on which particle is "on top" (the specific ordering of the particles). We know that the particles used in the experiments cannot be exactly identical, and there must be some differences, most likely in their

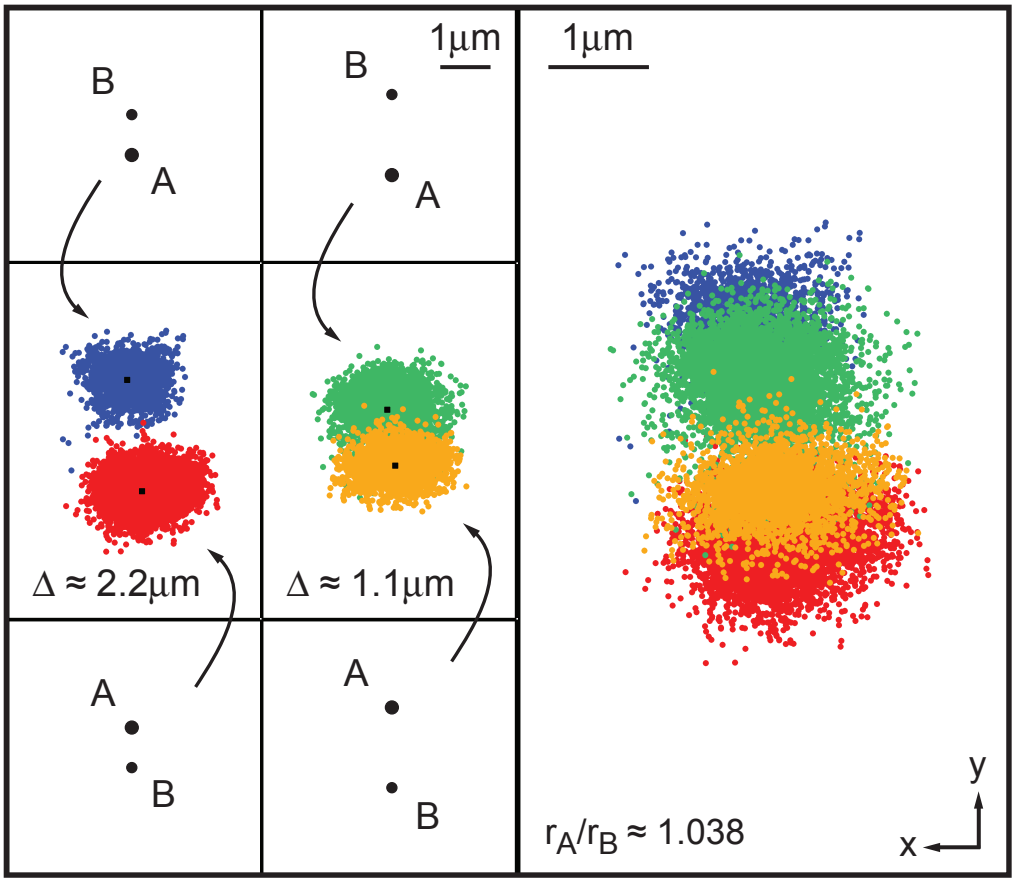

Figure 10.6: Center of mass tracking of an optically bound particle pair in the pancake trap. The colored regions represent the set of measured locations of the center of mass of the particle pair (which thermally diffuses within the pancake trap) for a given arrangement and orientation. The black squares represent the average center of mass position of the regions. The black dots in the top and bottom panels represent the arrangements of the gold nanoparticles (drawn to scale) and the arrows indicate the center of mass regions corresponding to those particle arrangements. The average center of mass position is seen to shift depending on the order of the particles, likely due to a difference (3.8%) in particle diameter. The larger particle is marked as A, and the smaller as B. This effect indicates a coupling to the external optical field that is specific to the particle formation. The panel on the right overlays all the sets of center of mass positions and is scaled by a factor of 2.

shapes and sizes, which cause the observed asymmetry. While it is not possible to measure the details of the particles' surface landscapes in diffraction limited optical microscopy, their relative sizes can be estimated by measuring the total scattered light intensity of each particle (I_i). Assuming the particles are approximately spherical, the total scattered intensity is proportional to the radius (r_i) of the particle by $I_i \propto r_i^6$ and thus even a small difference in radius should yield a measureable intensity difference. We find that the ratio of the particle intensities is $I_A/I_B \approx 1.25$ which indicates the relative sizes of the particles to be $r_A/r_B \approx 1.04$. Although this is only a 4% difference in size between the two particle, the cluster always dramatically translates in the direction of the smaller particle (figure 10.6). It may be that there is some small effect due to the calculation of the eCoM since the brighter particle is weighted more heavily, however such an effect would only cause a shift toward the larger particle and would be much less than the distance between the two particles, whereas we observe the opposite of both of these effects in our measurements. In fact, when the particles are in the first binding position (separated by $R \approx \lambda = 0.80\mu m$) we see a translation of about $2.2\mu m$ between the average positions of the eCoMs. This is a shift of over 275% of the distance between the two particles for only a 4% difference in size. When we calculate the eCoM for each particle ordering when the particle pair separation is doubled ($R \approx 2\lambda = 1.60\mu m$) we find that the shift in average eCoM position between the two configurations decreases by half to about $1.1\mu m$. This reduction in the eCoM shift may be due to a stronger gradient force since the greater

separation between the particles causes them to be nearer to the edges of the trapping volume. If this were true, we would also expect that the stronger gradient forces would reduce the standard deviation of the thermal fluctuations of the pair, but we find no significant change in those measurements. It is then likely that the distance between the particles, in addition to the particle size and ordering, plays a strong role in the coupling of the optically bound cluster to the external field. It is likely that when the particles are in closer proximity, they couple more strongly to each other and their specific interaction with the external field becomes more pronounced.

Similarly, as more particles are added to the cluster thus allowing a variety of geometrical arrangements (figure 10.5), we find that different cluster geometries also exhibit strong shifts in eCoM location. Furthermore, we now also see changes in the shape of the area it may explore. Figures 10.7 and 10.8 show different cluster configurations along with the corresponding regions explored by the eCoM through thermal motion of the cluster in the pancake trap. We see that for even small differences in geometry can cause the entire cluster to shift to a different region of the trapping volume. This shift is also dependent on the orientation of the cluster, as seen in the 1^{st} and 2^{nd} columns of the second row of figure 10.7 as well as in figure 10.6. Since the clusters prefer to align with their long axis perpendicular to the polarization direction, cluster generally do not rotate. However, the 4^{th} column from the left of figure 10.8a depicts a small triangular formation which was seen to rotate much more freely due to its symmetry. Thus the region which is explored by the cluster

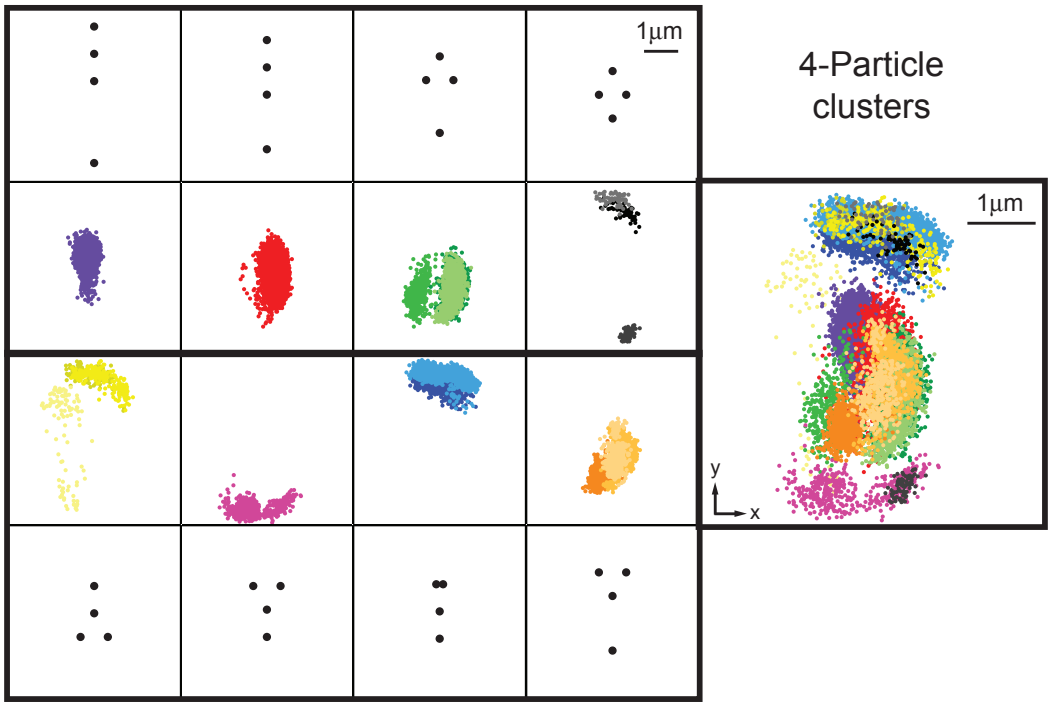

Figure 10.7: Center of mass tracking of 4-particle optical matter formations within the pancake trap. For different arrangements of the gold nanoparticles, the center of mass of the cluster shifts to different locations in the PT indicating geometry specific coupling to the external optical field. The black dots represent the arrangements of the gold nanoparticles (drawn to scale) and the colored shaded regions represent the set of center of mass locations for each given arrangement. Plotted above or below each cluster diagram are the corresponding sets of measured center of mass positions. In some plots, multiple colors are used indicating separate portions of the analyzed video where the formation occurred. We distinguish the separate occurrences because it is possible for the same geometry to reoccur while the specific order of the particles may have changed (as in the two particle case shown in figure 10.6). The panel on the far right overlays all the center of mass regions observed for comparison and is scaled by a factor of 2.

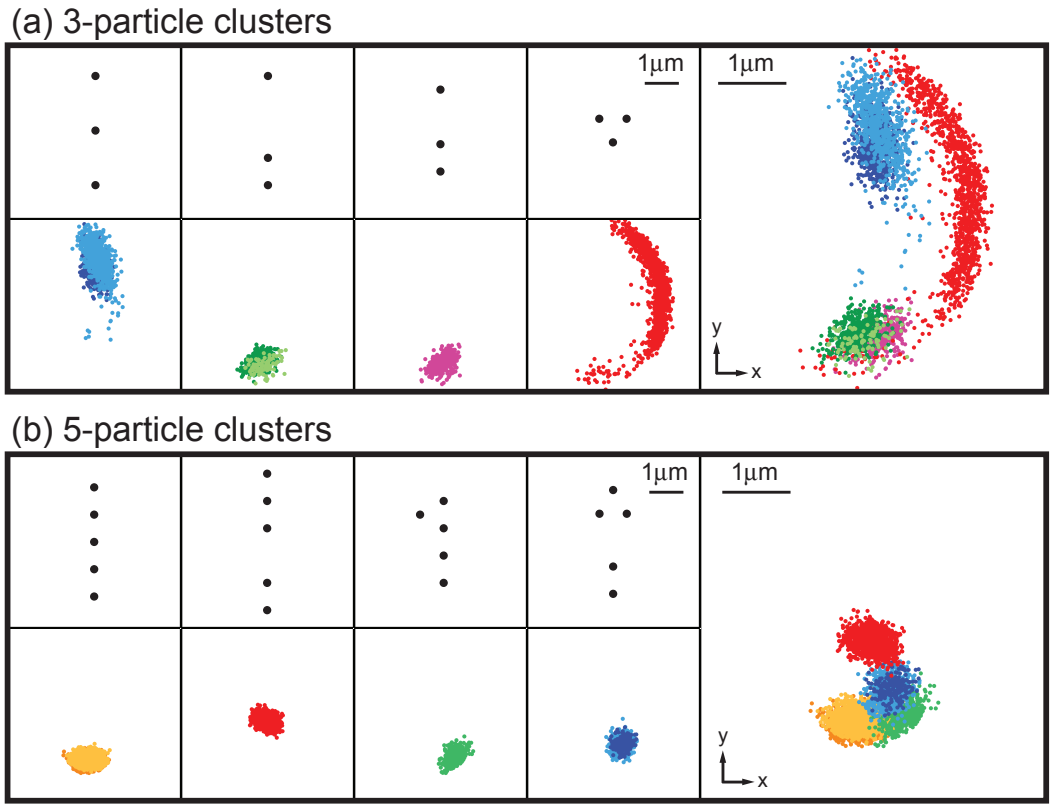

Figure 10.8: Center of mass tracking of 3- or 5-particle optical matter formations within the pancake trap. See figure caption 10.7 for more details.

sweeps a broad region as it rotates.

In general, these regions are specific to the cluster geometry and orientation, and the cluster will always return to the same region when in a particular configuration. We observe exceptions to this rule in a few instances, such as shown in figure 10.7. This is likely because the specific constituent particles within the cluster have rearranged, and since they are likely have small differences in size or shape, this reordering of the particles can cause large shifts

in eCoM location as demonstrated for the 2 particle system (figure 10.6). For example, the 3^{rd} and 4^{th} columns of the top row of figure 10.7 show that for the same cluster configuration, an eCoM region can have a "mirror image" region which is likely due to the cluster reforming as its own "mirror image" of constituent particles about the same axis.

These results showing strong geometry dependent coupling with the external optical field are particularly interesting and quite dramatic. While there has been a strong focus in the optics and nanotechnology communities on plasmonic devices, typical plasmonic coupling between nanoparticles occures at distances far smaller than the excitation wavelength (on the order of 10s of nanometers). This coupling of particles over the long distances of many wavelengths and the subsequent coupling and interaction of the clusters with external optical fields may provide a new frontier for optical nano-device development.

10.4 Summary

I described how the pancake trap can be used to study the optical binding interaction between nanoparticles in two dimensions. The high trapping stability of the pancake trap was used to trap a pair of $200nm$ gold particles in a single plane for 3 hours. Thus enough statistics of particle positions could be gathered in order to accurately and quantitatively measure the optical binding interaction in 2D. I provide the first detailed quantitative measurement of the pairwise optical binding energy landscape between nanoparticles in 2D. These

measurements show excellent agreement with theoretical calculations of the energy landscape.

When multiple particles are trapped, they are observed to self-assemble into a variety of geometrical shapes due to the optical binding interaction. These configurations are the first experimental observations of self-assembled "optical matter" in 2D using only optical binding forces and are in agreement with theoretical predictions made by other researchers. The center of mass motion of these clusters was then tracked and it was observed that the clusters move to different locations in the optical field depending on their specific geometries or particle order. This indicates that the positioning of the cluster within the optical field depends not only as the sum of the gradient forces on each constituent particle, but also depends on geometric properties of the cluster as a whole. This phenomenon has never before been observed.

Chapter 11

Outlook

We have shown that the optical binding force is a unique and powerful tool for manipulation of multiple nanoparticles. In addition, this ultra-strong, long-range interaction can be used to create complex rigid nanostructures with very high precision. With reasonably increased laser intensity and by using a laser wavelength near the plasmon resonance of the particles, precision of only a few nanometers or better should be achievable. Even particles $45nm$ in diameter or smaller should stably bind although with less precision (see chapter 9.4). We also expect that optical matter should become more stable as more particles are added. As we have indicated by our assisted trapping design (chapter 9.3), binding of smaller nanoparticles to form larger optical molecules should result in stable trapping of the object as a whole whereas the individual components may normally be difficult to trap.

There is vast potential for commercial application of optical matter. For example, metal particles or nanowires may be arranged precisely in 3D using optical binding then frozen in place within light-activated resin [140], thereby keeping the arrangement in a material for use in new electronics such as novel photovoltaics with broadband absorption [305–309] or high-precision

plasmonic nanodevices [4, 310]. Seeds or templates may be made for generating crystal structures or even biological tissue [196, 197]. New designs for nanomachines based on optical binding forces are now possible which can switch conformations or functions when illuminated by different wavelengths. When sensitivity to laser intensity is a concern, such as with biological experiments [236, 238, 239], optical binding provides the possibility for ultra-low power optical manipulation thereby extending the realm of potential medical research.

Appendices

Appendix A

List of Symbols and Variables

————English Letters————

a	.....	The radius of a spherical particle. Sometimes the symbol r is also used.
A, B	.....	Lables for the two individual particles of an optically bound particle pair.
$\overline{AB}$	.....	The length of the direct path a scattered light ray travels between two optically bound particles.
$\overline{AB'}$	.....	The length of the singly reflected path (off a surface) a scattered light ray travels between two optically bound particles.
c	.....	Speed of light in vacuum ($c = 3.0 \times 10^8 \frac{m}{s}$).
D	.....	The diameter of the objective lens back aperture.
D_f	.....	The diameter of the objective lens front aperture.
$\|E_0\|$	.....	The amplitude of the electric field vector of in an optical field.
f	.....	The focal length of a lens (usually the objective front lens).

f_b ..... The focal length of the back lens of an objective lens system.

F ..... Force (typically an optical force).

I_0 ..... The peak intensity of a 2D Gaussian distributed intensity profile. The location of this peak intensity generally defines the origin $(0, 0)$ of the coordinate system used.

$I_{x,y}$ ..... The intesity distribution of an optical field in a given 2D plane (typically the sample plane).

k ..... The wavenumber of a light wave. Related to the wavelength of light by $k = 2\pi/\lambda$.

k_B ..... Boltzmann's constant ($1.38 \times 10^{-23} \frac{m^2 kg}{K s^2}$).

L ..... The luminosity of a radiating object. The luminosity of the sun is $L_{sun} = 3.85 \times 10^{26}\, W$

n_m ..... The refractive index of a medium. Usually this medium surrounds the particles being studied (and is typically water, $n_m = 1.33$).

n_p ..... The refractive index of a particle. Typically polystyrene ($n_p = 1.55$) or gold ($n_p = -26.18 + i1.85$) is used. We must note that the complex refractive index of gold is wavelength dependent, and it is important to look up the exact value in reference [203].

NA ..... The numerical aperture of the objective lens.

p ..... The force per unit area (pressure) on an object.

P ..... The total laser power measured in the sample plane.

r ..... The radius of a spherical object. Usually the symbol a is used instead.

R ..... The distance between a pair of particles, usually used to describe an optically bound particle pair.

$\vec{s}$ ..... Displacement vector along a given path of arbitrary geometry.

T ..... Temperature of the sample (usually room temperature: $T \approx 295K$).

U ..... Potential energy function for a given system.

$\vec{v}$ ..... Velocity of a particle.

W ..... Probability function for a given system.

————Greek Letters————

α ..... The effective complex polarizability of a particle including the radiative reaction correction to the Claussius-Mossotti relation.

α_0 ..... The complex polarizability of a particle given by the Claussius-Mossotti relation (no radiative reaction correction).

β ..... A fitting parameter used to fit the optical binding spring constant data shown in figure 9.7. $\beta = \frac{|\alpha|^2 |E_0|^2 k^5 \sin^2\theta}{8\pi\epsilon_0\epsilon_m}$

γ ..... Stokes drag coefficient. Related to the particle radius (a) and fluid viscosity (η) by $\gamma = 6\pi\eta a$.

δx_{CL} ..... The displacement of the cylinder lens focal line in the SWOLT setup relative to the optical axis.

δz_{CL} ..... The displacement of the cylinder lens focal line in the SWOLT setup relative to the back focal plane of the objective lens.

Δ_x ..... The x-component of displacement between two optically bound particles.

Δ_y ..... The y-component of displacement between two optically bound particles.

Δz ..... The displacement of the image plane from the focal plane. See chapter 4.2.

ϵ ..... Correction factor for the Stokes drag coefficient for motion near a surface. Generally takes on a value between 1 (in bulk solution far from surfaces) to 3 (very near a surface). See reference [195] for more details

ϵ_0 ..... The dielectric permeability of vacuum ($\epsilon_0 = 8.85^{-12} \frac{s^2 C^2}{m^3 kg}$).

ϵ_m ..... The dielectric constant a medium. Generally this is the medium surrounding the particles being studied (and is typically water, $\epsilon_m = 1.77$). It is related to the refractive index by $\epsilon_m \approx n_m^2$ assuming the magnetic permiability of the material is 1.

ϵ_p ..... The dielectric constant of the particle(s) studied. It is related to the refractive index by $\epsilon_m \approx n_m^2$ assuming the magnetic permiability of the material is 1.

η ..... The fluid viscocity. For water, it is known to be $\eta = 1.0 fNs/\mu m^2$.

θ ..... 1) The angle of incidence of a light ray off a reflecting surface. 2) The angle of polarization of the incident light field relative to the axis joining two particles (as for an optically bound particle pair).

κ ..... The spring constant of a harmonic oscillator. Used to describe the strength of an optical trap.

λ ..... The wavelength of a light wave in a medium of refractive index n_m.

λ_0 ..... The wavelength of a light wave in vacuum.

ξ ..... The trapping efficiency of an optical trapping system. Defined as $\xi \equiv \kappa/I$.

π ..... The irrational number ($\pi = 3.1415926535\ldots$).

σ ..... The width of a Gaussian distribution or function.

τ ..... Position autocorrelation time. The characteristic timescale for a Brownian oscillator to traverse a harmonic potential energy well. $\tau = \gamma/\kappa$

ϕ ..... The angle made by the scattered light ray which travels along the path $\overline{AB'}$ with respect to the direct path $\overline{AB}$ (or equivalently to the plane of the reflecting surface).

Appendix B

List of Equations

The optical scattering force on a Rayleigh particle:

$$F^s(\vec{x}) = \frac{8\pi^3\alpha^2}{3cn_m^3\epsilon_0^2\lambda^4} I(\vec{x}) \tag{B.1}$$

$$= \frac{128\pi^5 a^6 n_m}{3c\lambda^4} \left[\frac{(n_p/n_m)^2 - 1}{(n_p/n_m)^2 + 2}\right]^2 I(\vec{x}) \tag{B.2}$$

The optical gradient force on a Rayleigh particle:

$$\vec{F}^g(\vec{x}) = \frac{1}{4}\alpha\nabla|E(\vec{x})|^2 \tag{B.3}$$

$$= \frac{2\pi n_m a^3}{c} \left[\frac{(n_p/n_m)^2 - 1}{(n_p/n_m)^2 + 2}\right] \nabla I(\vec{x}) \tag{B.4}$$

The optical binding force on a Rayleigh particle (in cylindrical coordinates):

$$F_r^b = \frac{|\alpha|^2|E_0|^2}{8\pi\epsilon_0\epsilon_m R^4} \Big\{ \left[2k^2R^2\left(2\cos^2\theta - 1\right) + 3\left(1 - 3\cos^2\theta\right)\right]\cos(kR) + \left[k^3R^3\left(\cos^2\theta - 1\right) + 3kR\left(1 - 3\cos^2\theta\right)\right]\sin(kR) \Big\} \tag{B.5}$$

$$F_\theta^b = \frac{|\alpha|^2|E_0|^2}{8\pi\epsilon_0\epsilon_m R^4} \sin(2\theta)\left[\left(k^2R^2 - 3\right)\cos(kR) - 3kR\sin(kR)\right] \tag{B.6}$$

$$F_z^b = -\Re\left\{\frac{(\alpha^*)^2|E_0|^2 k e^{-ikR}}{8\pi\epsilon_0\epsilon_m R^3} \times \left[3i - 3kR - ik^2R^2\right]\sin^2\phi - 2i + 2kR\right\} \tag{B.7}$$

The intensity distribution for a point focused laser beam:

$$I(x,y,z) = \frac{2P}{\pi}\left[\frac{1}{\omega_0^2 + 4z^2}\right] e^{-\frac{2(x^2+y^2)}{\omega_0^2+4z^2}} \tag{B.8}$$

The relationship between the intensity and electric field amplitude:

$$I(\vec{x}) = \frac{cn_m\epsilon_0}{2}|E(\vec{x})|^2 \tag{B.9}$$

The radius of the beam waist for a diffraction limited focal spot:

$$\omega_0 = \frac{\lambda}{2NA} \tag{B.10}$$

The Clausius-Mossotti relation:

$$\alpha = \frac{\alpha_0}{1 - \frac{ik^3\alpha_0}{6\pi\epsilon_0\epsilon_m}} \tag{B.11}$$

$$\alpha_0 = 4\pi\epsilon_0\epsilon_m a^3\left[\frac{\epsilon_p - \epsilon_m}{\epsilon_p + 2\epsilon_m}\right] \tag{B.12}$$

The Stokes drag on a particle moving in fluid:

$$\vec{F}^d = -6\pi\epsilon\eta a\vec{v} \tag{B.13}$$

The Maxwell-Boltzmann probability distribution for energy states:

$$W(\vec{x}) = \frac{1}{Z}e^{\frac{-U(\vec{x})}{k_B T}} \tag{B.14}$$

The position autocorrelation time:

$$\tau = \frac{\gamma}{\kappa_N} = \frac{6\pi\eta a}{\kappa_N} \tag{B.15}$$

Radiation pressure due to a point source emitter:

$$p = \frac{L}{4\pi r^2 c} \tag{B.16}$$

Bibliography

[1] T. H. Maiman. Stimulated optical radiation in ruby. *Nature*, 187(4736):493–494, August 1960.

[2] CJ Barrelet, AB Greytak, and CM Lieber. Nanowire photonic circuit elements. *Nano Letters*, 59:1–5, 2004.

[3] Mo Li, W H P Pernice, C Xiong, T Baehr-Jones, M Hochberg, and H X Tang. Harnessing optical forces in integrated photonic circuits. *Nature*, 456(7221):480–4, November 2008.

[4] WL Barnes, Alain Dereux, and TW Ebbesen. Surface plasmon subwavelength optics. *Nature*, 424(August):824–831, 2003.

[5] Mark Haw. Holographic data storage: The light fantastic. *Nature*, 422(4):80–5, April 2003.

[6] L Dhar, K Curtis, and T Fäcke. Holographic data storage: Coming of age. *Nature Photonics*, 2(July):403–405, 2008.

[7] Ji Cirac and P Zoller. A scalable quantum computer with ions in an array of microtraps. *Nature*, 404(6778):579–81, April 2000.

[8] Daniel Gottesman and IL Chuang. Demonstrating the viability of universal quantum computation using teleportation and single-qubit operations. *Nature*, 402(11), November 1999.

[9] E Knill, R Laflamme, and G J Milburn. A scheme for efficient quantum computation with linear optics. *Nature*, 409(6816):46–52, January 2001.

[10] J L O'Brien, G J Pryde, A G White, T C Ralph, and D Branning. Demonstration of an all-optical quantum controlled-NOT gate. *Nature*, 426(6964):264–7, November 2003.

[11] T D Ladd, F Jelezko, R Laflamme, Y Nakamura, C Monroe, and J L O'Brien. Quantum computers. *Nature*, 464(7285):45–53, March 2010.

[12] P Walther, K J Resch, T Rudolph, E Schenck, H Weinfurter, V Vedral, M Aspelmeyer, and A Zeilinger. Experimental one-way quantum computing. *Nature*, 434(7030):169–76, March 2005.

[13] Johannes Kepler. Ad Vitellionem Paralipomena. *Frankfurt: Marinium and Aubrii*, 1604.

[14] Johannes Kepler. *De cometis libelli tres...* 1619.

[15] Joseph a. Burns, Philippe L. Lamy, and Steven Soter. Radiation forces on small particles in the solar system. *Icarus*, 40(1):1–48, October 1979.

[16] Hiroshi Kimura, Hajime Okamoto, and Tadashi Mukai. Radiation Pressure and the PoyntingRobertson Effect for Fluffy Dust Particles. *Icarus*, 157(2):349–361, June 2002.

[17] Bernd Dachwald. Optimal solar-sail trajectories for missions to the outer solar system. *Journal of Guidance, Control, and Dynamics*, (August), August 2005.

[18] LO Froideval. *A study of solar radiation pressure acting on GPS satellites*. PhD thesis, The University of Texas at Austin, 2009.

[19] Y Bar-Sever and D Kuang. New Empirically Derived Solar Radiation Pressure Model for Global Positioning System Satellites During Eclipse Seasons. *IPN Progress Report*, 42(160):1–4, 2005.

[20] R M Georgevic. Solar radiation pressure effects on the Helios spacecraft. *NASA STI/Recon Technical Report N*, July 1976.

[21] R M Georgevic. The Solar Radiation Pressure on the Mariner 9 Mars Orbiter. *NASA STI/Recon Technical Report N*, December 1972.

[22] R M Georgevic. Mathematical model of the solar radiation force and torques acting on the components of a spacecraft. *NASA STI/Recon Technical Report N*, October 1971.

[23] SN Singh and W Yim. Nonlinear adaptive backstepping design for spacecraft attitude control using solar radiation pressure. *Proceedings of the 41st IEEE*, (December):1239–1244, 2002.

[24] John D Anderson, Philip A Laing, Eunice L. Lau, Anthony S Liu, Michael Martin Nieto, and Slava. Study of the anomalous acceleration of Pioneer 10 and 11. *Physical Review D*, 65:082004, April 2002.

[25] Slava G. Turyshev, Viktor T. Toth, Larry R. Kellogg, Eunice L. Lau, and Kyong J. Lee. The study of the pioneer anomaly: new data and objectives for new investigation. *International Journal of Modern Physics D*, 15(01):1–55, 2006.

[26] R M Georgevic. The solar radiation pressure force and torques model. *Journal of the Astronautical Sciences*, 20:257—-274, 1973.

[27] V. Koblik, E. Polyakhova, and L. Sokolov. Solar sail near the Sun: Point-like and extended models of radiation source. *Advances in Space Research*, 48(11):1717–1739, December 2011.

[28] L. Rios-Reyes and D. J. Scheeres. Generalized Model for Solar Sails. *Journal of Spacecraft and Rockets*, 42(1):182–185, January 2005.

[29] M Leipold. To the sun and Pluto with solar sails and micro-sciencecraft. *Acta Astronautica*, 45:549–555, 1999.

[30] James Clerk Maxwell. *A treatise on electricity and magnetism*. Oxford at the Clarendon Press, Oxford, 2nd edition, 1881.

[31] P Lebedew. Untersuchungen über die Druckkräfte des Lichtes. *Annalen der Physik*, 311(11):433–458, November 1901.

[32] Arthur Ashkin. Acceleration and trapping of particles by radiation pressure. *Physical Review Letters*, 24(4):156–159, January 1970.

[33] Arthur Ashkin and J M Dziedzic. Optical Levitation by Radiation Pressure. *Applied Physics Letters*, 19(8):283–285, October 1971.

[34] EM Purcell and CR Pennypacker. Scattering and absorption of light by nonspherical dielectric grains. *The Astrophysical Journal*, 186:705–714, December 1973.

[35] J. P. Gordon and Arthur Ashkin. Motion of atoms in a radiation trap. *Physical Review A*, 21(5):1606–1617, May 1980.

[36] P W Smith, Arthur Ashkin, and W J Tomlinson. Four-wave mixing in an artificial Kerr medium. *Optics Letters*, 6(6):284–286, June 1981.

[37] Arthur Ashkin, J M Dziedzic, and P W Smith. Continuous-wave self-focusing and self-trapping of light in artificial Kerr media. *Optics Letters*, 7(6):276–278, June 1982.

[38] Steven Chu, JE Bjorkholm, Arthur Ashkin, and A. Cable. Experimental observation of optically trapped atoms. *Physical Review Letters*, 57(3):314–317, July 1986.

[39] B.T. Draine. The discrete-dipole approximation and its application to interstellar graphite grains. *The Astrophysical Journal*, 333:848–872, October 1988.

[40] J. P. Barton, D. R. Alexander, and S. A. Schaub. Theoretical determination of net radiation force and torque for a spherical particle illuminated

by a focused laser beam. *Journal of Applied Physics*, 66(10):4594–4602, July 1989.

[41] Y Harada. Radiation forces on a dielectric sphere in the Rayleigh scattering regime. *Optics Communications*, 124:529–541, March 1996.

[42] Shojiro Nemoto and H Togo. Axial force acting on a dielectric sphere in a focused laser beam. *Applied Optics*, 37(27):6386–6394, September 1998.

[43] Adrian Neild, Tuck Wah Ng, and Winston Ming Shen Yii. Optical sorting of dielectric Rayleigh spherical particles with scattering and standing waves. *Optics express*, 17(7):5321–9, March 2009.

[44] Arthur Ashkin, J M Dziedzic, JE Bjorkholm, and Steven Chu. Observation of a single-beam gradient force optical trap for dielectric particles. *Optics Letters*, 11(5):288–290, May 1986.

[45] Rachel Won and Arthur Ashkin. How It All Began. *Nature Photonics*, 5(6):316–317, June 2011.

[46] Arthur Ashkin and J M Dziedzic. Optical trapping and manipulation of viruses and bacteria. *Science*, 235(4795):1517–1520, March 1987.

[47] Arthur Ashkin, J M Dziedzic, and T. Yamane. Optical trapping and manipulation of single cells using infrared laser beams. *Nature*, 330:769–771, December 1987.

[48] Karel Svoboda and Steven M. Block. Optical trapping of metallic Rayleigh particles. *Optics Letters*, 19(13):930–932, July 1994.

[49] H Furukawa and I Yamaguchi. Optical trapping of metallic particles by a fixed Gaussian beam. *Optics Letters*, 23(3):216–218, February 1998.

[50] Pu Chun Ke and Min Gu. Characterization of trapping force in the presence of spherical aberration. *Journal of Modern Optics*, 45(10):2159–2168, October 1998.

[51] S Nader S Reihani, H Khalesifard, and R Golestanian. Measuring lateral efficiency of optical traps: The effect of tube length. *Optics Communications*, 259:204–211, March 2006.

[52] Lana Bosanac, Thomas Aabo, Poul M Bendix, and Lene B Oddershede. Efficient optical trapping and visualization of silver nanoparticles. *Nano Letters*, 8(5):1486–1491, May 2008.

[53] Christine Selhuber-unkel, Inga Zins, Olaf Schubert, Carsten So, Carsten Sönnichsen, and Lene B Oddershede. Quantitative optical trapping of single gold nanorods. *Nano letters*, 8(9):2998–3003, September 2008.

[54] Lin Ling, Fei Zhou, Lu Huang, and Zhi-Yuan Li. Optical forces on arbitrary shaped particles in optical tweezers. *Journal of Applied Physics*, 108(7):073110, October 2010.

[55] Vladlen G Shvedov, Andrei V Rode, Yana Izdebskaya, Anton Desyatnikov, Wieslaw Krolikowski, and Yuri Kivshar. Giant Optical Manipulation. *Physical Review Letters*, 105(11):118103, September 2010.

[56] Jesper Gluckstad. Optical manipulation: Sculpting the object. *Nature Photonics*, 5(1):7–8, January 2011.

[57] Mohammed Mahamdeh, Citlali Perez Campos, and Erik Schaffer. Underfilling trapping objectives optimizes the use of the available laser power in optical tweezers. *Optics Express*, 19(12):1260–1262, June 2011.

[58] Ali Mahmoudi and S Nader S Reihani. The effect of immersion oil in optical tweezers. *Optics Express*, 19(16):388–394, August 2011.

[59] Akbar Samadi and S Nader S Reihani. Role of condenser iris in optical tweezer detection system. *Optics Letters*, 36(20):4056–4058, October 2011.

[60] Zijie Yan, Justin E Jureller, Julian Sweet, Mason J Guffey, Matthew Pelton, and Norbert F. Scherer. Three-Dimensional Optical Trapping and Manipulation of Single Silver Nanowires. *Nano letters*, September 2012.

[61] Arthur Ashkin. Forces of a single-beam gradient laser trap on a dielectric sphere in the ray optics regime. *Biophysical Journal*, 61(February):569–582, January 1992.

[62] Peter L Freddolino, Anton S Arkhipov, Steven B Larson, Alexander Mcpherson, and Klaus Schulten. Molecular dynamics simulations of the complete satellite tobacco mosaic virus. *Structure*, 14(3):437–449, March 2006.

[63] Steven M. Block, David F. Blair, and Howard C. Berg. Compliance of bacterial flagella measured with optical tweezers. *Nature*, 338:514–518, April 1989.

[64] S Seeger, S Monajembashi, K J Hutter, G Futterman, J Wolfrum, and K O Greulich. Application of laser optical tweezers in immunology and molecular genetics. *Cytometry*, 12(6):497–504, January 1991.

[65] Rosemarie Wiegand Steubing, Steve Cheng, William H Wright, Yasuyuki Numajiri, and Michael W. Berns. Laser induced cell fusion in combination with optical tweezers: the laser cell fusion trap. *Cytometry*, 510:505–510, 1991.

[66] I a Vorobjev, Hong Liang, William H Wright, and Michael W. Berns. Optical trapping for chromosome manipulation: a wavelength dependence of induced chromosome bridges. *Biophysical Journal*, 64(2):533–538, February 1993.

[67] Karel Svoboda and Steven M. Block. Biological applications of optical forces. *Annual review of biophysics and biomolecular structure*, 23:247–285, January 1994.

[68] PJ Bronkhorst, GJ Streekstra, J. Grimbergen, EJ Nijhof, JJ Sixma, and GJ Brakenhoff. A new method to study shape recovery of red blood cells using multiple optical trapping. *Biophysical Journal*, 69(5):1666–1673, November 1995.

[69] G. Leitz, E. Schnepf, and K O Greulich. Micromanipulation of statoliths in gravity-sensing Chara rhizoids by optical tweezers. *Planta*, 197(2):278–288, 1995.

[70] H Felgner, R Frank, and M Schliwa. Flexural rigidity of microtubules measured with the use of optical tweezers. *Journal of Cell Science*, 109:509–516, February 1996.

[71] Hong Liang, KT Vu, Priya Krishnan, TC Trang, David Shin, S, S. Kimel, and Michael W. Berns. Wavelength dependence of cell cloning efficiency after optical trapping. *Biophysical journal*, 70(March):4–5, March 1996.

[72] A. D. Mehta. Single-Molecule Biomechanics with Optical Methods. *Science*, 283(5408):1689–1695, March 1999.

[73] J Guck, R Ananthakrishnan, H Mahmood, T J Moon, C C Cunningham, and J Käs. The optical stretcher: a novel laser tool to micromanipulate cells. *Biophysical Journal*, 81(2):767–784, August 2001.

[74] Thomas Schnelle, Peter Walden, Evotec Biosystems Ag, C Reichle, K Sparbier, Torsten Müller, and Gunter Fuhr. Combined laser tweezers and

dielectric field cage for the analysis of receptor-ligand interactions on single cells. *Electrophoresis*, 22(2):272–282, January 2001.

[75] Keir C Neuman and Steven M. Block. Optical trapping. *The Review of Scientific Instruments*, 75(9):2787–2809, September 2004.

[76] Pei Yu Chiou, Aaron T Ohta, and Ming C Wu. Massively parallel manipulation of single cells and microparticles using optical images. *Nature*, 436(7049):370–2, July 2005.

[77] Kishan Dholakia and Peter J Reece. Optical micromanipulation takes hold. *Nano today*, 1(1):18–27, 2006.

[78] Darren Segall, Philip Nelson, and Rob Phillips. Volume-Exclusion Effects in Tethered-Particle Experiments: Bead Size Matters. *Physical Review Letters*, 96(8):1–4, March 2006.

[79] Taejin L. Min, Patrick J. Mears, Lon M. Chubiz, Christopher V. Rao, Ido Golding, and Yann R Chemla. High-resolution, long-term characterization of bacterial motility using optical tweezers. *Nature Methods*, 6(11):831–835, November 2009.

[80] Ihab Sraj, Alex C Szatmary, David W M Marr, and Charles D Eggleton. Dynamic ray tracing for modeling optical cell manipulation. *Optics Express*, 18(16):16702–16714, August 2010.

[81] Ashis Gopal Banerjee, Sagar Chowdhury, Wolfgang Losert, and Satyandra K Gupta. Survey on indirect optical manipulation of cells, nucleic

acids, and motor proteins. *Journal of Biomedical Optics*, 16(5):051302, May 2011.

[82] Poul M Bendix and Lene B Oddershede. Expanding the optical trapping range of lipid vesicles to the nanoscale. *Nano Letters*, 11(12):5431–5437, December 2011.

[83] Aidan T. Brown, Jurij Kotar, and Pietro Cicuta. Active rheology of phospholipid vesicles. *Physical Review E*, 84(2):021930, August 2011.

[84] Matthew J Comstock, Taekjip Ha, and Yann R Chemla. Ultrahigh-resolution optical trap with single-fluorophore sensitivity. *Nature Methods*, 8:335–340, February 2011.

[85] Furqan M Fazal and Steven M. Block. Optical tweezers study life under tension. *Nature Photonics*, 5(6):318–321, May 2011.

[86] Jan Lipfert, Jacob J. W. Kerssemakers, Maylon Rojer, and Nynke H. Dekker. A method to track rotational motion for use in single-molecule biophysics. *Review of Scientific Instruments*, 82(10):103707, October 2011.

[87] Yuquan Zhang, Xin Wang, Yijia Wang, Siwei Zhu, Bruce Z Gao, and X.-C. Yuan. A simple dynamic optical manipulation technique for label-free detection of biological cells. *Review of Scientific Instruments*, 82(6):064301, June 2011.

[88] Pavel Zemanek, Alexandr Jonáš, L Šrámek, and Miroslav Liška. Optical trapping of Rayleigh particles using a Gaussian standing wave. *Optics communications*, 151(June):273–285, June 1998.

[89] Pavel Zemanek, Alexandr Jonáš, L Srámek, and Miroslav Liska. Optical trapping of nanoparticles and microparticles by a Gaussian standing wave. *Optics Letters*, 24(21):1448–1450, November 1999.

[90] Alexandr Jonáš, Pavel Zemanek, and Ernst-ludwig Florin. Single-beam trapping in front of reflective surfaces. *Optics Letters*, 26(19):1466–1468, October 2001.

[91] Petr Jakl, Alexandr Jonáš, Ernst-ludwig Florin, and Pavel Zemanek. Comparison of the single beam and the standing wave trap stiffnesses. *Proceedings of SPIE*, 4356:347–352, 2001.

[92] Pavel Zemanek and Alexandr Jonáš. Simplified description of optical forces acting on a nanoparticle in the Gaussian standing wave. *Journal of the Optical Society of America A*, 19(5):1025–1034, May 2002.

[93] Pavel Zemanek, Alexandr Jonáš, Petr Jakl, Jan Jezek, Mojmír Šerý, and Miroslav Liska. Theoretical comparison of optical traps created by standing wave and single beam. *Optics Communications*, 220:401–412, May 2003.

[94] Hideki Fujiwara, Hidehisa Takasaki, Jun-ichi Hotta, and Keiji Sasaki. Observation of the discrete transition of optically trapped particle posi-

tion in the vicinity of an interface. *Applied Physics Letters*, 84(1):13–15, January 2004.

[95] Matthias Reuss. *Optical trapping and manipulation of nanoparticles in a Gaussian standing wave*. PhD thesis, University of Texas at Austin, 2005.

[96] Satoshi Kawata and Tadao Sugiura. Movement of micrometer-sized particles in the evanescent field of a laser beam. *Optics Letters*, 17(11):772–774, June 1992.

[97] J Y Walz. Ray optics calculation of the radiation forces exerted on a dielectric sphere in an evanescent field. *Applied Optics*, 38(25):5319–5330, September 1999.

[98] Patrick C. Chaumet and Manuel Nieto-Vesperinas. Time-averaged total force on a dipolar sphere in an electromagnetic field. *Optics Letters*, 25(15):1065–1067, August 2000.

[99] L Ng. Propulsion of gold nanoparticles on optical waveguides. *Optics Communications*, 208:117–124, July 2002.

[100] Maria Dienerowitz, Michael Mazilu, and Kishan Dholakia. Optical manipulation of nanoparticles: a review. *Journal of Nanophotonics*, 2:021875, September 2008.

[101] Mason J Guffey, Ryan L Miller, Stephen K Gray, and Norbert F. Scherer. Plasmon-driven selective deposition of au bipyramidal nanoparticles. *Nano Letters*, 11(10):4058–4066, October 2011.

[102] M Ploschner, Tomas Cizmar, M. Mazilu, a Di Falco, and Kishan Dholakia. Bidirectional optical sorting of gold nanoparticles. *Nano letters*, 12(4):1923–7, April 2012.

[103] K Sasaki, M Koshioka, H Misawa, N Kitamura, and H Masuhara. Pattern formation and flow control of fine particles by laser-scanning micromanipulation. *Optics Letters*, 16(19):1463–1465, October 1991.

[104] Luc P. Faucheux, LS Bourdieu, PD Kaplan, and AJ Libchaber. Optical thermal ratchet. *Physical review letters*, 74(9):1504–1507, February 1995.

[105] Luc P. Faucheux, Gustavo Stolovitzky, and Albert Libchaber. Periodic forcing of a Brownian particle. *Physical Review E*, 51(6):5239–5250, June 1995.

[106] John C. Crocker, J. A. Matteo, A. D. Dinsmore, and A. G. Yodh. Entropic Attraction and Repulsion in Binary Colloids Probed with a Line Optical Tweezer. *Physical Review Letters*, 82(21):4352–4355, May 1999.

[107] C. Mio, T. Gong, Alex Terray, and David W M Marr. Design of a scanning laser optical trap for multiparticle manipulation. *Review of Scientific Instruments*, 71(5):2196–2200, May 2000.

[108] Rajalakshmi Nambiar and Jens-Christian Meiners. Fast position measurements with scanning line optical tweezers. *Optics Letters*, 27(10):836–838, May 2002.

[109] B. Liesfeld, Rajalakshmi Nambiar, and Jens-Christian Meiners. Particle transport in asymmetric scanning-line optical tweezers. *Physical Review E*, 68(5):051907, November 2003.

[110] Rajalakshmi Nambiar, Arivalagan Gajraj, and Jens-Christian Meiners. All-optical constant-force laser tweezers. *Biophysical Journal*, 87(3):1972–1980, September 2004.

[111] Paul L. Biancaniello and John C. Crocker. Line optical tweezers instrument for measuring nanoscale interactions and kinetics. *Review of Scientific Instruments*, 77(11):113702, November 2006.

[112] Graham Milne, Daniel Rhodes, Michael P MacDonald, and Kishan Dholakia. Fractionation of polydisperse colloid with acousto-optically generated potential energy landscapes. *Optics letters*, 32(9):1144–6, May 2007.

[113] Kishan Dholakia and Tomas Cizmar. Shaping the future of manipulation. *Nature Photonics*, 5(6):335–342, June 2011.

[114] Yoshio Tanaka, Shogo Tsutsui, Mitsuru Ishikawa, and Hiroyuki Kitajima. Hybrid optical tweezers for dynamic micro-bead arrays. *Optics express*, 19(16):15445–51, August 2011.

[115] Michael M. Burns, Jean-Marc R. Fournier, and Jene A. Golovchenko. Optical binding. *Physical Review Letters*, 63(12):1233–1236, September 1989.

[116] Michael M. Burns, Jean-Marc R. Fournier, and Jene A. Golovchenko. Optical matter: crystallization and binding in intense optical fields. *Science*, 249(4970):749–754, August 1990.

[117] Raktim Dasgupta, Samarendra K. Mohanty, and Pradeep Kumar Gupta. Controlled rotation of biological microscopic objects using optical line tweezers. *Biotechnology Letters*, 25(19):1625–1628, 2003.

[118] Samarendra K. Mohanty, J Andrews, and Pradeep Kumar Gupta. Optical binding between dielectric particles. *Optics Express*, 12(12):2749–2756, June 2004.

[119] Ting Yu, Fook-chiong Cheong, and Chorng-Haur Sow. The manipulation and assembly of CuO nanorods with line optical tweezers. *Nanotechnology*, 15(12):1732–1736, November 2004.

[120] Samarendra K. Mohanty, Raktim Dasgupta, and Pradeep Kumar Gupta. Three-dimensional orientation of microscopic objects using combined elliptical and point optical tweezers. *Applied Physics B: Lasers and Optics*, 81(8):1063–1066, November 2005.

[121] Samarendra K. Mohanty, Mrinalini Sharma, Mitradas M Panicker, and Pradeep Kumar Gupta. Controlled induction, enhancement, and guid-

ance of neuronal growth cones by use of line optical tweezers. *Optics Letters*, 30(19):2596–2598, October 2005.

[122] Samarendra K. Mohanty and Pradeep Kumar Gupta. Transport of microscopic objects using asymmetric transverse optical gradient force. *Applied Physics B: Lasers and Optics*, 81:159–162, June 2005.

[123] Fook-chiong Cheong, Chorng-Haur Sow, A.T.S. Wee, P. Shao, A.A. Bettiol, J.A. van Kan, and F. Watt. Optical travelator: transport and dynamic sorting of colloidal microspheres with an asymmetrical line optical tweezers. *Applied Physics B: Lasers and Optics*, 83(1):121–125, February 2006.

[124] Manas Khan, A. K. Sood, Samarendra K. Mohanty, Pradeep Kumar Gupta, Girish V Arabale, K Vijaymohanan, and C N R Rao. Optical trapping and transportation of carbon nanotubes made easy by decorating with palladium. *Optics Express*, 14(1):424–429, January 2006.

[125] Samarendra K. Mohanty, R.S. Verma, and Pradeep Kumar Gupta. Trapping and controlled rotation of low-refractive-index particles using dual line optical tweezers. *Applied Physics B: Lasers and Optics*, 87(2):211–215, March 2007.

[126] Astrid van der Horst, Andrew I. Campbell, Lambert K. van Vugt, Daniël a. Vanmaekelbergh, Marileen Dogterom, and Alfons van Blaaderen. Manipulating metal-oxide nanowires using counter-propagating optical line tweezers. *Optics Express*, 15(18):11629–11639, September 2007.

[127] Alejandro V Arzola, Karen Volke-Sepúlveda, and José L Mateos. Force mapping of an extended light pattern in an inclined plane: deterministic regime. *Optics Express*, 17(5):3429–3440, March 2009.

[128] Jared Stephens, Samarendra K. Mohanty, Suzanne Genc, Xiangduo Kong, Kyoko Yokomori, and Michael W. Berns. Spatially sculpted laser scissors for study of DNA damage and repair. *Journal of Biomedical Optics*, 14(5):054004, September 2009.

[129] Alejandro V Arzola, Karen Volke-Sepúlveda, and José L Mateos. Experimental Control of Transport and Current Reversals in a Deterministic Optical Rocking Ratchet. *Physical Review Letters*, 106(16):20–23, April 2011.

[130] Robert W Applegate, Jeff Squier, Tor Vestad, John Oakey, and David W M Marr. Optical trapping, manipulation, and sorting of cells and colloids in microfluidic systems with diode laser bars. *Optics Express*, 12(19):4390–4398, September 2004.

[131] Robert W Applegate, David W M Marr, Jeff Squier, and Steven W Graves. Particle size limits when using optical trapping and deflection of particles for sorting using diode laser bars. *Optics express*, 17(19):16731–8, September 2009.

[132] Ihab Sraj, Charles D Eggleton, Ralph Jimenez, Erich Hoover, Jeff Squier, Justin Chichester, and David W M Marr. Cell deformation cytom-

etry using diode-bar optical stretchers. *Journal of biomedical optics*, 15(4):047010, 2012.

[133] Eric R. Dufresne, Gabriel C. Spalding, Matthew T. Dearing, Steven A. Sheets, and David G. Grier. Computer-generated holographic optical tweezer arrays. *Review of Scientific Instruments*, 72(3):1810–1816, March 2001.

[134] Jennifer E Curtis, Brian A Koss, and David G. Grier. Dynamic holographic optical tweezers. *Optics Communications*, 207:169–175, June 2002.

[135] Pamela T. Korda, Michael B. Taylor, and David G. Grier. Kinetically Locked-In Colloidal Transport in an Array of Optical Tweezers. *Physical Review Letters*, 89(12):128301, September 2002.

[136] Michael P MacDonald, L Paterson, Karen Volke-Sepúlveda, J Arlt, W Sibbett, and Kishan Dholakia. Creation and manipulation of three-dimensional optically trapped structures. *Science*, 296:1101–1103, May 2002.

[137] Michael P MacDonald, Gabriel C. Spalding, and Kishan Dholakia. Microfluidic sorting in an optical lattice. *Nature*, 426:421–424, November 2003.

[138] David G. Grier. A revolution in optical manipulation. *Nature*, 424:810–816, August 2003.

[139] Matthew Pelton, Kosta Ladavac, and David G. Grier. Transport and fractionation in periodic potential-energy landscapes. *Physical Review E*, 70(3):031108, September 2004.

[140] Pamela Jordan, Jonathan Leach, Miles Padgett, Paul Blackburn, Neil Isaacs, Mattias Goksör, Dag Hanstorp, Amanda Wright, John Girkin, and Jonathan Cooper. Creating permanent 3D arrangements of isolated cells using holographic optical tweezers. *Lab on a chip*, 5(11):1224–8, November 2005.

[141] David G. Grier and Yael Roichman. Holographic optical trapping. *Applied Optics*, 45(5):880–887, February 2006.

[142] Yael Roichman, Alex Waldron, Emily Gardel, and David G. Grier. Optical traps with geometric aberrations. *Applied Optics*, 45(15):3425–3429, May 2006.

[143] Yohai Roichman and David G. Grier. Projecting extended optical traps with shape-phase holography. *Optics Letters*, 31(11):1675–1677, June 2006.

[144] Yael Roichman, Victor Wong, and David G. Grier. Colloidal transport through optical tweezer arrays. *Physical Review E*, 75(1):011407, January 2007.

[145] Marco Polin, Yohai Roichman, and David G. Grier. Autocalibrated colloidal interaction measurements with extended optical traps. *Physical*

Review E, 77(5):051401, May 2008.

[146] Maximilian Pitzek, Ruth Steiger, Gregor Thalhammer, Stefan Bernet, and Monika Ritsch-Marte. Optical mirror trap with a large field of view. *Optics Express*, 17(22):19414–19423, October 2009.

[147] S Zwick, T Haist, Y Miyamoto, L He, M Warber, A Hermerschmidt, and W Osten. Holographic twin traps. *Journal of Optics A: Pure and Applied Optics*, 11(3):034011, March 2009.

[148] Ke Xiao and David G. Grier. Multidimensional Optical Fractionation of Colloidal Particles with Holographic Verification. *Physical Review Letters*, 104(2):1–4, January 2010.

[149] Richard Bowman, Alexander Jesacher, Gregor Thalhammer, Graham Gibson, Monika Ritsch-Marte, and Miles Padgett. Position clamping in a holographic counterpropagating optical trap. *Optics Express*, 19(10):9908–9914, May 2011.

[150] Tomas Cizmar, Oto Brzobohatý, Kishan Dholakia, and Pavel Zemanek. The holographic optical micro-manipulation system based on counter-propagating beams. *Laser Physics Letters*, 8(1):50–56, January 2011.

[151] Tomas Cizmar and Kishan Dholakia. Shaping the light transmission through a multimode optical fibre: complex transformation analysis and applications in biophotonics. *Optics Express*, 19(20):18871–18884, September 2011.

[152] Arnau Farré, Marjan Shayegan, Carol López-Quesada, Gerhard a Blab, Mario Montes-Usategui, Nancy R Forde, and Estela Martín-Badosa. Positional stability of holographic optical traps. *Optics Express*, 19(22):21370–21384, October 2011.

[153] Elisabeth R Shanblatt and David G. Grier. Extended and knotted optical traps in three dimensions. *Optics Express*, 19(7):5833–5838, March 2011.

[154] Miles Padgett and Richard Bowman. Tweezers with a twist. *Nature Photonics*, 5(6):343–348, June 2011.

[155] Y Igasaki, F Li, N Yoshida, and H Toyoda. High efficiency electrically-addressable phase-only spatial light modulator. *Optical review*, 6(4):339–344, 1999.

[156] Me Friese, J Enger, H Rubinsztein-Dunlop, and Nr Heckenberg. Optical angular-momentum transfer to trapped absorbing particles. *Physical Review A*, 54(2):1593–1596, August 1996.

[157] Jesper Gluckstad. Sorting particles with light. *Nature Materials*, 3:9–10, January 2004.

[158] D. Schrader, S. Kuhr, W. Alt, M. Müller, V. Gomer, and D. Meschede. An optical conveyor belt for single neutral atoms. *Applied Physics B: Lasers and Optics*, 73(8):819–824, December 2001.

[159] Tomas Cizmar, Veneranda Garces-Chavez, Kishan Dholakia, and Pavel Zemanek. Optical conveyor belt for delivery of submicron objects. *Applied Physics Letters*, 86(17):174101, April 2005.

[160] David M. Gherardi, Antonia E. Carruthers, Tomas Cizmar, Ewan M. Wright, and Kishan Dholakia. A dual beam photonic crystal fiber trap for microscopic particles. *Applied Physics Letters*, 93(4):041110, July 2008.

[161] Tomas Cizmar, Vera Kollarova, Martin Šiler, Petr Jakl, Zdenek Bouchal, Veneranda Garces-Chavez, Kishan Dholakia, and Pavel Zemanek. Non-diffracting beam synthesis used for optical trapping and delivery of submicron objects. *Proceedings of SPIE*, 6195:619507, 2006.

[162] S. Kuhr, W. Alt, D. Schrader, M. Müller, V. Gomer, and D. Meschede. Deterministic delivery of a single atom. *Science*, 293(5528):278–280, July 2001.

[163] Tomas Cizmar, Martin Šiler, and Pavel Zemanek. An optical nanotrap array movable over a milimetre range. *Applied Physics B: Lasers and Optics*, 84:197–203, April 2006.

[164] Oto Brzobohatý, V Karásek, Martin Šiler, J Trojek, and Pavel Zemanek. Static and dynamic behavior of two optically bound microparticles in a standing wave. *Optics Express*, 19(20):19613–19626, September 2011.

[165] Alexandr Jonáš and Pavel Zemanek. Light at work: the use of optical forces for particle manipulation, sorting, and analysis. *Electrophoresis*, 29(24):4813–4851, December 2008.

[166] D McGloin, Veneranda Garces-Chavez, and Kishan Dholakia. Interfering Bessel beams for optical micromanipulation. *Optics Letters*, 28(8):657–659, May 2003.

[167] Tomas Cizmar, Veneranda Garces-Chavez, Kishan Dholakia, and Pavel Zemanek. Optical conveyor belt based on Bessel beams. *Proceedings of SPIE*, 5930:59300X, 2005.

[168] J Arlt, Veneranda Garces-Chavez, W Sibbett, and Kishan Dholakia. Optical micromanipulation using a Bessel light beam. *Optics Communications*, 197:239–245, October 2001.

[169] Martin Šiler, Tomas Cizmar, Alexandr Jonáš, and Pavel Zemanek. Delivery of multiparticle chains by an optical conveyor belt. *Proceedings of SPIE*, 7138:713822–713822–6, 2008.

[170] Tomas Cizmar, Martin Šiler, Mojmír Šerý, Pavel Zemanek, Veneranda Garces-Chavez, and Kishan Dholakia. Optical sorting and detection of submicrometer objects in a motional standing wave. *Physical Review B*, 74(3):035105, July 2006.

[171] Martin Šiler, Tomas Cizmar, Mojmír Šerý, and Pavel Zemanek. Optical forces generated by evanescent standing waves and their usage for sub-

micron particle delivery. *Applied Physics B: Lasers and Optics*, 84:157–165, May 2006.

[172] Martin Šiler, Tomas Cizmar, Alexandr Jonáš, and Pavel Zemanek. Surface delivery of a single nanoparticle under moving evanescent standing-wave illumination. *New Journal of Physics*, 10(11):113010, November 2008.

[173] Tomas Cizmar and Pavel Zemanek. Optical tracking of spherical micro-objects in spatially periodic interference fields. *Optics Express*, 15(5):2262–2272, March 2007.

[174] Woei Ming Lee, Peter J Reece, Robert F Marchington, Nikolaus K Metzger, and Kishan Dholakia. Construction and calibration of an optical trap on a fluorescence optical microscope. *Nature Protocols*, 2(12):3226–3238, January 2007.

[175] Vassili Demergis and Ernst-Ludwig Florin. High precision and continuous optical transport using a standing wave optical line trap. *Optics Express*, 19(21):20833–20848, October 2011.

[176] David S. Sholl and Kristen A. Fichthorn. Effect of correlated flights on particle mobilities during single-file diffusion. *Physical Review E*, 55(6):7753–7756, June 1997.

[177] QH Wei, Clemens Bechinger, and P. Leiderer. Single-File Diffusion of Colloids in One-Dimensional Channels. *Science*, 287(5453):625–627,

July 2000.

[178] S C Lim and L P Teo. Modeling single-file diffusion with step fractional Brownian motion and a generalized fractional Langevin equation. *Journal of Statistical Mechanics: Theory and Experiment*, 2009(08):P08015, August 2009.

[179] J. Delfau, C. Coste, C. Even, and Michel Saint Jean. Single-file diffusion of interacting particles in a finite-sized channel. *Physical Review E*, 82(3):031201, September 2010.

[180] K Hahn, J Kärger, and V Kukla. Single-file diffusion observation. *Physical Review Letters*, 76(15):2762–2765, April 1996.

[181] Binhua Lin, Mati Meron, Bianxiao Cui, Stuart A Rice, and Haim Diamant. From random walk to single-file diffusion. *Physical review letters*, 1(2):1–4, 2005.

[182] Markus Kollmann. Single-file diffusion of atomic and colloidal systems: Asymptotic laws. *Physical Review Letters*, 90(18):180602, 2003.

[183] K Hahn and J. Karger. Deviations from the normal time regime of single-file diffusion. *Journal of Physical Chemistry B*, 102(30):5766–5771, 1998.

[184] Christoph Lutz, Markus Kollmann, and Clemens Bechinger. Single-File Diffusion of Colloids in One-Dimensional Channels. *Physical Review Letters*, 93(2):026001, July 2004.

[185] L. Lizana and T. Ambjörnsson. Single-File Diffusion in a Box. *Physical Review Letters*, 100(20):200601, May 2008.

[186] B Hille and W Schwarz. Potassium channels as multi-ion single-file pores. *The Journal of General Physiology*, 72(4):409–442, October 1978.

[187] Tom Chou and Detlef Lohse. Entropy-Driven Pumping in Zeolites and Biological Channels. *Physical Review Letters*, 82(17):3552–3555, April 1999.

[188] J A Hernández and J Fischbarg. Kinetic analysis of water transport through a single-file pore. *The Journal of general physiology*, 99(4):645–62, April 1992.

[189] S Draber, R Schultze, and UP Hansen. Patch-clamp studies on the anomalous mole fraction effect of the K+ channel in cytoplasmic droplets ofNitella: An attempt to distinguish between a multi-ion single-file. *Journal of Membrane Biology*, 190:183–190, 1991.

[190] P a Rosenberg and a Finkelstein. Water permeability of gramicidin A-treated lipid bilayer membranes. *The Journal of general physiology*, 72(3):341–50, September 1978.

[191] AL Hodgkin and RD Keynes. The potassium permeability of a giant nerve fibre. *The Journal of physiology*, (1949):61–88, 1955.

[192] Poul Martin Hansen, Vikram Kjø ller Bhatia, Niels Harrit, and Lene B Oddershede. Expanding the optical trapping range of gold nanoparticles. *Nano Letters*, 5(10):1937–1942, October 2005.

[193] Faeghe Hajizadeh and S Nader S Reihani. Optimized optical trapping of gold nanoparticles. *Optics Express*, 18(2):551–559, January 2010.

[194] Sun-Uk Hwang and Yong-Gu Lee. Simulation of an oil immersion objective lens: a simplified ray-optics model considering Abbes sine condition. *Optics Express*, 16(26):21170–21183, December 2008.

[195] J Happel and H Brenner. *Low Reynolds Number Hydrodynamics*. Prentice-Hall Inc., 1965.

[196] Kishan Dholakia and Pavel Zemanek. Colloquium: Gripped by light: Optical binding. *Reviews of Modern Physics*, 82(2):1767–1791, June 2010.

[197] Tomas Cizmar, L C Dávila Romero, Kishan Dholakia, and David L. Andrews. Multiple optical trapping and binding: new routes to self-assembly. *Journal of Physics B: Atomic, Molecular and Optical Physics*, 43(10):102001, May 2010.

[198] Oto Brzobohatý, Tomas Cizmar, V Karásek, Martin Šiler, Kishan Dholakia, and Pavel Zemanek. Experimental and theoretical determination of optical binding forces. *Optics Express*, 18(24):25389–25402, November 2010.

[199] Jack Ng, Zhifang Lin, C T Chan, and Ping Sheng. Photonic clusters formed by dielectric microspheres: numerical simulations. *Physical Review B*, 72(8):085130, August 2005.

[200] Michael D. Summers, Richard D. Dear, Jonathan M. Taylor, and Grant A. D. Ritchie. Directed assembly of optically bound matter. *Optics Express*, 20(2):1001–1012, January 2012.

[201] Christopher D Mellor, Thomas A Fennerty, and Colin D Bain. Polarization effects in optically bound particle arrays. *Optics Express*, 14(21):10079–10088, October 2006.

[202] Pierre Van Rysselberghe. Remarks concerning the Clausius-Mossotti Law. *The Journal of Physical Chemistry*, 49(1850):1152–1155, 1932.

[203] E D Palik. *Handbook of optical constants of solids*. Academic Press, Boston, 1998.

[204] Frederick Gittes, B Mickey, J Nettleton, and J Howard. Flexural rigidity of microtubules and actin filaments measured from thermal fluctuations in shape. *The Journal of Cell Biology*, 120(4):923–934, February 1993.

[205] Rafael R Daga, Kyeng-Gea Lee, Scott Bratman, Silvia Salas-Pino, and Fred Chang. Self-organization of microtubule bundles in anucleate fission yeast cells. *Nature Cell Biology*, 8(10):1108–1113, October 2006.

[206] Cecilia Conde and Alfredo Cáceres. Microtubule assembly, organization and dynamics in axons and dendrites. *Nature Reviews. Neuroscience*, 10(5):319–332, May 2009.

[207] Katja Marie Taute, Francesco Pampaloni, Erwin Frey, and Ernst-ludwig Florin. Microtubule dynamics depart from the wormlike chain model. *Physical review letters*, 028102(January):1–4, January 2008.

[208] Carlos Bustamante, Yann R Chemla, Nancy R Forde, and David Izhaky. Mechanical processes in biochemistry. *Annual Review of Biochemistry*, 73:705–748, 2004.

[209] Jijun Dong, Carlos E Castro, Mary C Boyce, Matthew J Lang, and Susan Lindquist. Optical trapping with high forces reveals unexpected behaviors of prion fibrils. *Nature structural & molecular biology*, 17(12):1422–30, December 2010.

[210] Preethi L. Chandran and Mohammad R. K. Mofrad. Averaged implicit hydrodynamic model of semiflexible filaments. *Physical Review E*, 81(3):031920, March 2010.

[211] Pierre-Gilles De Gennes. *Scaling Concepts in Polymer Physics*. Cornell University Press, 1979.

[212] Maximilian Ebner. *Biological nanofibers in a Standing Wave Optical Trap*. PhD thesis, University of Texas at Austin, 2007.

[213] F. Borghese, P. Denti, R. Saija, M. Iatì, and O. Maragò. Radiation Torque and Force on Optically Trapped Linear Nanostructures. *Physical Review Letters*, 100(16):1–4, April 2008.

[214] Vincenzo Lombardi, Gabriella Piazzesi, and Marco Linari. Rapid regeneration of the actin-myosin power stroke in contracting muscle. *Nature*, 355(13 Feb):638–641, February 1992.

[215] SJ Kron and JA Spudich. Fluorescent actin filaments move on myosin fixed to a glass surface. *Proceedings of the National Academy of Sciences*, 83(17):6272–6276, September 1986.

[216] Ivan Rayment, Hazel M Holden, Michael Whittaker, Christopher B. Yohn, Michael Lorenz, Kenneth C Holmes, and Ronald A. Milligan. Structure of the actin-myosin complex and its implications for muscle contraction. *Science*, 261:58–65, July 1993.

[217] Wolfgang Kabsch, Hans Georg Mannherz, Dietrich Suck, Emil F. Pai, and Kenneth C Holmes. Atomic structure of the actin: DNase I complex. *Nature*, 347(6 Sept):37–44, September 1990.

[218] Kenneth C Holmes, David Popp, Werner Gebhard, and Wolfgang Kabsch. Atomic model of the actin filament. *Nature*, 347:44–49, September 1990.

[219] Manfred Schliwa and Günther Woehlke. Molecular motors. *Nature*, 422(6933):759–765, April 2003.

[220] Steven J. Lade, Erin M. Craig, and Heiner Linke. Effectiveness of beads for tracking small-scale molecular motor dynamics. *Physical Review E*, 84(2):021907, August 2011.

[221] Hiroaki Kojima, E Muto, H Higuchi, and T Yanagida. Mechanics of single kinesin molecules measured by optical trapping nanometry. *Biophysical Journal*, 73(4):2012–2022, October 1997.

[222] C C Gregorio, H Granzier, H Sorimachi, and S Labeit. Muscle assembly: a titanic achievement? *Current Opinion in Cell Biology*, 11(1):18–25, February 1999.

[223] Agnieszka K. Rzadzinska, Mark E. Schneider, Caroline Davies, Gavin P. Riordan, and Bechara Kachar. An actin molecular treadmill and myosins maintain stereocilia functional architecture and self-renewal. *The Journal of cell biology*, 164(6):887–897, 2004.

[224] Abigail Klopper. Biophysics: Two-tone deaf. *Nature Physics*, 8(6):446–446, May 2012.

[225] Jérémie Barral and Pascal Martin. Phantom tones and suppressive masking by active nonlinear oscillation of the hair-cell bundle. *Proceedings of the National Academy of ...*, 109(21), 2012.

[226] E. Barkai and R. Silbey. Theory of Single File Diffusion in a Force Field. *Physical Review Letters*, 102(5):050602, February 2009.

[227] Thomas Franosch and Sylvia Jeney. Persistent correlation of constrained colloidal motion. *Physical Review E*, 79(3):031402, March 2009.

[228] Binhua Lin, Bianxiao Cui, Ji-Hwan Lee, and Jonathan Yu. Hydrodynamic coupling in diffusion of quasione-dimensional Brownian particles. *Europhysics Letters*, 57(5):724–730, March 2002.

[229] Gwennou Coupier, Michel Saint Jean, and Claudine Guthmann. Single file diffusion in macroscopic Wigner rings. *Physical Review E*, 73(3):031112, March 2006.

[230] Keir C Neuman and Attila Nagy. Single-molecule force spectroscopy: optical tweezers, magnetic tweezers and atomic force microscopy. *Nature Methods*, 5(6):491–505, June 2008.

[231] B. DeMarco and D. S. Jin. Onset of Fermi Degeneracy in a Trapped Atomic Gas. *Science*, 285(5434):1703–1706, September 1999.

[232] A G Truscott, K E Strecker, W I McAlexander, G B Partridge, and R G Hulet. Observation of Fermi pressure in a gas of trapped atoms. *Science*, 291(5513):2570–2, March 2001.

[233] M H Anderson, J R Ensher, M R Matthews, C E Wieman, and E A Cornell. Observation of bose-einstein condensation in a dilute atomic vapor. *Science*, 269(5221):198–201, July 1995.

[234] T. Gustavson, AP Chikkatur, A. Leanhardt, A. Görlitz, Satyandra K Gupta, D. E. Pritchard, and Wolfgang Ketterle. Transport of Bose-

Einstein Condensates with Optical Tweezers. *Physical Review Letters*, 88(2):020401, December 2001.

[235] S Inouye, T Pfau, S Gupta, AP Chikkatur, A Gorlitz, D. E. Pritchard, and Wolfgang Ketterle. Phase-coherent amplification of atomic matter waves. *Nature*, 224(1985):641–644, 1999.

[236] Keir C Neuman, E H Chadd, G F Liou, K Bergman, and Steven M. Block. Characterization of photodamage to Escherichia coli in optical traps. *Biophysical Journal*, 77(5):2856–2863, November 1999.

[237] Anita Jannasch, Ahmet F. Demirors, Peter D. J. van Oostrum, Alfons van Blaaderen, and Erik Schaffer. Nanonewton optical force trap employing anti-reflection coated, high-refractive-index titania microspheres. *Nature Photonics*, (June):2–6, 2012.

[238] A Hopt and E Neher. Highly nonlinear photodamage in two-photon fluorescence microscopy. *Biophysical journal*, 80(4):2029–36, April 2001.

[239] Yan Fu, Haifeng Wang, Riyi Shi, and Ji-Xin Cheng. Characterization of photodamage in coherent anti-Stokes Raman scattering microscopy. *Optics express*, 14(9):3942–51, May 2006.

[240] Francoise Dapasse and Jean-Marie Vigoureux. Optical binding force between two Rayleigh particles. *Journal of Physics D: Applied Physics*, 27:914–919, 1994.

[241] Patrick C. Chaumet and Manuel Nieto-Vesperinas. Optical binding of particles with or without the presence of a flat dielectric surface. *Physical Review B*, 64(3):35422, June 2001.

[242] S. a. Tatarkova, Antonia E. Carruthers, and Kishan Dholakia. One-Dimensional Optically Bound Arrays of Microscopic Particles. *Physical Review Letters*, 89(28):283901, December 2002.

[243] Manuel Nieto-Vesperinas. Near-field photonic forces. *Philisophical Transactions of the Royal Society A*, 362:719–737, February 2004.

[244] David S. Bradshaw and David L. Andrews. Optically induced forces and torques: Interactions between nanoparticles in a laser beam. *Physical Review A*, 72(3):1–14, September 2005.

[245] Tomasz M Grzegorczyk, Brandon A Kemp, and Jin Au Kong. Stable Optical Trapping Based on Optical Binding Forces. *Physical Review Letters*, 96(11):113903, March 2006.

[246] Marc Guillon, Olivier Moine, and Brian Stout. Longitudinal Optical Binding of High Optical Contrast Microdroplets in Air. *Physical Review Letters*, 96(14):143902, April 2006.

[247] Tomasz M Grzegorczyk, Brandon a Kemp, and Jin Au Kong. Trapping and binding of an arbitrary number of cylindrical particles in an in-plane electromagnetic field. *Journal of the Optical Society of America A*, 23(9):2324–2330, September 2006.

[248] Tomasz M Grzegorczyk, Brandon A Kemp, and Jin Au Kong. Passive guiding and sorting of small particles with optical binding forces. *Optics Letters*, 31(22):3378–3380, November 2006.

[249] V Karásek, Kishan Dholakia, and Pavel Zemanek. Analysis of optical binding in one dimension. *Applied Physics B: Lasers and Optics*, 84:149–156, 2006.

[250] NK Nikolaus K Metzger, Kishan Dholakia, and Ewan M. Wright. Observation of bistability and hysteresis in optical binding of two dielectric spheres. *Physical review letters*, 068102(February):1–4, February 2006.

[251] Nikolaus K Metzger, Ewan M. Wright, W Sibbett, and Kishan Dholakia. Visualization of optical binding of microparticles using a femtosecond fiber optical trap. *Optics Express*, 14(8):3677–3687, April 2006.

[252] V Karásek and Pavel Zemanek. Analytical description of longitudinal optical binding of two spherical nanoparticles. *Journal of Optics A: Pure and Applied Optics*, 9(8):S215–S220, July 2007.

[253] Justo Rodríguez, Luciana C. Davila Romero, and David L. Andrews. Optically induced potential energy landscapes. *Journal of Nanophotonics*, 1:019503, October 2007.

[254] A. Salam. Two alternative derivations of the static contribution to the radiation-induced intermolecular energy shift. *Physical Review A*, 76(6):1–5, December 2007.

[255] Anna S Zelenina, Romain Quidant, and Manuel Nieto-Vesperinas. Enhanced optical forces between coupled resonant metal nanoparticles. *Optics Letters*, 32(9):1156–1158, May 2007.

[256] V Karásek, Tomas Cizmar, Oto Brzobohatý, Pavel Zemanek, Veneranda Garces-Chavez, and Kishan Dholakia. Long-range one-dimensional longitudinal optical binding. *Physical review letters*, 101(October):143601, October 2008.

[257] Justo Rodríguez and David L. Andrews. Optical binding and the influence of beam structure. *Optics Letters*, 33(21):2464–2466, November 2008.

[258] Justo Rodríguez, Luciana Dávila Romero, and David L. Andrews. Optical binding in nanoparticle assembly: Potential energy landscapes. *Physical Review A*, 78(4):043805, October 2008.

[259] D. Haefner, S. Sukhov, and A. Dogariu. Conservative and Nonconservative Torques in Optical Binding. *Physical Review Letters*, 103(17):173602, October 2009.

[260] V Karásek, Oto Brzobohatý, and Pavel Zemanek. Longitudinal optical binding of several spherical particles studied by the coupled dipole method. *Journal of Optics A: Pure and Applied Optics*, 11(3):034009, March 2009.

[261] Justo Rodríguez and David L. Andrews. Influence of the state of light on the optically induced interparticle interaction. *Physical Review A*, 79(2):022106, February 2009.

[262] Jonathan M. Taylor and Gordon D. Love. Optical binding mechanisms : a conceptual model for Gaussian beam traps. *Optics Express*, 17(17):15381–15389, August 2009.

[263] David L. Andrews and Luciana C. Davila Romero. The electrodynamic mechanisms of optical binding. *Proceedings of SPIE*, 7613:761309, 2010.

[264] Oto Brzobohatý, Vitzslav Karasek, Pavel Zemanek, Tomaš Imar, and Kishan Dholakia. Formation of one-dimensional optically bound structures of polystyrene particles near the surface. *Proceedings of SPIE*, 7762:776212, 2010.

[265] Luciana C. Davila Romero, Scott N. A. Smith, and David L. Andrews. Optical binding between polar particles. *Proceedings of SPIE*, 7712:771219, 2010.

[266] Luciana C. Davila Romero and David L. Andrews. Geometric configurations and perturbative mechanisms in optical binding. *Proceedings of SPIE*, 7613:76130P, 2010.

[267] Kesava Jay, Patrick C. Chaumet, T. N. Langtry, and Adel Rahmani. Optical binding of electrically small magnetodielectric particles. *Journal of Nanophotonics*, 4(1):041583, 2010.

[268] Michael D. Summers, Richard D. Dear, Jonathan M. Taylor, and Grant A. D. Ritchie. Controlled formation of optically bound matter in evanescent fields. *Proceedings of SPIE*, 7762:776213, 2010.

[269] Jonathan M. Taylor and Gordon D. Love. On- and off-axis binding and induced circulation in counter-propagating beam traps. *Proceedings of SPIE*, 7613:76130O, 2010.

[270] Jun Chen, Jack Ng, Pei Wang, and Zhifang Lin. Analytical partial wave expansion of vector Bessel beam and its application to optical binding. *Optics Letters*, 35(10):1674–1676, April 2011.

[271] Wolfgang Singer, Manfred Frick, Stefan Bernet, and Monika Ritsch-Marte. Self-organized array of regularly spaced microbeads in a fiber-optical trap. *Journal of the Optical Society of America B*, 20(7):1568–1574, July 2003.

[272] Nikolaus K Metzger, Robert F Marchington, M. Mazilu, R. L. Smith, Kishan Dholakia, and Ewan M. Wright. Measurement of the Restoring Forces Acting on Two Optically Bound Particles from Normal Mode Correlations. *Physical Review Letters*, 98(6):068102, February 2007.

[273] George M Whitesides and Bartosz Grzybowski. Self-assembly at all scales. *Science*, 295(5564):2418–21, March 2002.

[274] Jack Ng and C T Chan. Localized vibrational modes in optically bound structures. *Optics Letters*, 31(17):2583–2585, September 2006.

[275] Christopher D Mellor and Colin D Bain. Array formation in evanescent waves. *ChemPhysChem*, 7(2):329–332, March 2006.

[276] Veneranda Garces-Chavez, Romain Quidant, Peter J Reece, G. Badenes, L. Torner, and Kishan Dholakia. Extended organization of colloidal microparticles by surface plasmon polariton excitation. *Physical Review B*, 73(8):085417, February 2006.

[277] Peter J Reece, Ewan M. Wright, and Kishan Dholakia. Experimental Observation of Modulation Instability and Optical Spatial Soliton Arrays in Soft Condensed Matter. *Physical Review Letters*, 98(20):203902, May 2007.

[278] Vassili Demergis and Ernst-Ludwig Florin. Ultrastrong Optical Binding of Metallic Nanoparticles. *Nano letters*, October 2012.

[279] Patrick C. Chaumet and Manuel Nieto-Vesperinas. Coupled dipole method determination of the electromagnetic force on a particle over a flat dielectric substrate. *Physical Review B*, 61(20):119–127, May 2000.

[280] Patrick C. Chaumet and Manuel Nieto-Vesperinas. Electromagnetic force on a metallic particle in the presence of a dielectric surface. *Physical Review B*, 62(16):11185–11191, October 2000.

[281] Kirk T. McDonald. Scattering of a Plane Wave by a Small Conducting Sphere. *cosmology.princeton.edu*, pages 1–10, July 2004.

[282] P M Celliers and J Conia. Measurement of localized heating in the focus of an optical trap. *Applied Optics*, 39(19):3396–3407, July 2000.

[283] Erwin J G Peterman, Frederick Gittes, and Christoph F Schmidt. Laser-induced heating in optical traps. *Biophysical Journal*, 84(2):1308–1316, February 2003.

[284] Y Liu, D K Cheng, G J Sonek, Michael W. Berns, C F Chapman, and B J Tromberg. Evidence for localized cell heating induced by infrared optical tweezers. *Biophysical Journal*, 68(5):2137–2144, May 1995.

[285] Andreas Schönle and Stefan W Hell. Heating by absorption in the focus of an objective lens. *Optics Letters*, 23(5):325–327, March 1998.

[286] S Nader S Reihani and Lene B Oddershede. Optimizing immersion media refractive index improves optical trapping by compensating spherical aberrations. *Optics Letters*, 32(14):1998–2000, July 2007.

[287] Markus Selmke, Marco Braun, and Frank Cichos. Nano-lens diffraction around a single heated nano particle. *Optics Express*, 20(7):8055–8070, March 2012.

[288] Anders Kyrsting, Poul M Bendix, Dimitrios G Stamou, and Lene B Oddershede. Heat profiling of three-dimensionally optically trapped gold nanoparticles using vesicle cargo release. *Nano Letters*, 11(2):888–92, February 2011.

[289] Yeonee Seol, Amanda E Carpenter, and Thomas T Perkins. Gold nanoparticles: enhanced optical trapping and sensitivity coupled with significant heating. *Optics Letters*, 31(16):2429–2431, August 2006.

[290] P. V. Ruijgrok, N. R. Verhart, P. Zijlstra, A. L. Tchebotareva, and Michel Orrit. Brownian Fluctuations and Heating of an Optically Aligned Gold Nanorod. *Physical Review Letters*, 107(3):037401, July 2011.

[291] Erwin Frey and Klaus Kroy. Brownian motion: a paradigm of soft matter and biological physics. *Annalen der Physik*, 14(1-3):20–50, February 2005.

[292] Rongxin Huang, Isaac Chavez, Katja Marie Taute, Branimir Lukić, Sylvia Jeney, Mark G. Raizen, and Ernst-Ludwig Florin. Direct observation of the full transition from ballistic to diffusive Brownian motion in a liquid. *Nature Physics*, 7(7):576–580, March 2011.

[293] Wesley P Wong and Ken Halvorsen. The effect of integration time on fluctuation measurements : calibrating an optical trap in the presence of motion blur. *Optics Express*, 14(25):12517–12531, December 2006.

[294] J. R. Arias-Gonzalez and Manuel Nieto-Vesperinas. Optical forces on small particles: attractive and repulsive nature and plasmon-resonance conditions. *Journal of the Optical Society of America A*, 20(7):1201–1209, July 2003.

[295] Matthew Pelton, Mingzhao Liu, Hee Y. Kim, Glenna Smith, S Cass Ave, Philippe Guyot-Sionnest, and Norbert F. Scherer. Optical trapping and alignment of single gold nanorods using plasmon resonances. *Proceedings of SPIE*, 6323:63230E, 2006.

[296] B Sepúlveda, J Alegret, and M Käll. Nanometric control of the distance between plasmonic nanoparticles using optical forces. *Optics Express*, 15(22):14914–14920, October 2007.

[297] Mathieu L Juan, Maurizio Righini, and Romain Quidant. Plasmon nano-optical tweezers. *Nature Photonics*, 5(6):349–356, June 2011.

[298] Maria Dienerowitz, Michael Mazilu, Peter J Reece, Thomas F Krauss, and Kishan Dholakia. Optical vortex trap for resonant confinement of metal nanoparticles. *Optics express*, 16(7):4991–9, March 2008.

[299] Boris Khlebtsov, Andrei Melnikov, Vladimir Zharov, and Nikolai Khlebtsov. Absorption and scattering of light by a dimer of metal nanospheres: comparison of dipole and multipole approaches. *Nanotechnology*, 17:1437–1445, February 2006.

[300] PB Johnson and RW Christy. Optical constants of the noble metals. *Physical Review B*, 6(45):4370–4379, December 1972.

[301] L G Schulz. The optical constants of silver, gold, copper, and aluminum. I. The absorption coefficient k. *Journal of the Optical Society of America*, 44(5):357–362, May 1954.

[302] L G Schulz and F. R. Tangherlini. Optical constants of silver, gold, copper, and aluminum. II. The index of refraction n. *Journal of the Optical Society of America*, 44(5):362–368, May 1954.

[303] Patrick Stoller, Volker Jacobsen, and Vahid Sandoghdar. Measurement of the complex dielectric constant of a single gold nanoparticle. *Optics Letters*, 31(16):2474–2476, August 2006.

[304] Lucia B. Scaffardi and Jorge O. Tocho. Size dependence of refractive index of gold nanoparticles. *Nanotechnology*, 17:1309–1315, February 2006.

[305] Y Nishijima, L Rosa, and S Juodkazis. Surface plasmon resonances in periodic and random patterns of gold nano-disks for broadband light harvesting. *Optics Express*, 12(5):2187–92, May 2012.

[306] Yoshiaki Nishijima, Kosei Ueno, Yukie Yokota, Kei Murakoshi, and Hiroaki Misawa. Plasmon-Assisted Photocurrent Generation from Visible to Near-Infrared Wavelength Using a Au-Nanorods/TiO 2 Electrode. *The Journal of Physical Chemistry Letters*, 1(13):2031–2036, July 2010.

[307] Xi Chen, Baohua Jia, Jhantu K Saha, Boyuan Cai, Nicholas Stokes, Qi Qiao, Yongqian Wang, Zhengrong Shi, and Min Gu. Broadband enhancement in thin-film amorphous silicon solar cells enabled by nucleated silver nanoparticles. *Nano letters*, 12(5):2187–92, May 2012.

[308] Hairen Tan, Rudi Santbergen, Arno H M Smets, and Miro Zeman. Plasmonic Light Trapping in Thin-film Silicon Solar Cells with Improved Self-Assembled Silver Nanoparticles. *Nano letters*, 12(8):4070–6, August 2012.

[309] Alexandre Aubry, Dang Yuan Lei, Antonio I Fernández-Domínguez, Yannick Sonnefraud, Stefan A Maier, and J B Pendry. Plasmonic light-harvesting devices over the whole visible spectrum. *Nano letters*, 10(7):2574–9, July 2010.

[310] Dmitri K. Gramotnev and Sergey I. Bozhevolnyi. Plasmonics beyond the diffraction limit. *Nature Photonics*, 4(2):83–91, January 2010.